

# Physically Based Modeling of Micro-Appearance

Dissertation

zur

Erlangung des Doktorgrades (Dr. rer. nat.)

der

Mathematisch-Naturwissenschaftlichen Fakultät

der

Rheinischen Friedrich-Wilhelms-Universität Bonn

vorgelegt von

**M.Sc. Weizhen Huang**

aus

Hubei, China

Bonn, November 2022



Angefertigt mit Genehmigung der Mathematisch-Naturwissenschaftlichen  
Fakultät der Rheinischen Friedrich-Wilhelms-Universität Bonn

Gutachter: Prof. Dr. Matthias B. Hullin  
Gutachter: Prof. Dr. Reinhard Klein

Tag der Promotion: 26. April 2023  
Erscheinungsjahr: 2023



## Abstract

Today, the computer graphics community still struggles to create photorealistic images. Looking at the objects around us, we might be unaware of all the microscale details and irregularities that contribute to the final appearance. However, the lack of such details is an important reason why we can tell a rendered image from a photograph.

In this dissertation, we focus on generating and rendering such microscale content in a physically based way. We also validate rendered results against measurements.

In Chapter 3 we model the *fluid flow on soap bubbles*. Soap film thickness is usually in the range of micrometers, demonstrating beautiful iridescence. Previously, the variation in film thickness has been approximated by random noise textures; such simplification fails to capture the rich appearance of soap bubbles. Our work instead considers the mechanics that drive such fluid flow, namely, the Navier-Stokes equations, surfactant concentration, Marangoni surface tension, air friction, gravity, evaporation, *etc.* However, simulating such a physical process brings a series of challenges: the significantly smaller radial extent compared with the lateral extent, the singularity at poles when advecting in spherical coordinates, the small step size needed when solving an extremely stiff system, and the blurring of details after repeated advection, for example. We design proper algorithms to address the above issues, thus simulating a wide range of dynamic effects on soap bubbles that match real-world footage for the first time.

In Chapter 4, we build a physically based *hair scattering model*. Hair has a diameter of around  $80\ \mu\text{m}$ ; its appearance is due to even smaller structures, such as the cuticle scales and the pigments inside. Hair rendering is a long-studied topic. Virtually all current models are based on the Marschner model, where one splits the scattering function into a longitudinal and an azimuthal component. This separation has its benefit in importance sampling but lacks a physical ground, therefore does not match the measurement. We revisit this topic and propose a novel physically based hair scattering model, representing hair as cylinders with microfacet roughness. We demonstrate that a 3D analysis of the light interaction with hairs is simpler than it seems, so the former reduction to 2D analysis in the cross-section plane is unnecessary. In this way, we reveal that the focused highlight in the forward-scattering direction, observed in the measurement but not properly explained and modeled before, is a result of the rough cylindrical geometry itself. Our

model also makes the extension to hair with elliptical cross-sections much more straightforward and natural.

A much-related topic, *feather rendering*, is discussed in Chapter 5. Few previous scientific works are available on this topic, while in production, feathers are usually approximated by hair scattering models due to their similar fiber-like appearance. However, feathers have distinct substructures with non-cylindrical cross-sections, differing from human hairs. In particular, a feather consists of many side branches, called barbs; similarly, a barb consists of numerous side branches called barbules; the barbules have irregular cross-sections. We build a scattering model directly upon such multi-scale geometries: the feather is modeled as a collection of barb primitives, the geometry of which is an extrusion of a circular arc, corresponding to the curved axis of barbules; the contribution of the barbule cross-sections is packed in a normal distribution function, similar to in microfacet theory, while the local shading frame of the barb geometry is aligned with the barbule axis. We present the model on rock dove neck feathers and show that the result closely matches the BSDF measurements and photographs.



## Acknowledgments

I would like to express my deepest appreciation to my advisor Prof. Dr. Matthias B. Hullin, who introduced me to such an interesting interdisciplinary research group and never failed to provide me with inspiration, support, and trust throughout my Ph.D. studies.

I could not have undertaken the journey of computer graphics without Prof. Dr. Leif Kobbelt and Dr. Philip Trettner from RWTH Aachen University. They have opened up a whole new world to me with their fascinating and ardent ways of giving lectures.

I also thank my doctoral committee members: Prof. Dr. Matthias B. Hullin, Prof. Dr. Reinhard Klein, Prof. Dr. Maren Bennewitz, and Prof. Dr. Martin Rumpf. Thank you for making an effort to assess my thesis.

Special thanks to some of my co-authors from other universities: Assoc. Prof. Dr. Chenfanfu Jiang, Prof. Dr. Doekele G. Stavenga, and Dr. Johannes Hanika, whose passion for their fields deeply touched me and made the collaboration possible. Thank you for the valuable suggestions and discussions.

I am also thankful for my other collaborators: Dr. Julian Iseringhausen, Tom Kneiphof, Ziyin Qu, Sebastian Merzbach, and Clara Callenberg. Thank you for offering help and feedback.

Lastly, I would like to thank my mother and my friends, who always believe I can achieve whatever I want.

This work was supported by the European Research Council under ERC Starting Grant “ECHO” (802192).



# Contents

<b>List of Figures</b>	<b>i</b>
<b>List of Tables</b>	<b>iii</b>
<b>List of Abbreviations</b>	<b>v</b>
<b>1 Introduction</b>	<b>1</b>
1.1 Motivation . . . . .	1
1.2 Soap Film Dynamics . . . . .	4
1.3 Hair Structure and Rendering . . . . .	5
1.4 Feather Structure and Rendering . . . . .	8
<b>2 Background</b>	<b>11</b>
2.1 BxDFs . . . . .	11
2.1.1 Microfacet BSDF . . . . .	11
2.1.2 BCSDf . . . . .	12
2.2 Hair Primitive . . . . .	14
2.3 Thin-film Interference . . . . .	15
<b>3 Chemomechanical Simulation of Soap Film Flow on Spherical Bubbles</b>	<b>17</b>
3.1 Motivation . . . . .	19
3.2 Related Work . . . . .	21
3.3 Physical Model . . . . .	22
3.3.1 Governing equations in 3D . . . . .	23
3.3.2 Thin-film analysis and governing equation on spheres . . . . .	25
3.3.3 Surface and body forces . . . . .	27
3.4 Method . . . . .	28
3.4.1 Spatial discretization . . . . .	28
3.4.2 Advection . . . . .	30
3.4.3 Concentration splitting . . . . .	34

3.4.4	Implementation and runtime performance . . . . .	35
3.5	Soap bubble rendering . . . . .	36
3.5.1	Thin film model . . . . .	36
3.5.2	Soap bubble ray tracing . . . . .	38
3.6	Results . . . . .	40
3.6.1	Mean surfactant concentration and bubble radius . . .	42
3.6.2	Gravity and buoyancy . . . . .	44
3.6.3	Air friction . . . . .	45
3.6.4	Evaporation . . . . .	45
3.6.5	Real-world experiments . . . . .	46
3.7	Discussion and Future Work . . . . .	46
3.7.1	Viscous film . . . . .	47
3.7.2	Black film . . . . .	47
<b>4</b>	<b>A Microfacet-based Hair Scattering Model</b>	<b>49</b>
4.1	Introduction . . . . .	51
4.2	Background and Related Work . . . . .	53
4.3	Model . . . . .	55
4.3.1	A Microfacet BCSDf . . . . .	55
4.3.2	Scale Tilt . . . . .	60
4.3.3	Extending the Model to Elliptical Hair Fibers . . . . .	61
4.3.4	Implementation . . . . .	63
4.4	Results and Comparison . . . . .	66
4.4.1	Validation . . . . .	66
4.4.2	Rendering Hair Scenes . . . . .	74
4.5	Discussion and Limitation . . . . .	77
4.6	Conclusion and Future Work . . . . .	79
<b>5</b>	<b>Rendering Iridescent Rock Dove Neck Feathers</b>	<b>81</b>
5.1	Introduction . . . . .	84
5.2	Related Work . . . . .	85
5.3	Background . . . . .	86
5.3.1	Feather Geometry . . . . .	86
5.3.2	The Colors of Bird Feathers . . . . .	87
5.3.3	The Physics of Thin Films . . . . .	88
5.3.4	Measuring with an Imaging Scatterometer . . . . .	90
5.4	Modeling . . . . .	90
5.4.1	Elliptical BSDF . . . . .	91
5.4.2	Implementation . . . . .	96
5.5	Results and Comparison . . . . .	99
5.5.1	Comparison with Scatterograms . . . . .	99

5.5.2	Comparison with Photographs . . . . .	100
5.5.3	Performance . . . . .	100
5.6	Conclusion and Future Work . . . . .	101
<b>6</b>	<b>Conclusion and Future Work</b>	<b>103</b>
	<b>Bibliography</b>	<b>120</b>
	<b>Appendices</b>	<b>122</b>
<b>A</b>	<b>Material Derivative in Spherical Coordinates</b>	<b>122</b>
<b>B</b>	<b>2<sup>nd</sup>-Order Half-Step Update</b>	<b>124</b>
<b>C</b>	<b>Linear System</b>	<b>125</b>
<b>D</b>	<b>Derivation of the kinematic condition and the lubrication model in Eq. (3.10)</b>	<b>126</b>
D.1	The Kinematic Condition . . . . .	126
D.2	Asymptotic Expansion . . . . .	127
<b>E</b>	<b>Analytical Integration of the lobe for GGX</b>	<b>134</b>
<b>F</b>	<b>Interference on Flat and Curved Thin Films</b>	<b>136</b>
<b>G</b>	<b>Melanin transmittance</b>	<b>139</b>
<b>H</b>	<b>Ablation Study of Feather Rendering Model Parameters</b>	<b>140</b>



# List of Figures

1.1	Backlit portraits rendered using the separable hair scattering model and our model, compared with a photograph . . . . .	3
1.2	Studio for shooting soap bubbles . . . . .	5
1.3	Microscopic images of hairs of various racial origins . . . . .	6
1.4	Collimated light scattering from a hair cross-section . . . . .	7
1.5	The hierarchical structure of hummingbird feathers . . . . .	9
1.6	Microscopic image of purple barbules from a rock dove neck feather . . . . .	10
2.1	Microfacet model for rough surfaces . . . . .	12
2.2	Brute-force ray tracing <i>vs.</i> far-field approximation for hair . . .	13
2.3	Two types of curve primitives . . . . .	14
3.1	Spatially-varying iridescence of a soap bubble evolving over time	19
3.2	Cross-section of a soap film. . . . .	23
3.3	Thin-film interference colors . . . . .	24
3.4	Vertical thickness gradient of a soap bubble under gravity . . .	27
3.5	Staggered spherical grid . . . . .	29
3.6	Unrolled staggered spherical grid . . . . .	30
3.7	Bi-linear sampling of velocities at the pole. . . . .	31
3.8	Advecting a scalar field across the pole . . . . .	32
3.9	A single advection step for the velocity field on the sphere . . .	33
3.10	Light paths in soap film . . . . .	37
3.11	Light paths in a spherical soap bubble . . . . .	39
3.12	Keeping $\Gamma_0/R$ constant results in similar soap bubble appearance	42
3.13	Bubble Equilibrium state as a function of $R$ . . . . .	42
3.14	Gravity-dependent soap film flow . . . . .	43
3.15	Airflow-dependent soap film flow . . . . .	44
3.16	False-color visualization of a time-varying airflow and the resulting velocity field on a soap bubble . . . . .	45
3.17	Life of a soap bubble . . . . .	46
3.18	A vertical soap film with marginal regeneration . . . . .	47

3.19	Soap film flow simulations with/without viscosity term . . . . .	48
3.20	Black film on a soap bubble (photograph) . . . . .	48
4.1	Detailed view of backlit portraits rendered using the separable hair scattering model and our model, compared with a photograph . . . . .	51
4.2	An illustration of the geometry of our hair scattering model . . . . .	56
4.3	R, TT, and TRT scattering from a circular cross-section . . . . .	58
4.4	Parallel rays reflected off a smooth cylinder . . . . .	61
4.5	An elliptical cross-section . . . . .	61
4.6	Evaluating $S_{\text{TT}} + S_{\text{TRT}}$ as a function of $\theta_o$ and $\varphi_o$ . . . . .	65
4.7	R lobes of our models, the separable model, and the ground truth . . . . .	68
4.8	R lobes of our model, the non-separable model, and the ground truth . . . . .	70
4.9	TT plus TRT lobe for various illumination angles $\theta_i$ . . . . .	71
4.10	Validating our elliptical BCSDf against Monte Carlo simulation . . . . .	71
4.11	Comparing BCSDfs of circular and elliptical cross-sections . . . . .	72
4.12	Hair with increasing melanin concentration . . . . .	73
4.13	Backlit on hair modeled by the separable model and our model . . . . .	75
4.14	Hair with various roughness . . . . .	75
4.15	Circular and elliptical hair under various illumination angles . . . . .	76
4.16	Higher-order lobes under different incident angles in $\theta_i$ . . . . .	78
5.1	Multi-scale geometric structures of rock dove neck feathers, the BSDF measurements and full feather rendering . . . . .	83
5.2	Various mechanisms of structural color in barbules. . . . .	87
5.3	Colors of a thin keratin film as a function of thickness and incidence angle . . . . .	88
5.4	Illustration of thin-film interference . . . . .	90
5.5	Measured and simulated reflectance spectra of a green barbule . . . . .	91
5.6	Diagram of the imaging scatterometer . . . . .	92
5.7	SEM image and model of a unit barbule cell. . . . .	93
5.8	Transverse cross-section of a barb plane. . . . .	95
5.9	Uniform sampling of $h$ and $l$ . . . . .	96
5.10	Explicit and implicit feather geometry . . . . .	97
5.11	Comparison between calibrated photographs and renderings . . . . .	99
B.1	Construction of a multi-step scheme similar to an order-2 Runge-Kutta update. . . . .	124
F.1	Detailed illustration of thin-film interference . . . . .	136

F.2	Interference in a curved thin film . . . . .	138
H.1	Ablation study with parameters that differ from Chapter 5 . .	140



# List of Tables

3.1	Typical values and ranges of dimensional parameters used in our soap bubble simulation. . . . .	41
3.2	Typical values of dimensionless parameters. . . . .	41
5.1	The four characteristic scales of the feather model . . . . .	84
5.2	Important notations used in the feather model . . . . .	89



# List of Abbreviations

---

<b>Notation</b>	<b>Description</b>
BCSDF	Bidirectional Curve Scattering Distribution Function
BRDF	Bidirectional Reflectance Distribution Function
BSDF	Bidirectional Scattering Distribution Function
BTDF	Bidirectional Transmittance Distribution Function
BTF	Bidirectional Texture Function
CDF	Cumulative Distribution Function
CPU	Central Processing Unit
HDR	High Dynamic Range
IOR	Index of Refraction
LED	Light-Emitting Diode
MSP	MicroSpectroPhotometer
NDF	Normal Distribution Function
NURBS	Non-Uniform Rational B-Splines
PDF	Probability Density Function
RGB	Red Green Blue
SEM	Scanning Electron Microscope
spp	samples per pixel
sRGB	standard RGB
TAC	Total Appearance Capture
TEM	Transmission Electron Microscope

---



# 1. Introduction

## 1.1 Motivation

Physically based modeling uses physical laws to capture the essential properties of the subject of study, and uses various techniques to solve the resulting equation system efficiently and accurately, instead of using empirical models that match the reality only phenomenologically. Physically based modeling has already become standard in offline simulation, such as movies, commercials, and architectural visualization. With the recent advances in graphics hardware and techniques, they have become a growing trend even in video games, which require real-time performance; these advances also make it possible to model much finer details, which increase believability even further.

In the realm of natural phenomena, physically based modeling means solving the actual governing equations of the physical quantities rather than using synthesized, procedurally generated textures. This includes physically based simulation of atmosphere [45, 91], combustion [85] and snow avalanches [74], or simulation at finer scales, including ocean foam [132] and fluid flow on soap films [53, 25], to name a few. Sometimes, the developed techniques are so accurate and efficient that they are even applied outside of computer graphics, for example in weather nowcasting and natural hazard forecasting [119, 131].

In terms of producing the final images, physically based rendering aims at producing photorealistic images via simulating the interaction of light and matter as it is in the physical world. The central theorem is the rendering equation introduced by Kajiya [65], which formulates the outgoing radiance from a surface in terms of all the incoming light and the physical properties of the surface itself. In the same paper, he showed how to solve the equation by applying Monte Carlo path tracing, an imitation of photon transport in reality. Later, Veach [123] pushes this direction forward by developing a rigorous theoretical basis for bidirectional path tracing and proposing robust and efficient algorithms such as multiple importance sampling and metropolis light transport. When describing surface properties, microfacet models [21, 125] play an essential role because they can model various materials, including glass and metal. Special models are designed for

more complex and delicate materials, such as Morpho butterflies [80], spider webs [134] and gemstones [127].

Another important physical aspect is the wave nature of light. Previously, RGB representation dominated computer graphics as it mimics human trichromatic color vision. However, an RGB triplet can not uniquely define a color: its interpretation depends on the color space and the devices. Besides, RGB is only a sparse sampling of the visible light spectrum. In contrast, spectral rendering [129] samples densely from a continuum of the visible spectrum, supporting wavelength-dependent phenomena such as interference, diffraction, fluorescence, and metamerism out-of-the-box; it is therefore gradually gaining popularity against RGB rendering.

Recent advances in physically based modeling mainly focus on reducing image noises via producing high-quality Monte Carlo samples [13, 79] or neural denoising guided by physically meaningful features [147], simulating complex material appearances such as scratches [128], caustics, and glints [146, 135], representing the wave nature of light globally instead of locally [114], or simulating richer domains of natural phenomena. All in all, physically based modeling has achieved great photorealism that was never seen before.

In this dissertation, we revisit a few topics where previous works intend to be physically based but neglect important physical aspects at microscales. These topics are: fluid flow on soap bubbles (Chapter 3), hair rendering (Chapter 4) and feather rendering (Chapter 5).

Soap film is a long-studied topic. However, previous works in computer graphics only focus on physically modeling the evolving shape of the films, while ignoring the fluid flow on the surface of the soap film—researchers either assume the film thickness to be constant or apply ad-hoc noise textures, both bear no resemblance with photographs.

Modern physically based hair rendering is based on Marschner et al.’s work [76]. Although the Marschner model considers important physical characteristics of hair (including the circular cross-section, tilted cuticle scales, internal absorption, and radiant transfer), its separation of the scattering function into a longitudinal and an azimuthal component has no physical ground, thus fails to capture important highlights. The model also provides only an approximated solution for elliptical cross-sections.

In production, feathers are usually rendered via texture-based or hair scattering models, neglecting the complex hierarchical structures of feathers. Meanwhile, many birds demonstrate iridescent colors, which could only be approximated by mixing a hair shader and a thin-film shader.

We instead aim to close the above-mentioned gaps to improve photorealism of synthetic images. This is a cumulative work involving 3 publications,

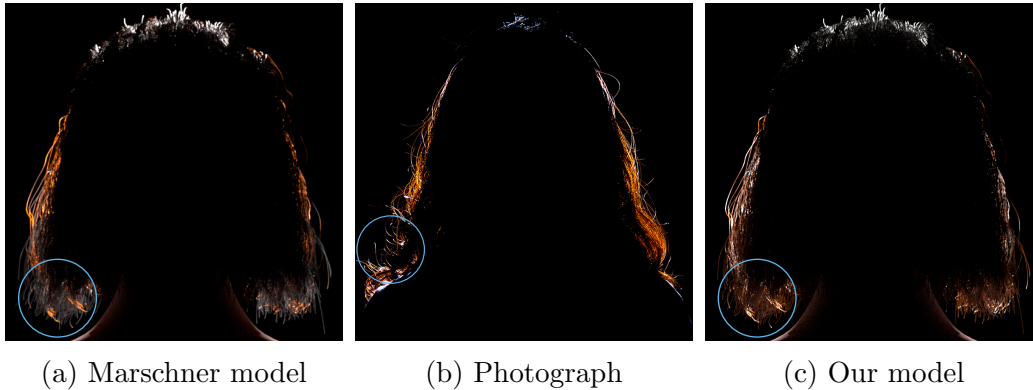


Figure 1.1: Although the Marschner model intends to be physically based by considering the geometric and optical properties of hairs, its assumption of the separability of the scattering function in the longitudinal and azimuthal direction is not well justified. Nevertheless, it has become the standard representation for following works until today. Before us, people also realized that the Marschner model has difficulties modeling the strong highlight in forward scattering. However, in production, this problem is usually bypassed by using different roughnesses for front and rear views, or by applying a cosine modulation in the longitudinal direction [28]. Both methods can match the appearance only phenomenologically. We instead build a physically based hair scattering model rooted in microfacet theory, and demonstrate the accuracy of our model compared with Monte Carlo simulation and photographs.

each presented in a separate chapter. In each chapter, we propose new governing equations for the respective problems as well as new algorithms to solve them; we also perform measurements to validate the photorealism of our models.

The following content is structured as follows: in Sections 1.2 to 1.3, we describe the physical properties of our objects of study, what previous works are lacking in describing these objects and what our models offer; in Chapter 2, we explain the background knowledge and necessary tools for understanding and solving the proposed problems; in Chapters 3 to 5, we present the respective publications on soap bubbles [53], human hairs [52], and rock dove neck feathers [54]; in Chapter 6, we conclude our achievements, discuss the influence of our works on following research and production renderers, and pose a few open problems.

## 1.2 Soap Film Dynamics

Few natural phenomena are so fascinating yet so easily accessible as soap bubbles and films, attracting the attention of children and grown-ups, laypeople and scholars alike. The beauty of soap bubbles is a result of their chemical, physical and mathematical aspects, interested readers can refer to Isenberg's book on soap films and soap bubbles [58] for a thorough explanation.

One charm of soap films lies in their shapes. Liquid surfaces have the tendency to minimize the surface tension and thus the free energy; therefore, they tend to evolve into minimal surfaces, such as spherical bubbles or catenoid between two rings. This property has even been used as an analog tool to solve mathematical problems. Soap film simulations in computer graphics also focused on the dynamic processes of their evolving into minimal surfaces.

Another charm of soap films lies in their colors. A soap film's iridescent colors are due to thin-film interference (Section 2.3) and depend on the film's thickness. Previous to our work [53], the computer graphics community did not look into the thickness dynamics of soap films. There have been theoretical works [20, 55, 56] in the mathematics and physics communities on the dynamics of soap film thicknesses, however, no full simulation was available. Although soap film flows are described by the same set of equations as other fluid flows, the *Navier-Stokes equations*, the extremely thin film and small-scale features make numerical simulations challenging.

A soap bubble consists of water and soap molecules. The majority of the soap molecules are adsorbed onto the surface so that their hydrophobic ends avoid contact with water. The existence of the soap molecules on the water surface, or *surfactant*, is why soap bubbles and films can last a long time before they burst. The surface tension of soap solution is lower than that of water; therefore, when a surface element is perturbed so that its area increases, the soap concentration will decrease, leading to a larger surface tension. Meanwhile, liquid surfaces tend to reduce the surface tension and thus the free energy; as a result, nearby soap molecules will be pushed to this region, restoring equilibrium. Since the film is so thin, an uncarefully chosen simulation step size could cause a massive amount of fluid gathering at the same place, or a sudden burst of the film. This kind of instability is often seen in a stiff mass-spring system.

In Section 3.4.3, we introduce a novel, unconditionally stable method for solving the surfactant concentration. We do so by combining the momentum equation and the surfactant transport equation to derive an implicit scheme, allowing significantly larger step sizes. In order to build a symmetric positive definite linear system, we choose to simulate in a spherical coordinate

system. This, unfortunately, introduces singularities at the poles, causing artifacts when advecting scalars or vectors near the poles. To address this problem, in Section 3.4.2, we develop an unconditionally stable advection scheme by constructing velocity-aligned local coordinate systems, effectively advecting quantities as if they were on the equator. This advection scheme could be applied to simulation on spherical coordinates in general. Besides the above-mentioned surface tension, in Sections 3.3.3 and 3.6.2 to 3.6.4, we also investigate other important sources that drive the fluid flow on a soap bubble: gravitational forces, air friction and evaporation. We also design a special shader for simulating multiple interactions between the soap bubble surfaces in Section 3.5.2. Finally, we set up a simple studio environment in the lab (Fig. 1.2) to capture real bubbles with a camera, and compare the photos with our renderings in Figs. 3.12, 3.14 and 3.15.

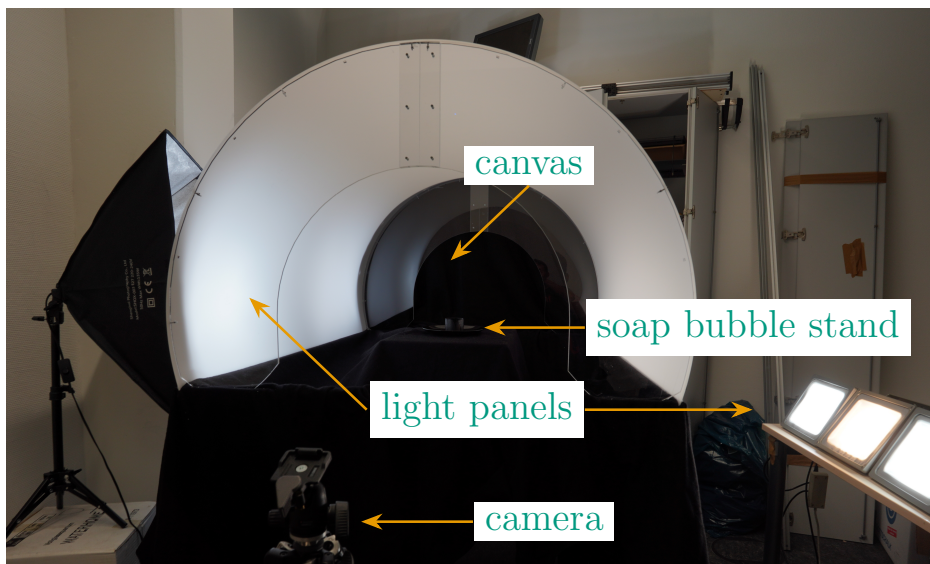


Figure 1.2: Studio for shooting soap bubbles

### 1.3 Hair Structure and Rendering

Hair is a much more popular topic than soap bubbles because it's vital in human character creation; a more accurate description of the hair's appearance increases the character's believability. Yet, hair rendering is difficult due to the complexity of light transport between the vast number of hairs.

Hair has three layers: the medulla, the cortex, and the cuticle [24]. The *medulla* is the innermost layer of hair; it is often narrow or absent in human

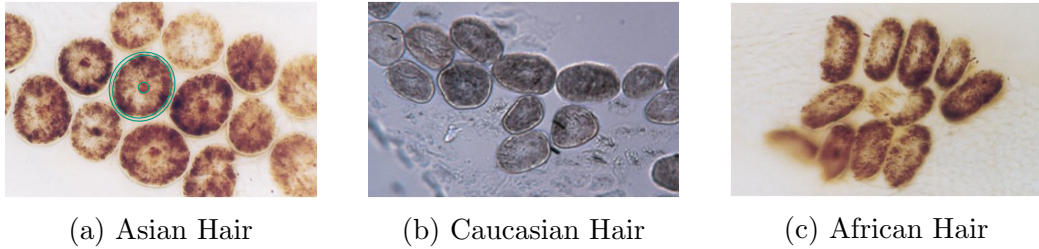


Figure 1.3: Microscopic images of hairs of various racial origins. The cross-sections vary from circular to elliptical. In (a), the three green circles from the innermost to the outermost one indicate medulla, cortex and cuticle. Images copyright: FBI Laboratory [24].

head hairs, compared to the distinct appearance in animal furs [138], its contributions to the reflectance is therefore neglected in hair scattering models. The *cortex* is the middle and the main part of hair, mainly consisting of keratin filaments and scattered melanin granules. While keratin is transparent (with a refractive index of 1.549 at 589 nm [73]), melanin granules absorb light (with a refractive index of  $1.648 + 0.06321i$  at 589 nm [112]), therefore, the amount of melanin determines the color of the hair. Due to the dominant presence of keratin and the relatively small difference in refractive indices between keratin and melanin, hair is usually modeled as a homogeneous cylinder made of keratin, with melanin only contributing to the absorption as light travels inside the cylinder [76, 26]. The *cuticle* is the outermost coating made of several overlapping layers of keratinized cells [12], with the tilt angle (around 2 to 4° [27]) pointing towards the root of the hair. The cuticle tilt alters the normal direction of the hair surface, and in particular causes the primary and secondary reflection from hair fibers to be shifted towards opposite directions along the axis (Fig. 4.10).

Almost all hair scattering models today are based on Marschner et al.'s work [76]. Their idea works as follows: According to Bravais law, the rays interacting with a dielectric cylinder from a certain inclination to the axis will exit at the same inclination, thus forming a cone. Therefore, a 3D analysis of light scattering can be reduced down to a 2D analysis in the cross-section plane by using a modified refractive index, so that the 4D scattering function  $S(\theta, \varphi)$  is factored into a product of two 2D terms: the longitudinal scattering function  $M(\theta)$  and the azimuthal scattering function  $N(\varphi)$ . However, the outgoing light only forms a specular cone when the interacting geometry is a perfectly specular cylinder. Hair has rough surfaces, plus the tilted cuticle scales, the outgoing rays from the same incoming angle do not form a cone anymore. Marschner et al. [76] deal with the problem by blurring  $M(\theta)$

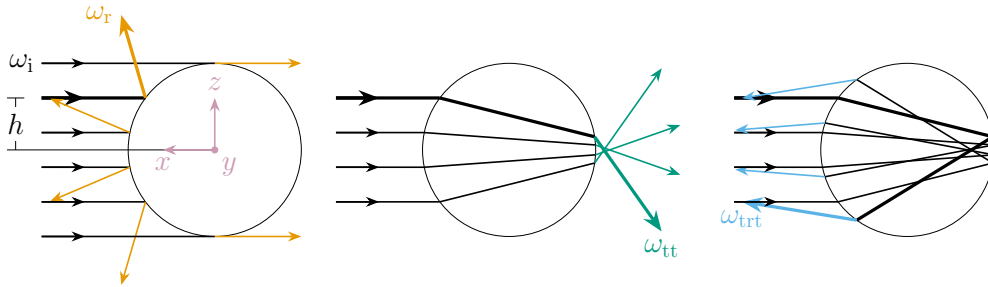


Figure 1.4: The incident light on a hair strand is assumed to be collimated. Components are grouped by the number of intersections.

along the axis using a Gaussian, and shifting  $M(\theta)$  by a certain amount depending on the number of interactions. However, this is only an arbitrary approximation of the underlying rough cylinder model.

Many subsequent works extend the Marschner model to animal furs [138, 137], improve the artistic control [19, 101] or performance [137, 27] of the model, but these are all built upon the separable assumption. The only exception is d'Eon et al.'s work [28], which points out that the longitudinal shift of the outgoing ray due to the scale tilt depends on the distance of the hit position to the axis (also called the azimuthal offset  $h$ , see Fig. 1.4). In particular, the angular shift of the primary reflection ray decreases as the offset increases, thus forming a focused response in forward scattering (*i.e.* when hair is observed against the illumination), which is verified in the measurements by Khungurn et al. [66]. D'Eon et al. compute the specular direction of the outgoing ray, and apply a cosine modulation of the original blurring along the longitude. This formulation intrinsically still separates the longitudinal and the azimuthal scattering functions, and is again a phenomenological approximation of the underlying rough cylinder model, as their result only matches the Monte Carlo simulation from a Beckmann microfacet distribution [9] with low roughness, and has a significant discrepancy with the ground-truth at grazing  $\theta$  angles.

Our approach [52] is rooted in microfacet theory [21, 48]. In computer graphics, a rough surface is usually modeled by a collection of small microfacets (also called microareas in the Trowbridge-Reitz distribution [120]), which scatter light in mirror directions. Different microfacet distributions are used to model different surface roughness. Similarly, to model a rough cylinder, one can also imagine small mirrors scattered on the cylinder surface and use the same microfacet model to describe light scattering, as there must exist a distribution function of the microfacet orientations on a rough cylinder. Following radiometry analysis by Cook and Torrance [21], it turns

out that such a distribution is basically just an integration of the planar distribution along the curve (Section 4.3.1). We show that this formulation gives rise to the focused highlight in the forward direction in Section 4.4.1 and Fig. 4.13. It even has an analytical solution for the GGX microfacet distribution, when the shadowing-masking term is left out (Appendix E). For subsequent interactions *e.g.* refraction and internal reflection, we adapt the formulation by Walter et al. [125] and also integrate along internal paths, resulting in higher-dimensional integrals, which we solve by combining Monte Carlo and deterministic numerical integration schemes (Section 4.3.4).

Because the basic idea is microfacets on a curved surface, our model naturally also works on elliptical cross-sections, which are the shapes of most hairs, as we have seen in Fig. 1.3. In that case, one also just integrates the distribution function along the elliptical curve (Section 4.3.3). Such a straightforward extension was not possible before. Since the curvature varies along the elliptical curve, light reflected from an elliptical cross-section shows different intensities along the azimuth (Fig. 4.11a). More interestingly, the secondary highlight is split into two distinct components pointing away from the backward scattering direction (Figs. 4.11b and 4.11c), showing a much brighter response when illuminated from the side, which is not present in hair with circular cross-sections (Fig. 4.15).

## 1.4 Feather Structure and Rendering

Compared to hair rendering, a much related but less studied topic is the realistic rendering of bird feathers. Feathers and hairs are both fiber-like, which explains why people use hair scattering models for feathers in production rendering [44]. However, in Section 1.3 we have shown the influence of the cross-sections on the appearance, and as we will see, the structure of feathers is much more complex than that of hairs, especially when considering particular complex effects like iridescence that occur in many bird species' plumage, so that a hair model is only partially transferable to feathers.

Generally, feathers are composed hierarchically (Fig. 1.5), starting with a central shaft that spans vane surfaces on both sides. Vanes consist of many fiber-like barbs; which are the parts normally seen with bare eyes. The barbs themselves consist of smaller barbules branching out to both sides. Finally, the barbules have non-cylindrical cross-sections, and may contain regularly aligned micro- or nanostructures.

Similar to human hairs, the general feather materials are keratin and melanin. Melanin is a source of *pigmentary* colors, since it absorbs light in a specific wavelength range. Other common pigments in avian plumage are

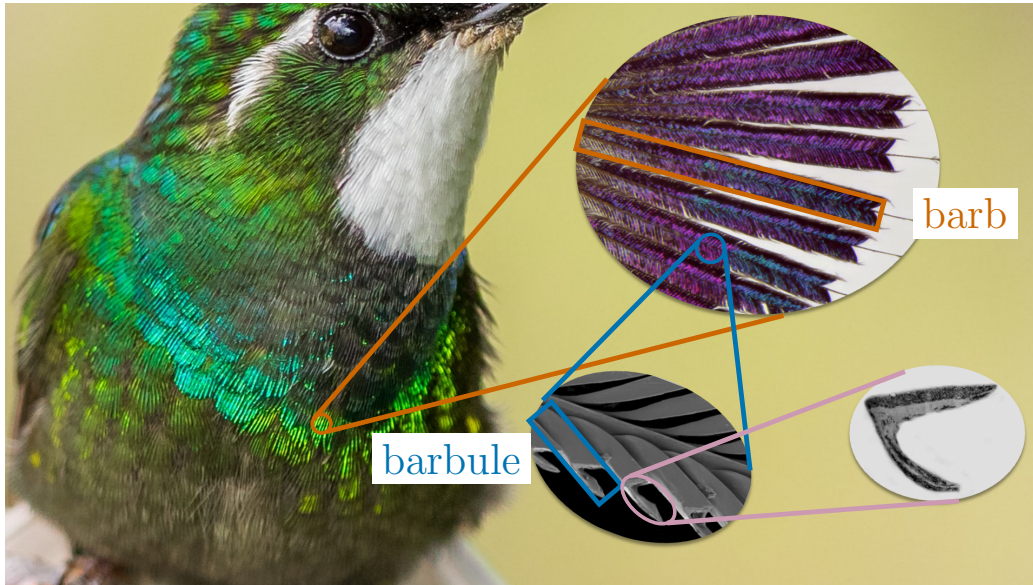


Figure 1.5: The hierarchical structure of hummingbird feathers. Photos taken from Giraldo et al. [42].

carotenoids, porphyrins, and psittacofulvins. More often [115], the regularly organized micro- and nanostructures of keratin and melanin cause *structural* colors by scattering light in a restricted wavelength range. Sometimes, structural colors also originate from the spongy barb.

The colors of rock dove neck feathers, the topic of Chapter 5, are a combination of structural and pigmentary sources. Their distinct two-color iridescence is a result of thin-film interference caused by the keratin films on the barbule surface. In certain thickness ranges (around 500 to 650nm), keratin films appear either green or purple, depending on the thickness and the viewing angle. Encapsulated by the keratin film are more or less randomly arranged melanin granules, which reflect visible light broad-bandly; they function as a background component that scatters light to a broader angular range and decreases the color saturation. However, the scattering behavior of rock dock neck feathers can only be partially explained by interference from the keratin thin film and the broad-band reflection from the melanin granules: it also depends on the millistructures, that is, the shape of the barbules and how they arrange themselves to form a barb. Microscope image (Fig. 1.6) shows that barbules are made of repeating cells with a curved shape, reflecting light to a broader angle. Moreover, the barbules are arranged regularly, forming a rather flat surface. In Section 1.3 we have discussed the idea of modeling a rough surface by a collection of microar-

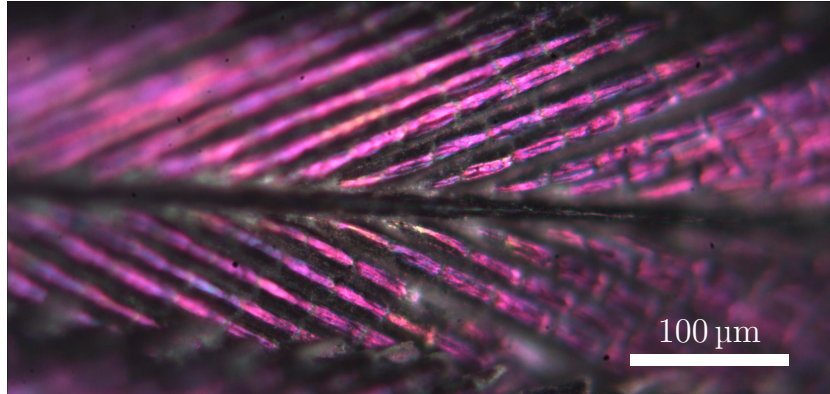


Figure 1.6: Microscopic image of purple barbules from a rock dove neck feather

eas, which is quite similar to our case here: a surface consisting of repeating microstructures.

We model the barb geometry explicitly as an extrusion of a circular arc (Fig. 5.10b), this is the macrosurface for our microfacet-like feather scattering model; we then formulate the microarea distribution of a barbule cell in Section 5.4.1, and model the randomness in the barbule orientation by applying a noise map at the barb scale, since such variation is also visible in the macroscale. There are two important aspects where our model differs from the microfacet model: first, because of the overlap, different part of the barbule is visible depending on the illumination and viewing angle, therefore, the shadowing-masking term needs special treatment, which we will discuss in Section 5.4.1; second, the barbule surface is a thin film, therefore, we need to account for thin-film interference (Section 2.3) instead of simple Fresnel reflection. Finally, we compare our rendered results with the measurement and photographs in Section 5.5, and identify great similarities.

## 2. Background

In this chapter, we give a thorough explanation of the background knowledge used throughout this dissertation. The BxDFs in Section 2.1 lays the foundation of both Chapters 4 and 5; thin-film interference in Section 2.3 is relevant for Chapters 3 and 4; we also introduce hair geometric primitive for Chapter 4.

### 2.1 BxDFs

BxDF is a family of bidirectional distribution functions describing how materials respond to incoming light. It is defined as the ratio between the differential outgoing radiance (radiant flux per unit projected area per solid angle)  $dL_o(\omega_o)$  and the differential incoming irradiance (radiant flux per unit area)  $dE_i(\omega_i)$  [94]

$$f(\omega_i, \omega_o) = \frac{dL_o(\omega_o)}{dE_i(\omega_i)} = \frac{dL_o(\omega_o)}{L_i(\omega_i) \cos \theta_i d\omega_i}, \quad (2.1)$$

where  $\omega_{i,o}$  are incoming and outgoing directions, respectively, and  $\theta_i$  is the angle between the incoming light and the surface normal. Integrating Eq. (2.1) over the sphere, we obtain the outgoing radiance

$$L_o(\omega_o) = \int L_i(\omega_i) f(\omega_i, \omega_o) \cos \theta_i d\omega_i. \quad (2.2)$$

#### 2.1.1 Microfacet BSDF

In computer graphics, microfacet theory [49] is the standard method to model surface roughness, where a macrosurface is presumed to be a collection of small mirrors that reflect light at the same angle as the incoming light. The distribution of the microfacets' normals is called the *normal distribution function* (NDF)  $D(\omega_h)$ , it appears in the *bidirectional reflectance distribution function* (BRDF) as

$$f_r(\omega_i, \omega_o) = \frac{F(\omega_h, \omega_o) G(\omega_o, \omega_i, \omega_h) D(\omega_h)}{4 \cos \theta_o \cos \theta_i}, \quad (2.3)$$

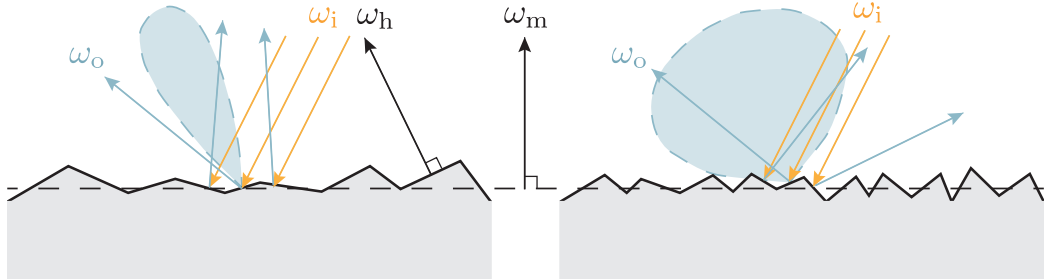


Figure 2.1: A *macrosurface* with normal direction  $\omega_m$  is modeled as a collection of small perfect mirrors, or *microfacets*. On the right, the microfacets' normal directions  $\omega_h$  have a larger variance, the surface therefore appears rougher.

with  $F$  being the Fresnel term,  $G$  the shadowing-masking term, and the direction of  $\omega_h$  is given by  $\omega_i + \omega_o$ .

Defined above is the reflection in the upper hemisphere around the macrosurface normal. If the surface is translucent, light is also refracted into the lower hemisphere, giving the *bidirectional transmittance distribution function* (BTDF)

$$f_t(\omega_i, \omega_o) = \frac{T(\omega_h, \omega_o)G(\omega_o, \omega_i, \omega_h)D(\omega_h)(\omega_i \cdot \omega_h)(\omega_o \cdot \omega_h)}{\|\omega_o + \eta^{-1}\omega_i\|^2 \cos \theta_o \cos \theta_i}, \quad (2.4)$$

with  $T$  being the Fresnel transmittance,  $\eta$  the relative refractive index of the media of the outgoing ray w.r.t. that of the incoming ray, and  $\|\cdot\|^2$  the squared norm. In the transmission case, the direction of  $\omega_h$  is given by  $-\omega_o - \eta^{-1}\omega_i$ , exactly the term in  $\|\cdot\|$ .

BRDF and BTDF combined give the *bidirectional scattering distribution function* (BSDF) in the complete sphere around the incident position.

In the following chapters, we will see extensions of the microfacet model, that is, the same formulation can be used even when the underlying macrosurface is not a plane, but a curved surface (Chapter 4), or when the microfacets are not “facets”, but overlapping surfels, or smooth microareas (Chapter 5).

### 2.1.2 BCSDF

The BSDF defined in the last section is used to describe the scattering behavior of a surface. When light is scattered from a fiber, *e.g.* human hair or animal fur, the *bidirectional curve scattering distribution function* (BCSDF) is used instead, derived from analogies of radiance and irradiance defined per

fiber length

$$S(\omega_i, \omega_o) = \frac{d\bar{L}_o(\omega_o)}{d\bar{E}_i(\omega_i)}, \quad (2.5)$$

where  $\bar{L}$  is radiant flux per unit projected fiber length per solid angle, and  $\bar{E}$  is radiant flux per unit fiber length, resulting in the rendering integral

$$L_o(\omega_o) = \frac{D_i}{D_o} \int L_i(\omega_i) S(\omega_i, \omega_o) \cos \theta_i d\omega_i, \quad (2.6)$$

with  $D_{i,o}$  being the diameter viewed from the incoming and outgoing directions, respectively. For fibers with circular cross-sections, this ratio is 1. In Section 4.3.3, we will discuss the case of elliptical cross-sections. Despite the similarity of Eq. (2.6) to Eq. (2.2), the  $\theta_i$  in both equations are different: in Eq. (2.2),  $\theta_i$  is the angle between the incoming light and the surface normal, *i.e.*  $\cos \theta_i = \langle \omega_i, \omega_m \rangle$ , whereas in Eq. (2.6),  $\theta_i$  is the angle between the incoming light and the cross-section plane  $x-z$  (Figs. 1.4 and 4.2), *i.e.*  $\sin \theta_i = \langle \omega_i, \vec{e}_y \rangle$ , with  $\vec{e}_y$  being the unit vector along the  $y$  axis.

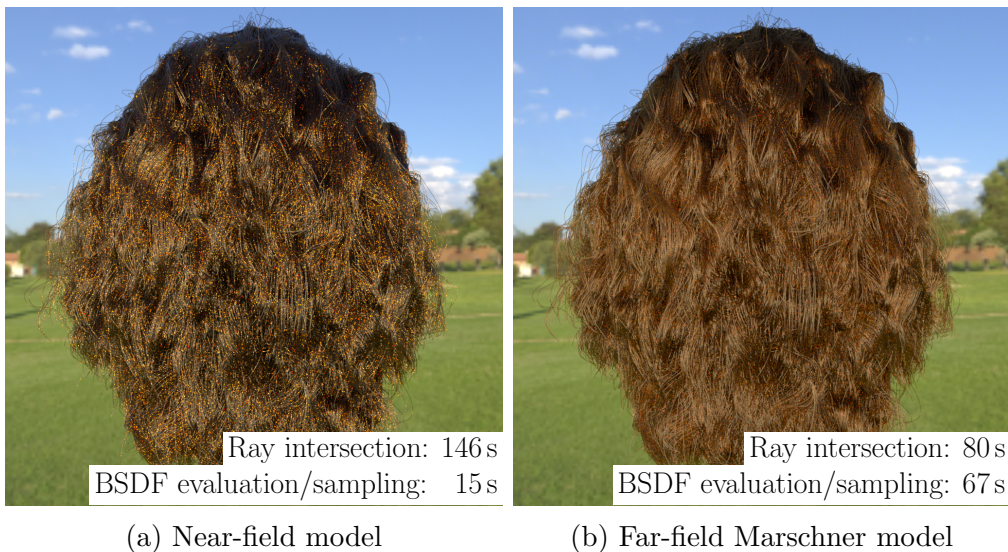


Figure 2.2: Comparing brute-force ray tracing (left) with a far-field approximation (right). Both images have a resolution of  $1024 \times 1024$  and took 3 min to render on an Apple M1 8-core CPU. On the left, hair is modeled by rough dielectric cylinders with absorption. Most of the time is spent on ray intersection, and the image is very noisy. On the right, hair is modeled by ray-facing stripes with BCSDF applied. BSDF evaluation now takes much longer, but the ray intersection time is reduced, and the image also has much better convergence.

Although Marschner et al. [76] first formulated the scattering function  $S(\omega_i, \omega_o)$  for hairs, it was Arno and Zinke [149] who performed the first systematic derivation of radiance transfer at a hair, or more generally, a fiber. Arno and Zinke [149] also pointed out that the scattering function used by Marschner et al. [76] is a far-field approximation of the near-field model integrated along the fiber width, and name the former BCSDf. *Far-field* means that a fiber is illuminated and viewed from sufficiently large distances and hence takes up less than one pixel on the screen, so that the exact incident and outgoing position along the fiber width does not matter; in this case, we can assume collimated light (Fig. 1.4). Local illumination between fibers is also assumed to be collimated. Because the hair fiber is very thin, the probability of hitting a particular fiber is low; by summarizing the scattering behavior from the whole width, we reduce the samples needed for convergence, at the tradeoff of longer BSDF computation times each time the ray hits the fiber. In effect, one achieves less noisy results in the same rendering times when a far-field model is applicable (Fig. 2.2).

## 2.2 Hair Primitive

Although triangle meshes are ubiquitous in shape representation, it is more efficient to use interpolating *curves* when modeling hair.



Figure 2.3: Curve primitives. *Left*: a circular cross-section swept along a curve. *Right*: a ray-facing stripe.

Ideally, a hair fiber is formed by sweeping a circular cross-section along a curve (Fig. 2.3 left). Ray intersection with a curve primitive is often approximated by recursively splitting the current curve section in half [94], until it spans less than one pixel and can be approximated by a line segment (or a cylinder, when considering the curve width). For far-field models, the exact hit position on the cylinder does not matter, therefore, in practice, a *ray-facing stripe* (Fig. 2.3 right) is used to replace the cylinder, saving the computational expense of solving a quadratic equation. Recently, there have been approaches to intersect a polynomial curve directly and efficiently without recursive subdivisions [98, 144], however, they only support circular cross-sections (with varying radius along the curve), not elliptical cross-sections as

we will need in Section 4.3.3. Therefore, we stick with the ray-facing stripe representation.

For elliptical cross-sections, one also needs to figure out the orientation along the curve. Without previous knowledge, we assume the semi-minor axis to be aligned with the curvature vector, as a long and thin structure, such as a wire, is most easily bent along its thinnest direction.

## 2.3 Thin-film Interference

When the film thickness is at the scale of visible light wavelengths, we need to consider the wave nature of light. The complex representation of an electric field vector is

$$E = |E|e^{i\phi}, \quad (2.7)$$

with  $\phi = \omega t + \epsilon$  accounting for the angular temporal frequency  $\omega$ , time  $t$ , and phase  $\epsilon$ .

In its simplest form, a thin film has an infinite extent, sandwiched between two semi-infinite media (both are air in our case). All media are homogeneous and isotropic. When light is incident from air on the thin film, it is partially reflected by an amplitude of  $r_{12}$  and partially transmitted by an amplitude of  $t_{12}$ . The transmitted part enters the thin film and is partially reflected and transmitted repeatedly at the film-air interfaces by amplitudes of  $r_{21}$  and  $t_{21}$ , respectively (see Fig. F.1. For a flat thin film, the reflected rays are parallel and interfere with each other, with the phase difference of successive rays being  $\Delta\psi$ . The transmitted rays are also parallel and have the same phase difference  $\Delta\psi$ . The reflection (transmission) coefficient is then obtained by summing up an infinite series of the reflected (transmitted) rays, which is given by the Airy formula [140]

$$r = r_{12} + \frac{t_{12}r_{21}t_{21}e^{i\Delta\psi}}{1 - r_{21}^2e^{i\Delta\psi}}, \quad t = \frac{t_{12}t_{21}}{1 - r_{21}^2e^{i\Delta\psi}}. \quad (2.8)$$

the full expression of the infinite series can be found in Appendix F.

For a soap bubble (Chapter 3) or a feather barbule (Chapter 5), however, the two interfaces of the thin film is not parallel. Also in Appendix F, we perform a 2D analysis on a thin film with curvature, and found out that the exact reflection coefficient can be very well approximated by a flat thin film, except when the curvature radius is too small, even smaller than a grid size in Chapter 3 or a barbule width in Chapter 5. Therefore, in both chapters, we assume the film to be locally flat.



# 3. Chemomechanical Simulation of Soap Film Flow on Spherical Bubbles

The content of this chapter has been published as:

Weizhen Huang, Julian Iseringhausen, Tom Kneiphof, Ziyin Qu, Chenfanfu Jiang, and Matthias B Hullin.  
Chemomechanical simulation of soap film flow on spherical bubbles.  
In *ACM Transactions on Graphics (TOG)*, 39(4):41–1, 2020.  
DOI: 10.1145/3386569.3392094

## Summary

Numerous research works have focused on the dynamics of soap bubbles or films, exploring various shapes such as soap films in frames, clusters of bubbles [60], and bursting bubbles [148]. However, the colorful patterns resulting from fluid flow in soap films, which contribute to their great beauty, have not been replicated in previous works.

In the chapter, we derive the governing equation of fluid flow on soap bubbles and identify the essential factors, including surfactant concentration, gravitational force, and air friction. To alleviate numerical issues arising from mixing substantially smaller radial dimension with larger lateral dimensions, we employ lubrication theory to transform the 3D governing equation into a 2D equation, treating the film thickness as an additional variable dependent on the lateral coordinates.

The resulting equation system is discretized for numerical simulation. We adopt a spherical coordinate system, which is convenient for defining variables due to the spherical nature of soap bubbles; additionally, a regular grid yields a symmetric positive definite linear system, benefiting the numerical solver. However, using a spherical coordinate system introduces singularities at the poles, which can cause numerical problems when advecting quantities near

the poles. To overcome this, we construct velocity-aligned local coordinate systems, effectively treating every point on the sphere as if on the equator.

Preserving the fine details of fluid flow on soap bubbles requires addressing numerical diffusion, caused by repeatedly interpolating values from a coordinate system with finite resolution. We tackle this problem by keeping a bidirectional mapping [96], consisting of a backward mapping that maps the current grid point to its position at the initial time step for interpolation, and a forward mapping to accumulate changes along the flow. This approach ensures that values are always interpolated from the initial time step instead of repeatedly interpolated from the previous time step.

After advection, additional terms are applied with a single time step update. Due to the elasticity resulting from the concentration gradient term, the system requires extremely small step sizes when solved explicitly. To overcome this limitation, we propose a concentration split step to solve the concentration gradient term implicitly, while using explicit updates for other terms. The resulting sparse matrix is solved using a conjugate gradient method with the AmgX library.

Furthermore, we capture soap bubble footage in the lab and observed significant similarities with our models. We are able to recreate the stripe-like features resulting from velocity gradients and shear motion, the waterdrop shapes with tails floating up- or downwards due to local thickness differences, thinning due to evaporation, and thickness gradients resulting from gravity.

One drawback of our model is its limitation to spherical shape. Extending the model to more general shapes would require different coordinate systems. Additionally, our model neglects viscosity, which would require an extra update step. Another challenge lies in simulating black films with extremely small thickness, where the force gradient is so large and therefore requires much finer resolutions. These aspects are left for future works.

**Author Contribution:** In this research, I conducted literature review, derived and simplified the governing equation of the fluid system. Additionally, I designed an unconditionally stable advection scheme and implemented all simulation algorithms, including advection, external forces, bidirectional mapping, and the conjugate gradient solver in AmgX. Furthermore, I conducted the experiments with together with Matthias Hullin.

The initial idea was proposed by Matthias Hullin. Chenfanfu Jiang contributed the concentration splitting scheme. Ziyin Qu provided valuable suggestions for the conjugate gradient methods. Tom Kneiphof and Matthias Hullin contributed to implementing the renderer. All the co-authors assisted in revising the paper.



Figure 3.1: Spatially-varying iridescence of a soap bubble evolving over time (left to right). The complex interplay of soap and water induces a complex flow on the film surface, resulting in an ever changing distribution of film thickness and hence a highly dynamic iridescent texture. This image was simulated using the method described in this chapter, and path-traced in Mitsuba [62] using a custom shader under environment lighting.

## Abstract

Soap bubbles are widely appreciated for their fragile nature and their colorful appearance. The natural sciences and, in extension, computer graphics, have comprehensively studied the mechanical behavior of films and foams, as well as the optical properties of thin liquid layers. In this chapter, we focus on the dynamics of material flow within the soap film, which results in fascinating, extremely detailed patterns. This flow is characterized by a complex coupling between surfactant concentration and Marangoni surface tension. We propose a novel chemomechanical simulation framework rooted in lubrication theory, which makes use of a custom semi-Lagrangian advection solver to enable the simulation of soap film dynamics on spherical bubbles both in free flow as well as under body forces such as gravity or external air flow. By comparing our simulated outcomes to videos of real-world soap bubbles recorded in a studio environment, we show that our framework, for the first time, closely recreates a wide range of dynamic effects that are also observed in experiment.

## 3.1 Motivation

The beauty of soap films and bubbles is of great appeal to people of all ages and cultures, and the scientific community is no exception. In the computer graphics community, it is now widely understood how films, bubbles and foams form, evolve and break. On the rendering side, it has become possible to recreate their characteristic iridescent appearance in physically based

renderers. The main parameter governing this appearance, the thickness of the film, has so far only been driven using ad-hoc noise textures [43], or was assumed to be constant. The resulting renderings appear largely plausible but static, as they lack the rich dynamics known from real-world soap films.

In this chapter, we aim to close this gap in order to achieve greater realism. We do so by contributing a chemomechanical framework targeted specifically at simulating the rich and detailed microscopic flow on spherical soap bubbles. Our framework employs a leading-order approximation for the soap film dynamics developed by Chomaz [20], Ida and Miksis [55]. A soap bubble is modeled as a two-dimensional flow on a static spherical surface with two associated scalar fields: the film thickness and the soap concentration. We are able to show that this state-of-the-art model, paired with a custom solver, is capable of expressing the intricate flows found on real-world soap bubbles (Fig. 3.1) under the mutual influence of mechanical stress, film thickness and surfactant concentration as well as body and surface forces like gravity and air friction. Our simulation is performed on a staggered grid, using finite differences in space and time. An advection scheme based on BiMocq<sup>2</sup> [96] minimizes numerical dissipation in order to prevent fine details from washing out over time. The resulting thickness maps are presented in real time using a custom, very efficient polarization-aware spectral rendering scheme.

Besides the underlying physical model, our framework is enabled by the following key contributions:

- We propose a novel advection scheme for vector and scalar quantities in spherical coordinates. Our scheme, which constructs a local coordinate frame aligned with the direction of the flow, is unconditionally stable and maintains continuous behavior even near and across the poles.
- We propose an implicit update step for the soap concentration, which avoids solving a stiff indefinite system and enables the use of significantly larger time steps when applying body forces.
- We introduce a novel real-time shader that is designed to reflect spectrally and polarization-dependent effects under environment lighting in a physically accurate manner. This even holds for contributions which are reflected multiple times in a spherical bubble.
- We investigate the influence of material parameters, geometric scale and external forces on the flow, and compare our results to real-world examples captured under lab conditions.

## 3.2 Related Work

With their tendency to evolve into minimal surfaces, soap films embody a fundamental mathematical and physical principle in a way that is immediately relatable and fascinating to experts and laypersons alike. Consequently, they have inspired a large body of research in mathematics, physics and materials science. Some mathematicians even went so far as to use them as analog computers to solve mathematical minimization problems [58]. Within the computer graphics community, the geometric properties of minimal surfaces as well as the formation, evolution and destruction of films, bubbles and foams have inspired a large number of groundbreaking works [122, 43, 61, 60, 148, 68, 23].

Besides their geometry, the beauty of soap bubbles also stems from their dynamic iridescent patterns. The chaotic mixing, highly non-linear vortices and turbulence of the fluid flow are not only visually interesting, but they have also led to a body of scientific work that is just as varied and colorful as its subject of study. Examples range from the visualization and study of 2D flow [40] or using soap bubbles as a small-scale surrogate model for planetary atmospheres [78, 106] via the visualization of sound and music [39] to using soap films as volatile display surfaces [88]. In computer graphics, the simple optical effect behind the characteristic iridescent colors (thin-film interference) has long been understood and used [108, 117, 43, 63, 61, 10, 69]. However, the film thickness, which is the main governing parameter besides the liquid's refractive index, has rarely been driven by proper physical simulation. While some works [102, 103, 148] have coupled thickness in their models, they use it more or less as an intermediate variable that influences the macroscopic motion and serves as a bursting condition. Most recently, such models have been equipped with the ability to propagate turbulent flow across Plateau boundaries [59]. In contrast, our goal is to simulate the rich and detailed dynamics of the microscopic flow that is observable through thin film interference, while staying as close as possible to a state-of-the-art physical model.

We turn to the fluid mechanics and physics communities, where several comprehensive models for soap film flow have been devised. Chomaz [20] derived a highly accurate model for the dynamics of a flat soap film, which is based on the asymptotic lubrication theory, assuming the thickness of the film is small compared to its lateral extent. The main contribution of that work is on the construction of similarities between soap film flows and compressible fluid flows in a planar, two-dimensional domain. The model provided by Ida and Miksis [55] is in principle capable of expressing general and time-varying three-dimensional soap films. In order to simulate flow using their model [56],

they employ a pseudospectral Chebychev spatial collocation and restrict the solution to the one-dimensional axisymmetric case.

Since the pioneering work by Foster and Metaxas [34], physics-based animation of fluids has been an important topic in computer graphics due to its wide range of applications for capturing effects of smoke [31], free surface flow [33], or fire [84]. We note that even lubrication theory, which forms the foundation of our framework, has at least once before been employed by other members of the computer graphics community: Azencot et al. [3] used it to simulate the flow of thin liquid films across solid surfaces. Regarding the geometric discretization, various possible choices exist [15, 32, 2, 57, 75]. Grid-based Eulerian simulation of fluid remains popular and widely adopted due to its superior efficiency and versatility, despite its well-known problems in numerical diffusion. In graphics, the semi-Lagrangian advection scheme presented by Stam [109] builds the foundation for many more advanced future developments on Eulerian fluids, including some recent impressively successful examples [145, 82, 96]. Indeed, the advection equation is such a mathematically simple, yet numerically challenging equation that consistently draws a lot of attention. The difficulty is pronounced at an even higher level when one tries to solve for fluid dynamics on a spherical geometry [51, 139] due to the notoriously difficult “pole singularity problem” [97]. In this chapter, we look into an even more challenging scenario where we need to efficiently and robustly advect multiple physical quantities related to the chemomechanical physics on a soap film.

### 3.3 Physical Model

The mechanical properties of soap solutions are characterized by the interplay of water and the soap dissolved in it. Soap molecules, which have a polar (hydrophobic) and a non-polar (hydrophilic) end, tend to settle at the water surface, so that their hydrophobic part can avoid the contact with water. As a result, the soap concentration at surfaces is usually much higher than in the bulk fluid. Soap further acts as a surfactant, *i.e.*, the presence of soap molecules reduces the surface tension of the fluid. When the distance between soap molecules at the surface increases, surface tension increases accordingly. By adding soap to water, it becomes possible to make bubbles that can last several seconds to minutes, since the surface tension prevents them from bursting. The resulting structure of soap films consists of three layers [22]: two water-air interfaces populated by soap molecules and a thin layer of bulk fluid in between (Fig. 3.2). The thickness of a soap film is usually around  $1\mu\text{m}$ , which explains the colorful interference between light

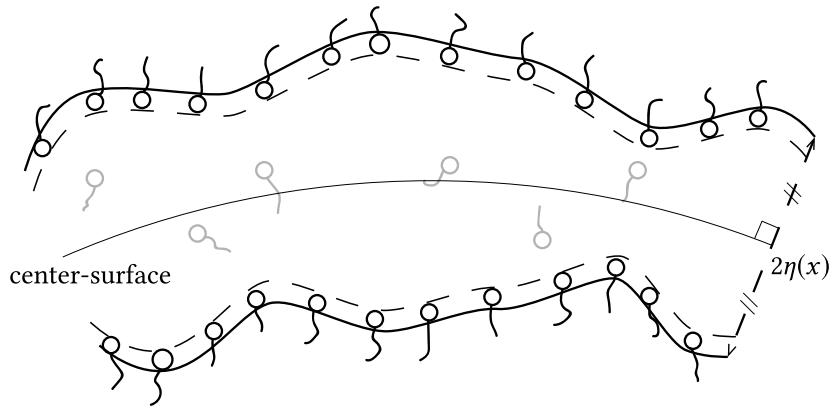


Figure 3.2: Cross-section of a soap film (image adapted from Couder et al. [22]). A thin layer of liquid (thickness  $2\eta$ ) is centered around a macroscopically defined surface. The polar chemistry of surfactant molecules causes them to concentrate at the liquid-air interface. We assume the number of soap molecules in the bulk fluid (here marked in gray) to be negligible.

reflected at the two interfaces (Fig. 3.3).

As a soap solution's refractive index is only weakly affected by the soap concentration, the two dominant influences on the color of the film are its large-scale geometry and hence the viewing angle, and the spatially varying thickness of the fluid layer. For the purpose of this work, we assume the shape of the bubble to be fixed. This leaves material transport within the film manifold as the main source of texture. In order to recreate the intricate dynamics found in real-world soap films, we have to understand, model and simulate this flow.

### 3.3.1 Governing equations in 3D

We formulate the fluid flow in terms of the incompressible three-dimensional Navier-Stokes equations,

$$\frac{\partial \vec{u}}{\partial t} + (\vec{u} \cdot \nabla) \vec{u} = \frac{1}{\rho} \nabla \cdot \sigma + \vec{f}, \quad (3.1a)$$

$$\nabla \cdot \vec{u} = 0, \quad (3.1b)$$

where  $\nabla$  is the nabla operator in three dimensions,  $\vec{u}$  is the fluid velocity,  $\sigma$  is the Cauchy stress tensor [8, Ch. 1.3],  $\rho$  is the mass density, and  $\vec{f}$  represents body accelerations such as gravity and air friction.

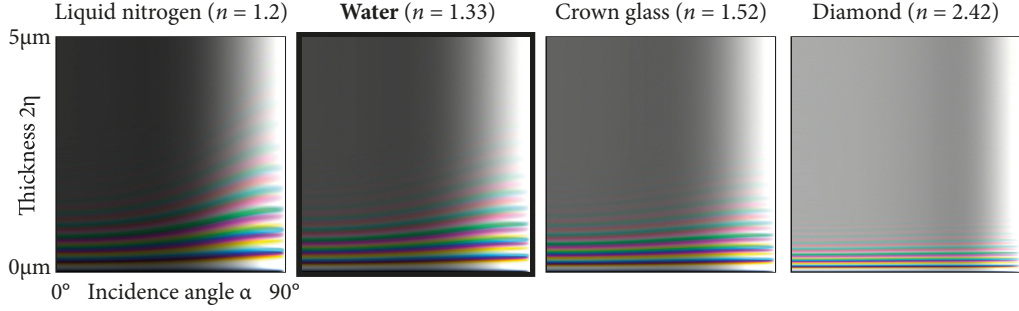


Figure 3.3: Interference color of light reflected by a thin layer of dielectric as a function of film thickness and incidence angle. Shown are simulations with a spectral resolution of 5nm for materials of different refractive index, including the most relevant material for our purpose, water. Colors are scaled so that white corresponds to a reflectance of 100%. We refer the reader to established literature [43, 10] on how to compute these colors. Somewhat counterintuitively, we note that the optical path difference *decreases* with increasing angle. Therefore, under oblique observation it takes a *thicker* film to produce the same color.

At a film surface, the stress condition applies as [55, 22]

$$\sigma \cdot \vec{n} = (2\mathcal{C}\gamma - p_a)\vec{n} + \nabla_s \gamma, \quad (3.2)$$

where  $\vec{n}$  is the outward normal vector at the respective surface,  $p_a$  the air pressure,  $\gamma$  the surface tension, and  $2\mathcal{C} = -\nabla \cdot \vec{n}$  is twice the mean surface curvature. In general, the values of these quantities differ between one surface of the film and the other. The 2D gradient operator  $\nabla_s$  within the surface acts on a scalar field  $\Phi$  as

$$\nabla_s \Phi = \nabla \Phi - \mathbf{n}(\mathbf{n} \cdot \nabla \Phi). \quad (3.3)$$

The surface tension depends on the surfactant concentration  $\Gamma$ , *i.e.*, the concentration of soap molecules on the surface,

$$\gamma = \gamma_a - \gamma_r \Gamma, \quad (3.4)$$

where  $\gamma_a$  is the surface tension of pure water, and  $\gamma_r$  accounts for the elasticity of the film. In the small concentration range,  $\gamma_r$  is considered to be constant [22].

Finally, the surfactant concentration  $\Gamma$  is driven by the advection-diffusion equation

$$\frac{\partial \Gamma}{\partial t} + \nabla_s \cdot (\vec{u}\Gamma) = D_s (\nabla_s)^2 \Gamma, \quad (3.5)$$

with  $D_s$  being the diffusivity for surfactant molecules.

### 3.3.2 Thin-film analysis and governing equation on spheres

In the following, we will restrict ourselves to spherical bubbles with radius  $R$ . For small (centimeter-sized) bubbles, this approximation is reasonable. It is thus convenient to parameterize the problem in spherical coordinates  $(r, \theta, \phi)$ . The fluid velocity  $\vec{u}$  then reads as

$$\vec{u} = (u_r, u_\theta, u_\phi)^\top. \quad (3.6)$$

We further note that the thickness of a soap bubble is very small compared to its lateral extent. Using lubrication theory [99, 90], we reduce the three-dimensional problem to a two-dimensional one. The extent of the film along the normal direction (the thickness) is introduced as a variable rather than a third dimension of the simulation domain. Suppose the inner and outer sides of the bubble are symmetrically deformed with half thickness  $\eta$  to either side (Fig. 3.2), then the kinematic condition (see Section D.1) describing the interaction between the time and spatially varying film thickness  $\eta = \eta(\theta, \phi, t)$  and the velocity  $\vec{u}$  at the interface  $r = R \pm \eta$  can be written as

$$\frac{\partial \eta}{\partial t} + \frac{u_\theta}{R} \frac{\partial \eta}{\partial \theta} + \frac{u_\phi}{R \sin \theta} \frac{\partial \eta}{\partial \phi} = \pm u_r. \quad (3.7)$$

With the mean half thickness  $\eta_0$  and the expansion parameter  $\epsilon = \eta_0/R$ , we non-dimensionalize the variables as

$$\begin{aligned} \eta &= \eta_0 \eta', & u_\theta &= U u'_\theta, & u_\phi &= U u'_\phi, & \sigma &= \frac{\mu U}{R} \sigma', \\ u_r &= \epsilon U u'_r, & r &= R + \epsilon R r', & t &= \frac{R}{U} t', & \Gamma &= \Gamma_0 \Gamma', & p &= \frac{\mu U}{R \epsilon} p', \end{aligned} \quad (3.8)$$

where  $U$  is the characteristic velocity and  $\Gamma_0$  is the mean surfactant concentration. We substitute these variables in Eqs. (3.1), (3.2), (3.4), (3.5) and (3.7), expand  $\vec{u}$ ,  $\Gamma$  and  $\eta$  asymptotically with a power series, and drop all terms except those with leading order of  $\epsilon$  (see Chomaz and Miksis et al.'s works [20, 55] for more details). Note that our non-dimensionalization is adapted to spherical coordinates and thus differs from the literature examples. The nabla operator  $\nabla$  now only acts within the surface,

$$\nabla = \nabla_s = \vec{e}_\theta \frac{\partial}{\partial \theta} + \frac{1}{\sin \theta} \vec{e}_\phi \frac{\partial}{\partial \phi}, \quad (3.9)$$

where  $\vec{e}_\theta$  and  $\vec{e}_\phi$  are the respective basis vectors. The governing equations are thus reduced to

$$\left[ \begin{array}{l} \frac{D\vec{u}'}{Dt'} = -\frac{M}{\eta'} \nabla \Gamma' + \vec{f} + Re^{-1} \vec{V}, \\ \frac{D\Gamma'}{Dt'} = -\Gamma' \nabla \cdot \vec{u}' + D'_s \nabla^2 \Gamma', \\ \frac{D\eta'}{Dt'} = -\eta' \nabla \cdot \vec{u}', \end{array} \right. \quad (3.10a)$$

$$\left[ \begin{array}{l} \frac{D\Gamma'}{Dt'} = -\Gamma' \nabla \cdot \vec{u}' + D'_s \nabla^2 \Gamma', \\ \frac{D\eta'}{Dt'} = -\eta' \nabla \cdot \vec{u}', \end{array} \right. \quad (3.10b)$$

$$\left[ \begin{array}{l} \frac{D\eta'}{Dt'} = -\eta' \nabla \cdot \vec{u}', \end{array} \right. \quad (3.10c)$$

where  $M = \Gamma_0 \gamma_r / \rho \eta_0 U^2$  is the Marangoni number,  $Re = UR\rho/\mu$  is the Reynolds number,  $\mu$  and  $\rho$  are the dynamic viscosity and the mass density of the soap solution, respectively. The thermodynamic quantity  $\gamma_r = \bar{R}T$  combines gas constant  $\bar{R}$  and temperature  $T$  [22].  $D'_s = D_s/UR$  is the scaled diffusivity, and the total derivative

$$\frac{D}{Dt'} = \frac{\partial}{\partial t'} + \vec{u}' \cdot \nabla. \quad (3.11)$$

The vector  $\vec{V} = (V_\theta, V_\phi)^\top$  represents viscous terms including second order terms as

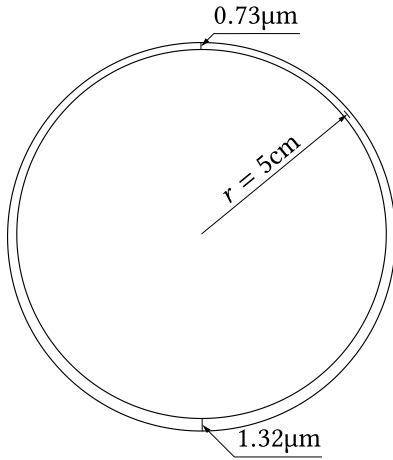
$$\frac{\partial^2 u'_\theta}{\partial \phi^2}, \frac{\partial \eta'}{\partial \theta} \frac{\partial u'_\theta}{\partial \theta}, \dots$$

The complete terms are provided in Eq. (D.37). For readability, we drop the primes from this point onward. Further, within the scope of this work, we assume that the soap molecules are not diffusive ( $D_s = 0$ ) and that viscosity can be neglected. Readers interested in viscous effects may refer to Section 3.7.1. In spherical coordinates, the total derivative of  $\vec{u}$  can be written as

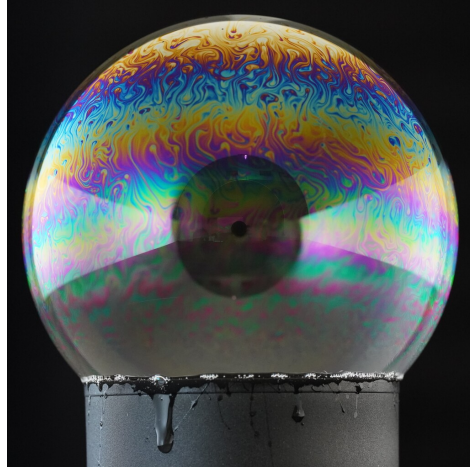
$$\begin{aligned} \frac{D\vec{u}}{Dt} &= \left( \frac{\partial u_\theta}{\partial t} + u_\theta \frac{\partial u_\theta}{\partial \theta} + \frac{u_\phi}{\sin \theta} \frac{\partial u_\theta}{\partial \phi} - \frac{u_\phi^2}{\tan \theta} \right) \vec{e}_\theta \\ &+ \left( \frac{\partial u_\phi}{\partial t} + u_\theta \frac{\partial u_\phi}{\partial \theta} + \frac{u_\phi}{\sin \theta} \frac{\partial u_\phi}{\partial \phi} + \frac{u_\theta u_\phi}{\tan \theta} \right) \vec{e}_\phi \end{aligned} \quad (3.12)$$

and its divergence as

$$\nabla \cdot \vec{u} = \frac{1}{\sin \theta} \left[ \frac{\partial u_\phi}{\partial \phi} + \frac{\partial}{\partial \theta} (u_\theta \sin \theta) \right]. \quad (3.13)$$



(a) Typical dimensions



(b) Soap bubble photograph

Figure 3.4: Under the influence of gravity and with surface tension as opposing force, bubbles assume an equilibrium state where the film thickness gradually increases from top to bottom. This is reflected by the horizontal fringe pattern observed on real-world bubbles.

The derivatives of a scalar field  $\Phi$  (which could either be the thickness  $\eta$  or the soap concentration  $\Gamma$ ), are

$$\nabla\Phi = \left( \frac{\partial\Phi}{\partial\theta}, \frac{1}{\sin\theta} \frac{\partial\Phi}{\partial\phi} \right)^\top, \quad (3.14)$$

$$\frac{D\Phi}{Dt} = \frac{\partial\Phi}{\partial t} + u_\theta \frac{\partial\Phi}{\partial\theta} + \frac{u_\phi}{\sin\theta} \frac{\partial\Phi}{\partial\phi}, \quad (3.15)$$

$$\nabla^2\Phi = \frac{1}{\sin\theta} \left[ \frac{\partial}{\partial\theta} \left( \sin\theta \frac{\partial\Phi}{\partial\theta} \right) + \frac{\partial}{\partial\phi} \left( \frac{1}{\sin\theta} \frac{\partial\Phi}{\partial\phi} \right) \right]. \quad (3.16)$$

There are mainly two contributions for the evolution of soap film thickness  $\eta$  and surfactant concentration  $\Gamma$ : they are passively advected by the flow field [139], but also affected by inflow or outflow as expressed by the divergence terms in Eqs. (3.10b) and (3.10c). Unlike the full 3D incompressible flow (Eq. (3.1b)), the 2D flow within a thin film behaves like a compressible, elastic medium.

### 3.3.3 Surface and body forces

The most important forces governing the motion of a soap film within its manifold are surface tension, gravity and air friction. The interaction be-

tween gravity and surface tension will cause thinner films to float upwards and thicker films to drop downwards, so that a soap bubble (or film) at its equilibrium state always assumes a wedge shape (Fig. 3.4). Let  $g$  be the gravitational acceleration scaled by  $U^2/R$ . If we assume the north pole of the bubble to be pointing upwards, then the gravity vector  $\vec{g}$  in the spherical coordinate system  $(\vec{e}_\theta, \vec{e}_\phi)$  is  $\vec{g} = (g \sin \theta, 0)^\top$ .

As a soap bubble is very thin, the film is easily set into motion by tangential air flow. If the surrounding air is still, it damps the flow motion. For simplicity, we assume a linear Stokes drag  $\vec{f}_{\text{air}} = (Cr/\eta)(\vec{u}_{\text{air}} - \vec{u})$ , with  $Cr$  being the drag coefficient. Taking gravity and air friction into account, Eq. (3.10) becomes

$$\left[ \begin{array}{l} \frac{D\vec{u}}{Dt} = -\frac{M}{\eta} \nabla \Gamma + \frac{Cr}{\eta} (\vec{u}_{\text{air}} - \vec{u}) + \vec{g}, \\ \frac{D\Gamma}{Dt} = -\Gamma \nabla \cdot \vec{u}, \\ \frac{D\eta}{Dt} = -\eta \nabla \cdot \vec{u}. \end{array} \right. \quad \begin{array}{l} (3.17a) \\ (3.17b) \\ (3.17c) \end{array}$$

Interestingly, from Eq. (3.17a), we observe that surface forces as surface tension and air drag are divided by the film thickness, so that thinner films are more easily driven into motion, whereas body forces like gravity act throughout the volume of the body and thus do not depend on the thickness.

## 3.4 Method

In this section we develop novel spatial and temporal discretization schemes for the governing equations. In particular, via using a staggered spherical grid (Section 3.4.1), we develop an unconditionally stable advection scheme (Section 3.4.2) that can smoothly propagate flow across the poles, as well as a projection-like implicit solver for handling chemomechanical forces (Section 3.4.3).

### 3.4.1 Spatial discretization

We discretize the spherical domain with a staggered grid [139], where velocities and scalar quantities are stored at different locations (illustrated in Figs. 3.5 and 3.6). This allows the accurate evaluation of the concentration gradient  $\nabla \Gamma$  and the velocity divergence  $\nabla \cdot \vec{u}$  using central differences without the formation of checkerboard patterns [15, Ch. 2.4]. Also, a regular grid

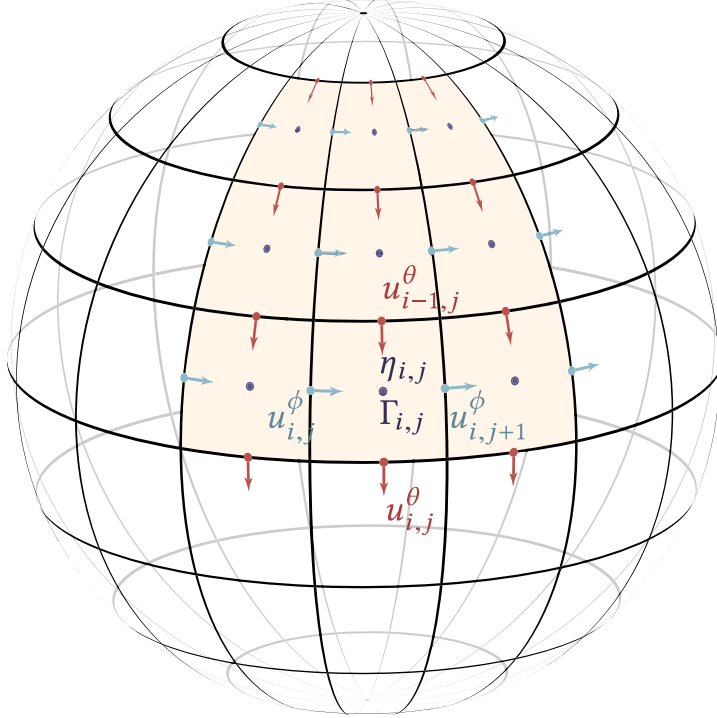


Figure 3.5: The staggered spherical grid. Film thickness  $\eta$  and soap concentration  $\Gamma$  are evaluated at the cell center, while the  $\theta$  and  $\phi$  components of the velocity vector  $\vec{u}$  are sampled at the midpoints of cell boundaries.

discretization makes it possible to build a symmetric positive definite linear system that can be solved using the conjugate gradient method.

The velocity vector is split in two components,  $u_\phi$  and  $u_\theta$ , which are located at the center of the cell boundaries, whereas the concentration  $\Gamma$  and the thickness  $\eta$  are sampled at the cell center. Assuming the staggered grid consists of  $N_\theta \times N_\phi$  cells, then the dimension of  $u_\phi, \Gamma$  and  $\eta$  is  $N_\theta \times N_\phi$ , and the dimension of  $u_\theta$  is  $(N_\theta - 1) \times N_\phi$ . Quantities that do not lie exactly on the respective grid points are bi-linearly interpolated between neighboring grid points (Fig. 3.7). Special care needs to be taken when sampling near the poles, as neighborhood relations reach across the pole. At this point, both  $\vec{e}_\theta$  and  $\vec{e}_\phi$  experience a sign change, so velocity samples drawn from across the pole have to be negated.

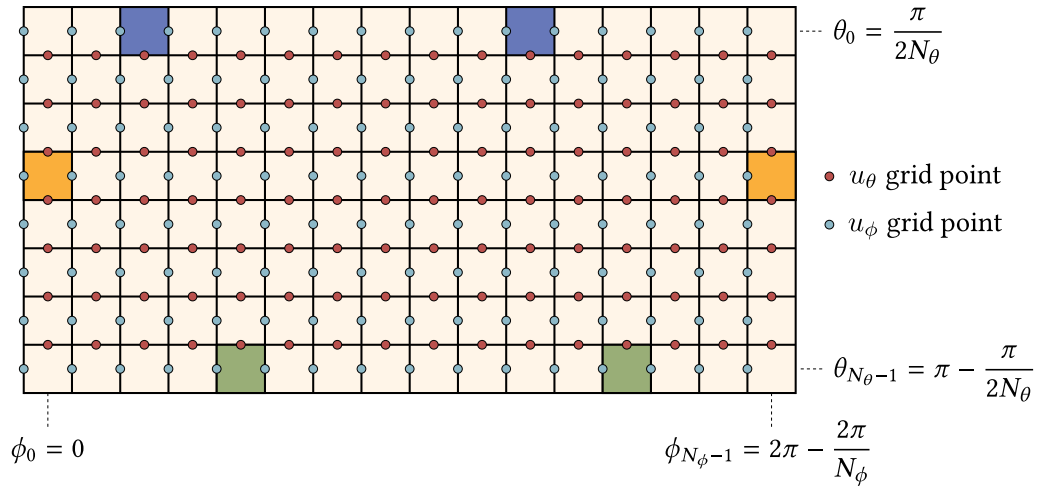


Figure 3.6: The staggered spherical grid unrolled in  $\theta$  and  $\phi$  direction, with the north pole at  $\theta = 0$  and the south pole at  $\theta = \pi$ . Cells with the same color indicate direct neighborhood. Specifically, in  $\phi$ -direction, periodic boundary conditions are employed, while in  $\theta$ -direction,  $\phi$  is shifted by  $180^\circ$  when crossing the pole. The velocity vector is not stored explicitly at the poles and instead we sample the vectors close to the pole bi-linearly from neighboring cells.

### 3.4.2 Advection

Taking an operator splitting approach, we first solve the material derivative ( $D/Dt$ ) parts of  $\vec{u}$ ,  $\eta$ , and  $\Gamma$  in Eq. (3.17) along the velocity field through advection; afterwards, we treat the remaining force terms in a separate step (Section 3.4.3).

On the spherical domain, the pure advection of a time-dependent scalar field  $\Phi(\vec{x}, t)$ ,  $\vec{x} = (\theta, \phi)^\top$ , along the velocity field  $\vec{u}(\vec{x}, t) = (u_\theta(\vec{x}, t), u_\phi(\vec{x}, t))^\top$  can be written as the initial value problem [95]

$$\begin{aligned} \frac{D\Phi}{Dt} &= \frac{\partial\Phi}{\partial t} + u_\theta \frac{\partial\Phi}{\partial\theta} + \frac{u_\phi}{\sin\theta} \frac{\partial\Phi}{\partial\phi} = 0, \\ \Phi(\vec{x}, 0) &= \Phi^0(\vec{x}). \end{aligned} \quad (3.18)$$

We seek to evaluate the advected quantity at a grid point  $\vec{x}_{ij} = (\theta_i, \phi_j)^\top$ . In keeping with standard practice in fluid simulation, we introduce a virtual particle that passes the grid point at time  $t$ , and trace it backward in time. This results in the time-dependent trajectory  $X^{(\vec{x}_{ij}, t)}(\tau)$  for the seed point  $(\vec{x}_{ij}, t)$  and time parameter  $\tau < t$ . Substituting this trajectory into Eq. (3.18)

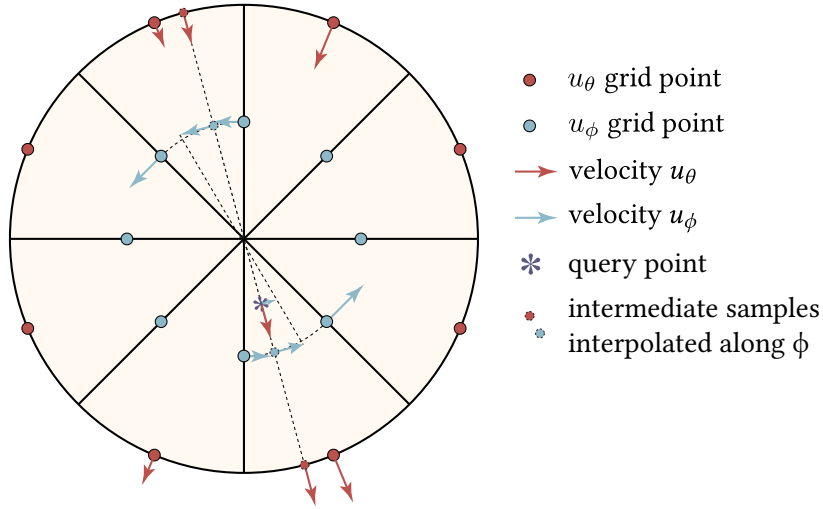


Figure 3.7: Sampling velocities bi-linearly at the pole. As samples are interpolated across the pole, it is important to take into account the sign flip of  $\vec{u}$  caused by the parameterization singularity.

yields

$$\begin{aligned}
0 &= \frac{D}{D\tau} \Phi(X(\bar{x}_{ij}, t)(\tau), \tau) \Big|_{\tau=t} \\
&\approx \frac{1}{\Delta t} (\Phi(X(\bar{x}_{ij}, t)(t)) - \Phi(X(\bar{x}_{ij}, t)(t - \Delta t))),
\end{aligned} \tag{3.19}$$

where the finite difference corresponds to a discretization of the time domain around  $t$  with step size  $\Delta t$ . A particle that undergoes pure advection experiences  $\Phi$  as being constant. We exploit this property to approximate the value for  $\Phi(X(\bar{x}_{ij}, t)(t))$  using a sample taken a step of  $\Delta t$  backward through the flow field. A numerical integration step like Euler or Runge-Kutta can be used to obtain  $\Phi(X(\bar{x}_{ij}, t)(t - \Delta t))$ .

Advecting vectors in spherical coordinates is much more challenging. As  $\partial \bar{e}_\theta / \partial \phi$  and  $\partial \bar{e}_\phi / \partial \theta$  are not equal to zero (Appendix A) as they would be on a Cartesian grid, Eq. (3.12) contains the additional terms  $-u_\phi^2 / \tan \theta$  and  $u_\theta u_\phi / \tan \theta$  that are not present in Eq. (3.18). Yang et al. [139] advect vectors in a scalar-like manner with  $(u_\theta, u_\phi / \sin \theta)^\top$ , and treat the two additional terms as body forces in an additional backward Euler integration step. Their method does not work well in practice when additional force terms are present. Instead, we are able to perform unconditionally stable vector advection in a single step. We note that at the equator  $\theta = \pi/2$ , where  $\tan^{-1} \theta = 0$ , these two extra terms vanish. There, the advection of a vector field falls back to the known case of advecting a scalar field. We exploit this insight in order to

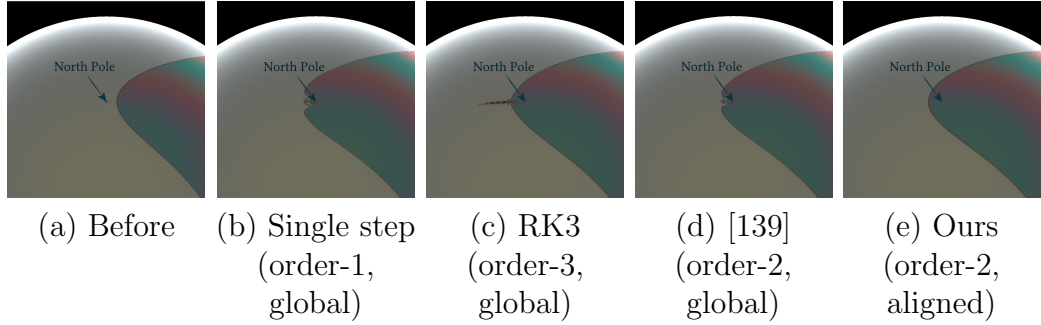


Figure 3.8: A scalar field with a sharp transition is advected across the north pole. Shown are film thickness maps before (a) and after (b–e) passing the pole, advected over 4 time steps using different methods. Using a velocity-aligned coordinate frame introduced in Section 3.4.2, our method is the only one to solve this problem without visible artifacts.

obtain this desirable property anywhere on the sphere. By constructing a local coordinate system at each grid point that aligns with the velocity, we can treat the quantities there as if they were on the equator.

For each grid point  $\vec{x}_{ij} = X^{(\vec{x}_{ij}, t)}(t)$ , we draw a great circle on the sphere that passes through this point and is tangent to the velocity  $\vec{u}$  at this point (see Fig. 3.9). We denote the unit vector in  $\vec{u}$ -direction to be  $\hat{u}$ , and the unit vector pointing from the sphere center  $O$  to  $\vec{x}_{ij}$  to be  $\hat{w}$ , and the binormal unit vector to be  $\hat{v} = \hat{w} \times \hat{u}$ . Then the great circle can be parameterized by

$$C(s) = \sin(s)\hat{u} + \cos(s)\hat{w}, \quad s \in \mathbb{R}; \quad (3.20)$$

*i.e.*, changing the arc parameter  $s$  translates the current grid point  $\vec{x}_{ij} = C(0) = \hat{w}$  back or forward in time with unit velocity. Following  $\vec{u}$  backward for a time step  $\Delta t$  results in a change in the arc parameter of  $-\Delta s = -\|\vec{u}\|\Delta t$ , taking us to the point

$$C(-\Delta s) = \sin(-\Delta s)\hat{u} + \cos(-\Delta s)\hat{w}. \quad (3.21)$$

This results in the following single-step advection scheme (Fig. 3.9):

1. Evaluate the velocity  $\vec{u}$  and establish the great circle  $C$  in its direction.
2. Perform an interpolated lookup of the velocity  $\vec{u}'$  at  $C(-\Delta s)$  using the technique described in Section 3.4.1.
3. Decompose  $\vec{u}'$  into tangent and binormal components  $u'$  and  $v'$  with respect to the great circle  $C$  at this point.

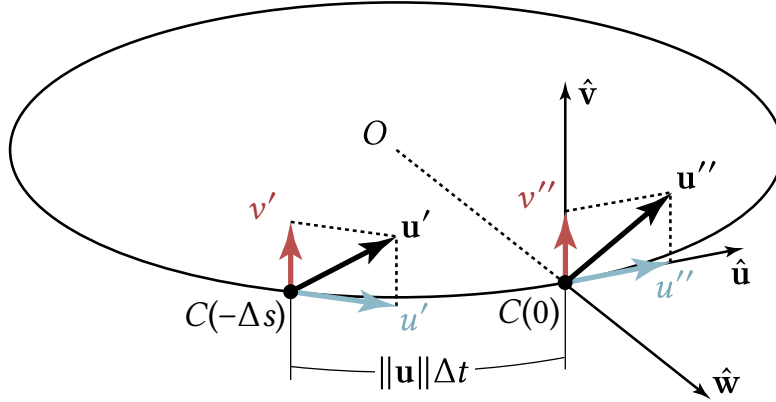


Figure 3.9: A single advection step for the velocity field on the sphere, executed in a local, flow-aligned coordinate frame (great circle  $C$ ). A detailed description of the procedure is provided in Section 3.4.2.

4. Move components back along the circle to  $\vec{x}_{ij} = C(0)$  with  $v'' = v'$ ,  $u'' = u'$ .
5. Project the advected quantity  $\vec{u}'' = v''\hat{v} + u''\hat{u}$  back to global spherical coordinate system to obtain  $u_\theta^*$  and  $u_\phi^*$ .

The main distinction of this approach to existing work is in the choice of coordinate frame. Rather than operating in the *global* spherical coordinate system, it locally creates an orthonormal coordinate frame that is defined by the velocity vector and therefore *data-aligned*. Since the method only interpolates values from the last step, it is unconditionally stable.

When higher accuracy is desired, the same principle can also be used to implement higher-order schemes involving multi-step updates. As an example, we lay out the construction of a 2<sup>nd</sup>-order “half-step” scheme (Fig. B.1) in Appendix B, which was used to generate the results shown throughout this chapter.

By design, our advection scheme does not produce artifacts when advecting quantities (scalars or vectors) around the poles, see Fig. 3.8. Yang et al. [139] adapts the advection scheme by Hill and Henderson [51] to staggered grids, where boundary conditions are introduced at both poles to remove *singularities*. However, according to Hill and Henderson [51], their method is not free of *artifacts*: small disturbances will appear near the pole due to variation of grid spacing (the  $1/\sin\theta$  term becomes prohibitively large near the pole). By constructing a local frame in our advection scheme, the  $1/\sin\theta$  term always takes the value 1, so the variation in grid spacing does not affect the advection. Moreover, the so-called geometry term [139, 51] that is caused

by coordinate orientation changes in curvilinear coordinate systems (see Appendix A) is in our case implicitly handled when transforming from global to local coordinates, and does not need to be solved separately. By performing our global-to-local coordinate transformation everywhere on the sphere, we show that all the discretization points on the sphere can be treated equally and there is no need for any *special pole treatment*. We expect this method to perform equally well as on a Cartesian grid.

### Preserving details

The interpolated look-up in our advection scheme causes numerical diffusion known from all semi-Lagrangian methods. This is acceptable for  $\vec{u}$  and  $\Gamma$ , since both PDEs include diffusive terms (see Eq. (3.10)). However, the transport equation for  $\eta$  is non-diffusive. Therefore, it is important to prevent high-frequency details in the film thickness from blurring out over time.

To achieve this goal, we make use of BiMocq<sup>2</sup> [96] and extend the method to spherical coordinates. Essentially, BiMocq<sup>2</sup> keeps a backward mapping

$$\mathcal{X}(\vec{x}(T)) : \vec{x}(T) \rightarrow \vec{x}(t_0) \quad (3.22)$$

which maps a spatial point  $\vec{x}(T)$  back to its position at the initial time  $t_0$ , as well as a forward mapping

$$\mathcal{Y}(\vec{x}(t_0)) : \vec{x}(t_0) \rightarrow \vec{x}(T) \quad (3.23)$$

which maps a spatial point at the initial position  $\vec{x}(t_0)$  to its current position at  $t = T$ . Instead of repeatedly blurring the features from the last time step, we acquire the initial state directly from the backward mapping, which corresponds to the pure advection part  $D/Dt$ . The additional changes ( $-\eta \nabla \cdot \vec{u}$  in our case) are accumulated along the forward mapping and added to the acquired value from backward mapping. At each simulation step, both mappings are updated via the advection method in Section 3.4.2, and the coordinates are interpolated using spherical linear interpolation. When the distortion between forward and backward mapping becomes too large, both mappings are re-initialized. This, however, introduces a small amount of numerical diffusion. We found that re-initializing both mappings when the distortion is larger than  $\pi/128$  provides a good trade-off between sharpness and noise. For other implementation details, such as error correction, we refer the reader to the original paper [96].

### 3.4.3 Concentration splitting

After solving the advection part  $D/Dt = 0$ , we now deal with force and divergence terms in the right hand sides of Eq. (3.17). Soap film exhibits elastic

properties similar to a mass-spring system. Solving such systems using an explicit time integrator would require prohibitively small step sizes to achieve a stable simulation. Instead, we construct a projection-like implicit system for  $\Gamma$  and  $\vec{u}$ . To keep the system linear, we still solve for  $\eta$  explicitly.

We temporally discretize the continuous equations into

$$\left[ \begin{array}{l} \frac{\vec{u} - \vec{u}^*}{\Delta t} = -\frac{M}{\eta^*} \nabla \Gamma + \frac{Cr}{\eta^*} (\vec{u}_{\text{air}} - \vec{u}) + \vec{g}, \\ \frac{\Gamma - \Gamma^*}{\Delta t} = -\Gamma^* \nabla \cdot \vec{u}, \\ \frac{\eta - \eta^*}{\Delta t} = -\eta^* \nabla \cdot \vec{u}, \end{array} \right. \quad (3.24a)$$

$$\left[ \begin{array}{l} \frac{\Gamma - \Gamma^*}{\Delta t} = -\Gamma^* \nabla \cdot \vec{u}, \\ \frac{\eta - \eta^*}{\Delta t} = -\eta^* \nabla \cdot \vec{u}, \end{array} \right. \quad (3.24b)$$

$$\left[ \begin{array}{l} \frac{\eta - \eta^*}{\Delta t} = -\eta^* \nabla \cdot \vec{u}, \end{array} \right. \quad (3.24c)$$

where  $\Gamma^*$ ,  $\eta^*$ , and  $\vec{u}^*$  denote the respective quantities after applying the advection step. First, we solve for  $\Gamma$  by rewriting Eq. (3.24a) and applying divergence to both sides of the result,

$$\nabla \cdot \vec{u} = \nabla \cdot \frac{\eta^* \vec{u}^* + Cr \Delta t \vec{u}_{\text{air}} + \Delta t \eta^* \vec{g}}{\eta^* + Cr \Delta t} - M \Delta t \nabla \cdot \frac{\nabla \Gamma}{\eta^* + Cr \Delta t}. \quad (3.25)$$

Afterwards, we combine Eqs. (3.24b) and (3.25) and eliminate  $\nabla \cdot \vec{u}$ ,

$$\begin{aligned} & \frac{\Gamma}{\Gamma^* \Delta t} - M \Delta t \nabla \cdot \frac{\nabla \Gamma}{\eta^* + Cr \Delta t} \\ &= \frac{1}{\Delta t} - \nabla \cdot \frac{\eta^* \vec{u}^* + Cr \Delta t \vec{u}_{\text{air}} + \Delta t \eta^* \vec{g}}{\eta^* + Cr \Delta t}. \end{aligned} \quad (3.26)$$

Finally, we express this linear system as a sparse matrix (Appendix C), solve it for  $\Gamma$  using a preconditioned conjugate gradient method [83], and update  $\vec{u}^{n+1}$  and  $\eta^{n+1}$  using Eqs. (3.24a) and (3.24c). Note that this system is strictly symmetric positive definite unless  $\Gamma^*$  approaches infinity, in which case we end up with a Poisson equation that is closely related to pressure projection in nearly incompressible mixed finite elements.

Our implicit treatment of the concentration based on its evolution Eq. (3.24b) allows us to take significantly larger time steps compared to what could be permitted when treating the forces explicitly. Our method also avoids solving an extremely stiff indefinite system as in standard Newton-based elasticity solvers [38].

### 3.4.4 Implementation and runtime performance

We implemented our method using CUDA and AmgX [83], and executed it on an NVIDIA GeForce GTX 1080 graphics card. A typical resolution for

our simulation grid is  $1024 \times 2048$  with a step size of 0.002 s. At this setting, a single time step typically takes 16–17 conjugate gradient iterations and 1.1 s to execute. The bulk of the compute time is spent on divergence/force calculation and advection with 75% and 25%, respectively. The source code is provided in <https://github.com/RiverInTheSky/SoapBubble>.

## 3.5 Soap bubble rendering

The iridescent effects produced by thin films are wave-optical effects that arise from constructive and destructive interference of light waves. To compute the light power that is reflected or transmitted when interacting with a thin film, we need to consider the corresponding complex amplitudes of the electromagnetic wave. This section describes a real-time renderer for spherical soap bubbles that is specifically targeted at the correct handling of polarization and spectral sampling.

### 3.5.1 Thin film model

We follow the modeling of Belcour and Barla [10] for the reflection and transmission through a single thin film layer. In our case, the light interacts multiple times with the soap bubble surface on a given light path, so their analytical solution to the spectral integration does not directly apply here. After each reflection, we would have to retract to an RGB representation of the light, introducing an error that increases with each interaction with the soap bubble. Therefore, we numerically integrate the compounded reflectance and transmittance for each light path over the wavelengths  $\lambda$ , which we sample at 5 nm intervals, and compute the fractional light power that is carried by each light path for each wavelength.

**Material model** The surface of the soap bubble is modeled locally as a thin film with parallel interfaces, sandwiched between two layers of air with refractive index  $n_a = 1$ . The refractive index of the soap water in between is  $n_s = 1.33$ . For a single interaction of the light with the soap bubble, the film thickness  $2\eta$  is assumed to be constant. For a given light direction  $\vec{i}$  and surface normal  $\vec{n}$ , we define the angle of incidence  $\theta_a$  in air via  $\cos \theta_a = \vec{i} \cdot \vec{n}$ . Upon refraction into the soap film, the angle at which the light travels is found via Snell’s law:  $n_a \sin \theta_a = n_s \sin \theta_s$ . Since the film interfaces are assumed to be parallel, the angle at which the light is refracted out of the film at both interfaces equals  $\theta_a$ , and the direction of the light transmitted through the film is uninterrupted from air to air. We assume that the light

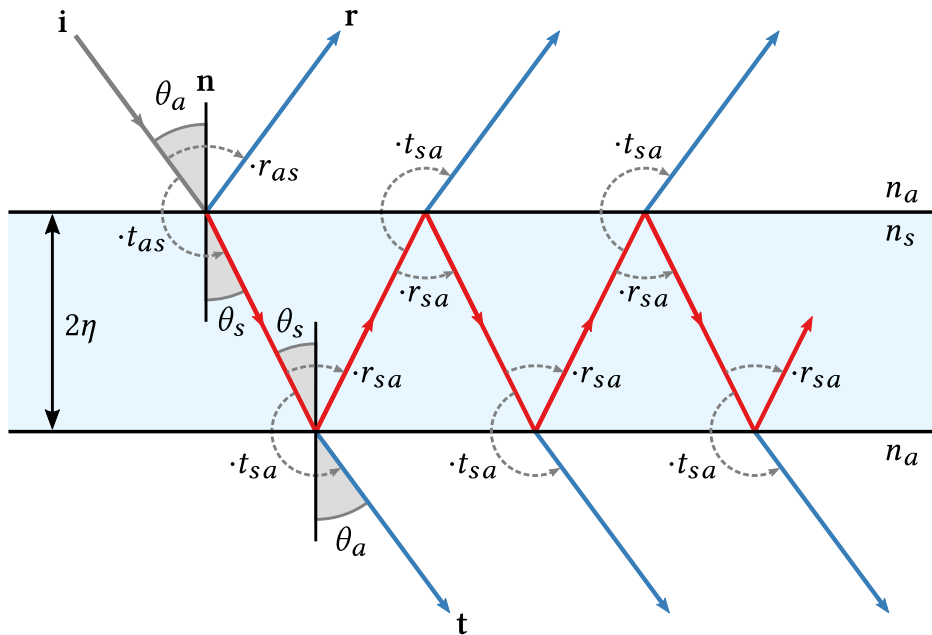


Figure 3.10: Light paths in soap film. Light is refracted into the film, and attenuated at each film interaction. The emitted light paths at the top and bottom of the film produce interference, respectively.

enters and leaves the film at the same location on a macroscopic scale, since the film thickness is much smaller than the lateral extent of the soap bubble.

**Thin-film reflectance** The polarization-dependent reflectance  $R$  and transmittance  $T$  are the ratios of outgoing to incoming light powers at an interface between two media. In order to compute these values for two media separated by a thin film, we consider the complex-valued electro-magnetic wave amplitudes. The complex-valued reflection coefficient  $r$  and transmission coefficient  $t$  describe the ratios of outgoing to incoming wave amplitudes. Since the power carried by a light wave is proportional to the square of the wave amplitude, we have  $R = |r|^2$  and  $T = |t|^2$ . In addition to the power ratio, they also encode a phase shift of the light wave, which leads to constructive and destructive interference when two light paths interfere and their reflection or transmission coefficients are added. The reflectance and transmittance produced by an interaction with the film is computed for each wavelength and polarization by taking all light paths inside the thin film (shown in Fig. 3.10) into account and accumulating their wave amplitudes. The light waves are affected by the reflection coefficients  $r_{as}$ ,  $r_{sa}$  and transmission coefficients  $t_{as}$ ,

$t_{sa}$ , defined by Fresnel's equations [14], where  $r_{as}$  and  $t_{as}$  act at the air-to-soap interface and  $r_{sa}$  and  $t_{sa}$  on the soap-to-air interface. The light waves of each path are also affected by a wavelength-dependent phase shift, induced by the difference in path length between successively emitted light rays at each film interface. This difference in path length is known as the optical path difference  $\mathcal{D} = 4\eta n_s \cos \theta_s$ , which introduces a phase shift  $\Delta\psi = 2\pi \frac{\mathcal{D}}{\lambda}$  of a light path with respect to its predecessor. The phase shifts with respect to the first light ray accumulate linearly, such that the  $k$ -th ray is phase-shifted by  $k\Delta\psi$ . Summing the contributions from the infinitely many emitted light rays at the top and bottom interface yields the reflectance  $R$ ,

$$\begin{aligned} R(\lambda) &= \left| r_{as} + \sum_{k=0}^{\infty} t_{as} r_{sa} (r_{sa}^2 e^{i\Delta\psi})^k e^{i\Delta\psi} t_{sa} \right|^2 \\ &= \left| r_{as} + \frac{t_{as} r_{sa} t_{sa} e^{i\Delta\psi}}{1 - r_{sa}^2 e^{i\Delta\psi}} \right|^2, \end{aligned} \quad (3.27)$$

and transmittance  $T$  of the thin-film

$$\begin{aligned} T(\lambda) &= \left| \sum_{k=0}^{\infty} t_{as} (r_{sa}^2 e^{i\Delta\psi})^k t_{sa} \right|^2 \\ &= \left| \frac{t_{as} t_{sa}}{1 - r_{sa}^2 e^{i\Delta\psi}} \right|^2. \end{aligned} \quad (3.28)$$

Since we are not dealing with total internal reflections,  $|r_{sa}| < 1$  holds and taking the limit of the geometric series yields a closed form solution for each wavelength.

### 3.5.2 Soap bubble ray tracing

The wave nature of light only needs to be taken into account when computing the reflectance and transmittance for a single interaction with the soap bubble. Since soap bubbles are inherently transparent, many light paths contribute to a given view ray. To compute the light transport along these paths, we multiply the reflectance and transmittance produced at each soap bubble interaction along the path. The light transport  $\mathcal{R}^{(n)}$  for the  $n$ -th order light path is defined as

$$\mathcal{R}^{(0)} = R^{(0)} \quad \text{and} \quad \mathcal{R}^{(k)} = T^{(0)} \prod_{i=1}^{k-1} R^{(i)} T^{(k)}, \quad (3.29)$$

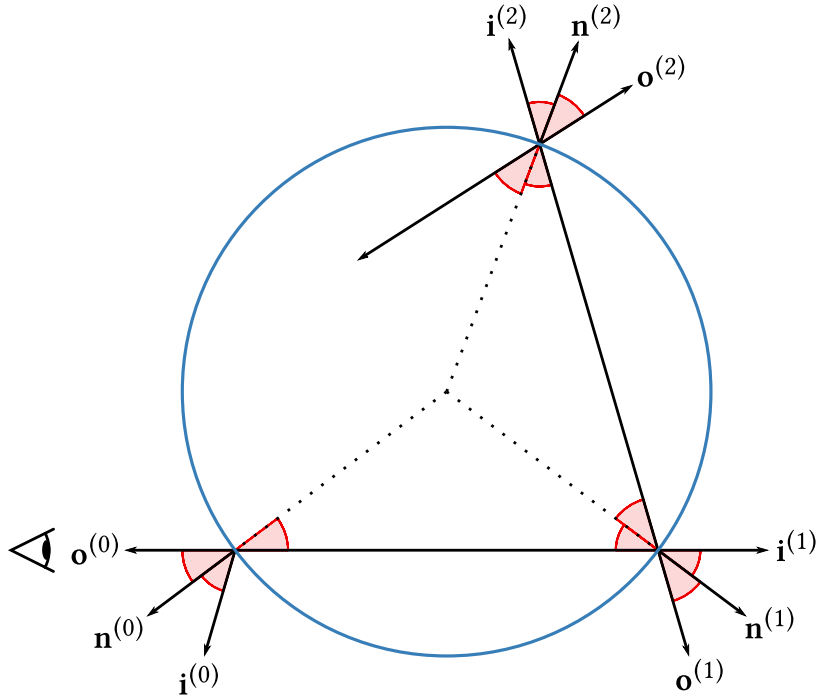


Figure 3.11: Light paths in a spherical soap bubble. All angles marked in red are equal.

for  $k \geq 1$ , where  $R^{(i)}$  and  $T^{(i)}$  are the iridescent reflectance and transmittance produced at the  $i$ -th interaction with the soap bubble along the path traced backwards from the observer. The reflectance  $R^{(i)}$  and transmittance  $T^{(i)}$  produced by different interactions along a path change only due to differences in film thickness. The angle of incidence is constant for all interactions along a light path (see Fig. 3.11) and the index of refraction is constant as well.

**Polarization** Due to the spherical geometry of the soap bubble, the incoming and outgoing light directions for all interactions lie in the same plane. This implies that the light polarization basis (the decomposition into s and p component) does not change between successive soap film interactions. Therefore, we are able to correctly handle polarization effects by first evaluating Eq. (3.29) for each polarization direction independently, and then averaging both frames.

**Tracing rays** For the computation of the light paths through the soap bubble, illustrated in Fig. 3.11, we exploit the assumption that the soap bubble is spherical. We evaluate the first  $N = 8$  light paths through the soap bubble. Since we assume distant illumination, we do not track the

world-space location of the film interactions, and only consider the relevant directions: the incoming light direction  $\vec{i}^{(i)}$  of the  $i$ -th order light path to sample the environment map, the surface normal  $\vec{n}^{(i)}$  to sample the film thickness  $2\eta$  at the  $i$ -th interaction, and the (virtual) viewing direction  $\vec{o}^{(i)}$ , which is used to compute the directions for the succeeding interaction with the soap film. Given these values for the  $i$ -th film interaction, the directions for the  $i + 1$ -th interaction are defined as

$$\begin{aligned}\vec{n}^{(i+1)} &= \vec{n}^{(i)} - 2\vec{n}^{(i)} \cdot \vec{o}^{(i)} \vec{o}^{(i)}, \\ \vec{i}^{(i+1)} &= -\vec{o}^{(i)}, \\ \vec{o}^{(i+1)} &= \vec{o}^{(i)} - 2\vec{o}^{(i)} \cdot \vec{n}^{(i+1)} \vec{n}^{(i+1)}.\end{aligned}\tag{3.30}$$

The surface normal  $\vec{n}^{(i+1)}$  is defined by a reflection of  $-\vec{n}^{(i)}$  at the outgoing light direction  $\vec{o}^{(i)}$ , and the new outgoing light direction  $\vec{o}^{(i+1)}$  is then the reflection of the incoming light direction  $\vec{i}^{(i+1)}$  at the surface normal  $\vec{n}^{(i+1)}$  (see Fig. 3.11).

**Spectral integration** To produce an sRGB color image, we have to integrate the response to the respective color-matching functions  $s_j$  for  $j \in \{R, G, B\}$  of the color space:

$$L_{o,j} = \int s_j(\lambda) \cdot \sum_{n=0}^{\infty} \mathcal{R}_n(\lambda) L_i^{(n)}(\lambda) d\lambda,\tag{3.31}$$

where  $L_{o,j}$  is the integrated response for the  $j$ -th color channel, and  $L_i^{(n)}$  is the incoming light of the  $n$ -th light path. Since we use an RGB environment map for illumination,  $L_i^{(n)}$  is not known. For each color channel  $j$ , we assume  $L_i^{(n)} = L_{i,j}^{(n)}$  to be constant. Under this assumption Eq. (3.31) simplifies to

$$L_{o,j} \approx \sum_{n=0}^N L_{i,j}^{(n)} \cdot \int s_j(\lambda) \mathcal{R}_n(\lambda) d\lambda.\tag{3.32}$$

## 3.6 Results

In the following, we perform a selection of synthetic experiments and discuss the influence of the most important parameters and variables. From various sources, we attempted to gather as realistic a set of parameters as possible. The numbers used for simulations throughout this section, as well as sources for the more exotic values, are listed in Tables 3.1 and 3.2.

Table 3.1: Typical values and ranges of dimensional parameters used in our simulation. For values associated with air and soap solution, such as density and viscosity, we take common literature values for air and water, respectively, under standard conditions.

Description	Symbol	Value / Range	Unit
Bubble radius <sup>a</sup>	$R$	0.02 to 0.1	m
Mean half thickness <sup>a</sup>	$\eta_0$	$4 \times 10^{-7}$ to $1 \times 10^{-6}$	m
Characteristic velocity	$U$	1	$\text{m s}^{-1}$
Mean soap concentration <sup>b</sup>	$\Gamma_0$	$1 \times 10^{-8}$ to $1 \times 10^{-6}$	$\text{mol m}^{-2}$
Surface tension of water-air interface	$\gamma_a$	$7.275 \times 10^{-2}$	$\text{N m}^{-1}$
Gas constant	$\bar{R}$	8.3144598	$\text{J mol}^{-1} \text{K}^{-1}$
Room Temperature	$T$	298.15	K
Water mass density	$\rho$	997	$\text{kg m}^{-3}$
Water dynamic viscosity	$\mu$	$8.9 \times 10^{-4}$	Pas
Air density	$\rho_a$	1.184	$\text{kg m}^{-3}$
Air kinematic viscosity	$\nu_a$	$1.562 \times 10^{-5}$	$\text{m}^2 \text{s}^{-1}$
Gravitational acceleration	$G$	9.8	$\text{m s}^{-2}$
Surfactant diffusivity <sup>c</sup>	$D_s$	(0)	$\text{m}^2 \text{s}^{-1}$

<sup>a</sup>Empirical values.

<sup>b</sup>Taken from Couder et al.'s work [22, Figure 1(a)] in the low concentration range.

<sup>c</sup>We assume advection to be the dominant transport mechanism.

Table 3.2: Typical values of dimensionless parameters.

Description	Symbol	Definition	Value
Expansion parameter	$\epsilon$	$\frac{\eta_0}{R}$	$1 \times 10^{-5}$
Marangoni number	$M$	$\frac{\Gamma_0 \bar{R} T}{\rho \eta_0 U^2}$	0.83
Reynolds number	$Re$	$\frac{UR\rho}{\mu}$	$5.6 \times 10^4$
Drag coefficient	$Cr$	$\frac{\rho_a \sqrt{\nu_a \bar{R}}}{\rho \eta_0 \sqrt{U}}$	2.1
Scaled gravitational acceleration	$g$	$\frac{GR}{U^2}$	0.49



Figure 3.12: Influence of soap concentration  $\Gamma_0$  and bubble radius  $R$  on the thickness gradient in equilibrium state. The ratio of both parameters,  $\Gamma_0/R$ , is kept constant for both simulations, causing a similar appearance.

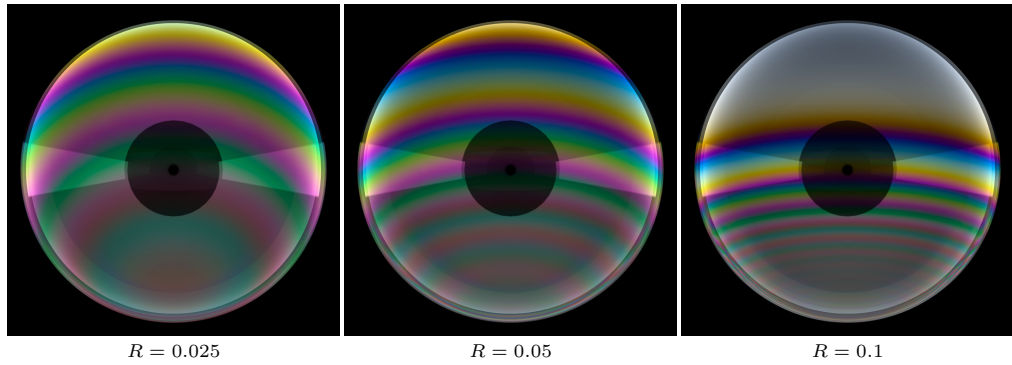


Figure 3.13: Equilibrium state as a function of  $R$ , for a film initialized with soap concentration  $\Gamma_0 = 6.67 \times 10^{-8}$  and thickness  $\eta_0 = 4 \times 10^{-7}$  and relaxed under standard gravity. For larger bubbles, the gravity drag causes a stronger displacement of material from top to bottom.

### 3.6.1 Mean surfactant concentration and bubble radius

According to the momentum equation (3.17a), a soap film under gravity but without other sources of excitation has its equilibrium state at

$$-\frac{M}{\eta} \frac{\partial \Gamma}{\partial \theta} + g \sin \theta = 0. \quad (3.33)$$

The other two Eqs. (3.17b) and (3.17c) can be rewritten as

$$\frac{D(\Gamma/\eta)}{Dt} = 0, \quad (3.34)$$

*i.e.*,  $\Gamma/\eta$  remains constant. If the simulation is started with uniform surfactant concentration and thickness, we can non-dimensionalize the variables so that

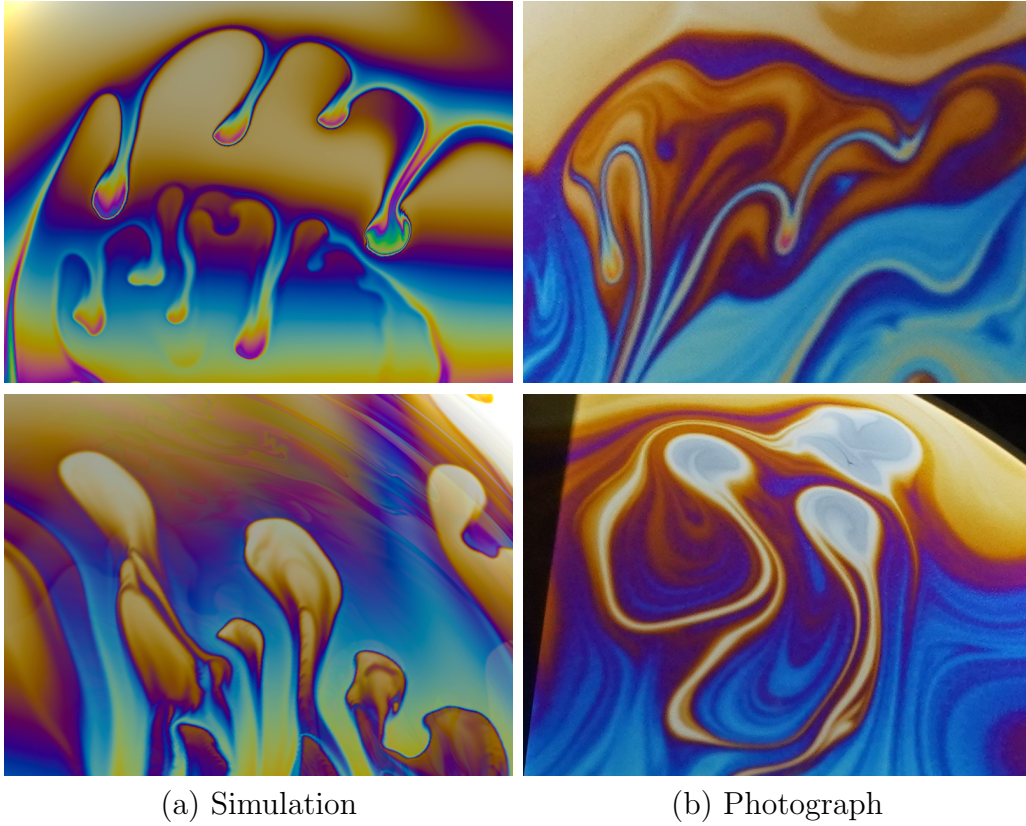


Figure 3.14: Under the influence of gravity, thicker (heavier) regions form downward-moving tears; thinner (lighter) regions rise from the bottom. These effects can be observed both in simulation (a) and experiment (b).

$\Gamma(t=0) = \eta(t=0) = 1$ . Combining the above two equations, this yields

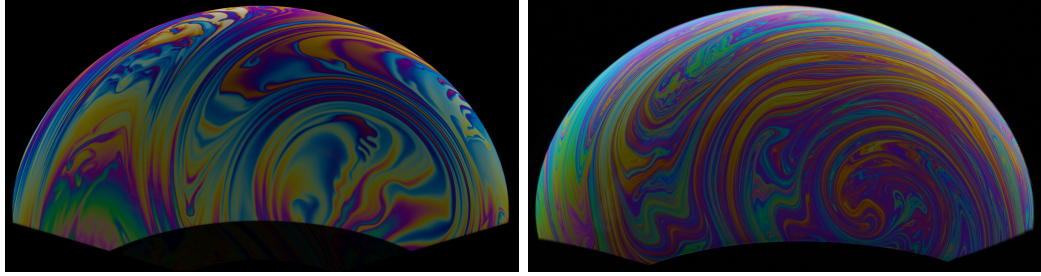
$$-\frac{M}{\eta} \frac{\partial \eta}{\partial \theta} + g \sin \theta = 0, \quad (3.35)$$

the solution of which is

$$\eta = \frac{\pi}{\int_0^\pi e^{-\frac{g \cos \theta}{M}} d\theta} e^{-\frac{g \cos \theta}{M}}. \quad (3.36)$$

From this, we can draw at least three conclusions:

- Soap films under the influence of gravity are thinner at the top and thicker at the bottom, leading to colorful bands on soap bubbles (Fig. 3.12). As noted in Fig. 3.3, the film color is also influenced by the viewing angle. On a bubble, the bands are bent downwards; on a flat film they appear horizontal.



(a) Simulation

(b) Photograph

Figure 3.15: Inflating a soap bubble with a straw generates a rotating “ball of air” trapped inside the bubble. The resulting velocity gradient leads to a shear motion and the formation of thin stripes.

- A constant ratio  $g/M$  will lead to the same equilibrium state (albeit through a different dynamic process). From the definitions of  $M$  and  $g$  (Table 3.2), this is equivalent to keeping  $R/\Gamma_0$  constant.
- The larger  $R/\Gamma_0$ , the thinner the film is at the top, and thicker at the bottom.

This expected behavior is confirmed in experiment and simulation (Figs. 3.12 and 3.13).

### 3.6.2 Gravity and buoyancy

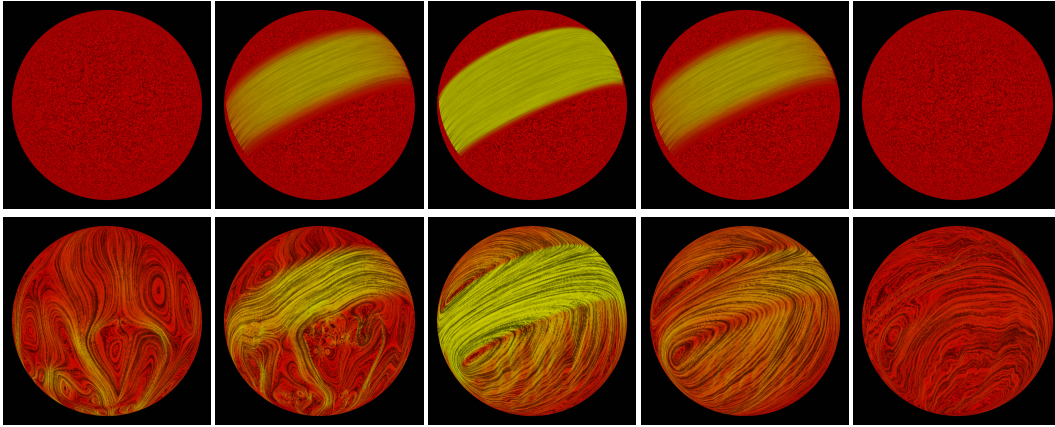
The momentum equation of a soap bubble

$$\frac{D\vec{u}}{Dt} = -\frac{M}{\eta}\nabla\Gamma + \frac{Cr}{\eta}(\vec{u}_{\text{air}} - \vec{u}) + \vec{g} \quad (3.37)$$

has great resemblance with the compressible Navier-Stokes equation

$$\frac{D\vec{u}}{Dt} = -\frac{1}{\rho}\nabla p + \frac{\mu}{\rho}\nabla^2\vec{u} + \frac{\mu}{3\rho}\nabla(\nabla\cdot\vec{u}) + \vec{g}, \quad (3.38)$$

where the surfactant concentration  $\Gamma$  takes the role of pressure  $p$  and the variable thickness  $\eta$  substitutes the variable density  $\rho$ . In fact, just as smoke with smaller density flows upwards in the air, thinner soap film regions also tend to flow upwards. This is confirmed by our observation. As thinner regions on a soap bubble flow upwards (and thicker regions downwards), they form drop-shaped “islands”, and leave “rivers” behind (Fig. 3.14).



(a)  $t = 0.52\text{ s}$  (b)  $t = 1.00\text{ s}$  (c)  $t = 2.04\text{ s}$  (d)  $t = 3.08\text{ s}$  (e)  $t = 3.56\text{ s}$

Figure 3.16: False-color visualization of a time-varying airflow (top) and the resulting velocity field (bottom) on a soap bubble using line integral convolution [17]. From left to right, the correlation of the lines shows the direction of the respective vector field, while the magnitude is encoded in the color. (a) After initialization with a noise texture, the fluid sags down under the influence of gravity. (b)–(d) Over a corridor on the surface, air gradually starts flowing and slows down again. The soap fluid follows the excitation. (e) After the air has stopped flowing, the bubble remains in a rotating motion.

### 3.6.3 Air friction

Soap films are highly susceptible to air flow, and assume beautiful patterns in windy environments. When a bubble is blown, a rapidly rotating wind field is produced inside and induces a shear motion on the soap film. Advection along the air flow results in thin stripes that remain stable even after the external influence has stopped (Fig. 3.15). See Fig. 3.16 for a false-color visualization of the external air flow and the resulting velocity field in multiple time steps of an experiment.

### 3.6.4 Evaporation

Due to evaporation, a soap bubble exposed to air becomes thinner and thinner and eventually breaks down. Since evaporation mostly depends on the exposed surface (which is constant), we model this effect by subtracting a small constant amount of  $\eta$  at each simulation step. Once a point on the surface reaches thickness zero, the simulation is terminated. Our model in its current form does not support the simulation of bursting bubbles. Fig. 3.17

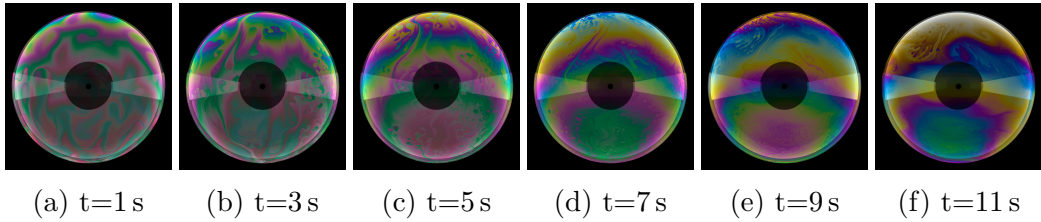


Figure 3.17: The bubble was initialized with a Perlin noise texture and excited by curl-noise air flow. As water evaporates and the film becomes thinner, the colorful bands move gradually downwards and the top of the bubble fades to gray.

shows a soap bubble over its whole lifetime. Starting from a random thickness distribution, thicker regions are moving downwards and horizontal color bands. Shortly before bursting, the top of the bubble becomes very thin and exhibits a gray appearance.

### 3.6.5 Real-world experiments

To capture stills and videos of real-world bubbles under laboratory conditions, we constructed simple studio environments consisting of 1200mm  $\times$  1200mm LED panels, black theater curtain and a Sony ILCE-7RM3 system camera with a ZEISS Batis 135 mm  $f/2.8$  lens. We use Pustefix brand soap solution for all experiments.

## 3.7 Discussion and Future Work

We have been able to show that our model and solver, which is fast and stable, can recreate the most prominent effects found on spherical soap bubbles in the real world. An obvious next step will be to look into more general cases, like complex film shapes or groups of bubbles. Although we focus on spherical geometry in this chapter, the ideas underlying our scheme are not limited to spherical domains. Ida and Miksis’s model [55] is valid for general manifolds; following their derivation, one arrives exactly at Eq. (3.10), with the definition of the differential operators adjusted to the corresponding curvilinear coordinate frame. Furthermore, the idea of our advection scheme is independent of the underlying manifold shape, as long as a proper local coordinate frame is constructed. Finally, the special force and divergence terms treatment in Eq. (3.26) holds for arbitrary shapes and can be expressed as a sparse matrix, as long as the neighborhood of each point is well-defined.



Figure 3.18: A vertical soap film with marginal regeneration. Picture taken from Nierstrasz and Frens’s work [86].

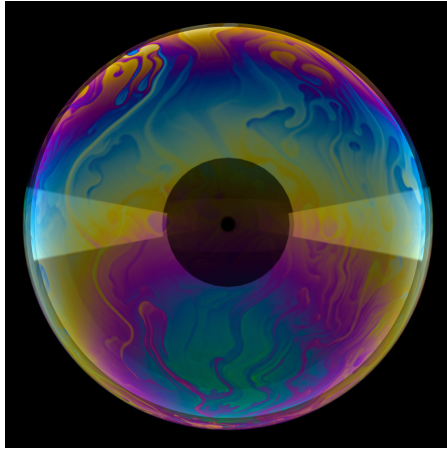
However, nice-to-have properties (such as the matrix being symmetric positive definite) might be lost in other types of meshes or grids. Consequently, our scheme should not be difficult to generalize to bubbles that are diffeomorphic to a sphere. Groups of bubbles with Plateau borders, as well as bounded films, are not manifolds and hence have to be left to future consideration. The treatment of film boundaries deserves particular attention also because a complicated mechanism called *marginal regeneration* [58] causes the film to become even thinner at the boundaries, producing regions that flow upwards erratically (see Fig. 3.18).

### 3.7.1 Viscous film

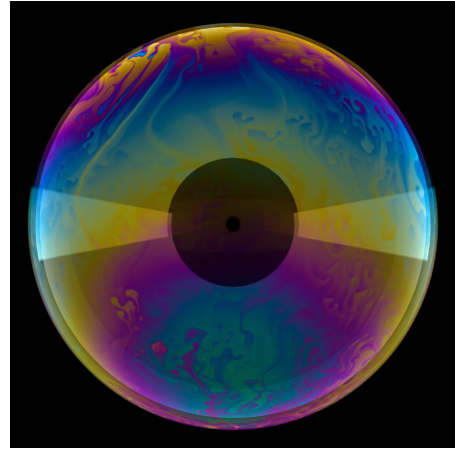
Soap films with larger viscosity tend to be more stable and last longer, which can be achieved by adding glycerin to home-made soap solution. Some commercial soap solution also includes additional formula to make it more viscous. The soap solution we used in experiments, for example, has a dynamic viscosity of  $1.2 \times 10^{-1}$  Pa s, which is about 100 times greater than that of water and thus shows different dynamics. The example in Fig. 3.19 was obtained by adding a very basic explicit step to compute viscosity; however, this is slow and unstable and thus not included in our standard solver.

### 3.7.2 Black film

As a film keeps thinning through evaporation or gravity drag, at some point it becomes so thin that destructive interference takes place, and the film appears completely black. The thickness is then about 5 to 30 nm [100, 58].



(a) Viscous soap film



(b) Inviscid soap film

Figure 3.19: Two simulations with/without viscosity term  $Re^{-1}\vec{V}$ , otherwise under the same condition and after same frame numbers. A viscous film tends to keep its texture longer in shape and has a reduced tendency to break into fractal structures.

At such a small scale, molecular forces come into play, such as Van der Waals attraction, electrostatic repulsion, and Born repulsion. These forces cause black film to be surprisingly stable and form sharply defined “islands” within the colorful film (Fig. 3.20). In future work, it will be interesting to include such molecular forces in an extended model.

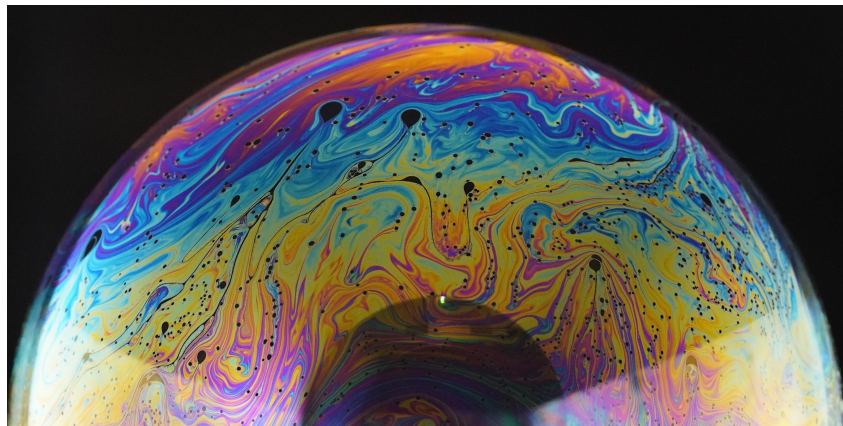


Figure 3.20: Black film on a soap bubble (photograph)

## 4. A Microfacet-based Hair Scattering Model

The content of this chapter has been published as:

Weizhen Huang, Matthias B Hullin, and Johannes Hanika.  
A microfacet-based hair scattering model.  
In *Computer Graphics Forum*, volume 41, pages 79–91. Wiley Online Library, 2022.  
DOI: 10.1111/cgf.14588

### Summary

The modern hair rendering model, established by Marschner et al. [76] and improved by d’Eon et al. [26, 28], is based on the assumption that the scattering distribution function is separable along the fiber direction and the azimuthal direction. While this assumption simplifies the model, its validity has not been justified. Recent measurements [66] have revealed strong scattering in the forward direction, which our simulations confirm to match well with ray-traced results from a rough cylinder. Based on this observation, we propose to model human hair as rough dielectric cylinders with a microfacet surface, which is the standard model in computer graphics for surface roughness.

To make ray tracing efficient and practical, we follow the previous approach of establishing a far-field model, where incident light on a hair fiber is assumed to be collimated due to the small size of the hair, allowing us to compute the scattering across the entire width of the fiber. The scattering function is further decomposed into components based on the number of surface interactions, with the first three components being R (reflection), TT (transmission-transmission) and TRT (transmission-reflection-transmission). Higher order components are omitted due to increasing computational cost and decreasing contribution to the overall appearance.

For the R component, we observe that the integral equation takes a similar form as the Cook-Torrance BRDF [21] and is computationally straightforward. When using the GGX distribution without the shadowing-masking term, an analytical solution exists. However, for components beyond R, we need to integrate not only across the fiber width but also along all the possible internal paths. These higher-order integrations pose challenges for deterministic numerical integration due to the curse of dimensionality. Therefore, we employ a combined technique of Simpson’s method for integration along the fiber width, and sampling a microfacet at each interface to choose a specific internal path, similar as in Monte Carlo ray tracing. By dividing the sampling probability, we greatly simplify the integral equation, making it practical to solve on the fly.

Since such integration is generic and does not rely on assumptions about the underlying shape, our model naturally extend, almost with almost no additional computational cost, to elliptical hair cross-sections, which is the shape of most human hairs.

The rendered results demonstrate narrow and bright reflections in the forward scattering direction and the angle-dependent highlights due to elliptical cross-sections, aligning well with both microscopic measurements and photographs.

Despite its many advantages, our model has some limitations. One obvious shortcoming is the introduced energy loss, as it inherits the energy loss of single-scattering microfacet models. However, well-established algorithms for addressing this issue in general microfacet models, such as multiple-scattering [50] and albedo scaling [121] can be directly applied to our model. Another limitation is that our model ignores wave-optics effects, which can be prominent on dark hairs under sunlight. This limitation could potentially be addressed by implementing complex ray tracing.

**Author Contribution:** I proposed the research topic and conducted a thorough literature review. Furthermore, I designed the rendering model, including the derivation of all necessary equations and the development of a combined deterministic and non-deterministic integration scheme. Moreover, I successfully implemented the rendering model in Mitsuba and performed comparisons against other existing models, validating the accuracy of our approach.

Johannes Hanika provided valuable feedback on the overall design, shared relevant code for reference, and contributed to the literature review section. Matthias Hullin suggested to align the ellipse direction with the curvature vector, smoothed the hair curve, and revised the manuscript.

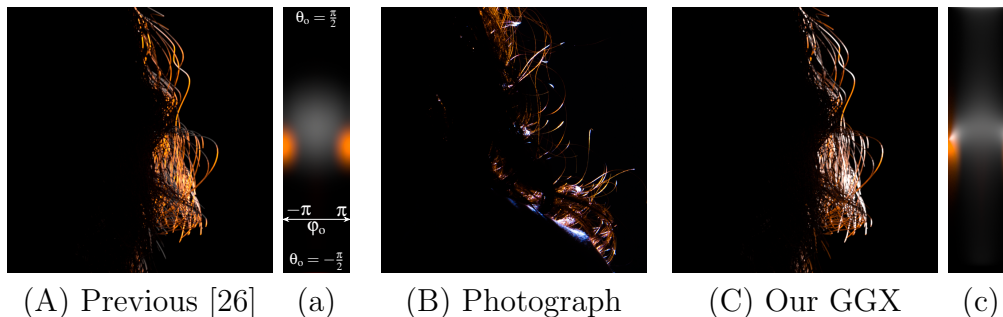


Figure 4.1: Details of a backlit studio scene rendered using a state-of-the-art separable hair scattering model (A) and the proposed model (C), both compared with a photograph under similar lighting conditions (B) (© Martyn Thompson <https://photographymk.co.uk>), with visualization of the BCSDF (a,c) as plotted against  $\theta_o/\varphi_o$ , illumination angle  $\theta_i = 0$ . The strongly focused reflection in the forward scattering direction seen in (C,c) gives rise to a glint-like appearance that the previous separable hair scattering models have been unable to capture. (Exposure of (a,c) is scaled up by 2.5 stops to improve feature visibility. (A,C) are close-up images of Fig. 4.13.)

## Abstract

The development of scattering models and rendering algorithms for human hair remains an important area of research in computer graphics. Virtually all available models for scattering off hair or fur fibers are based on separable lobes, which bring practical advantages in importance sampling, but do not represent physically-plausible microgeometry. In this chapter, we contribute the first microfacet-based hair scattering model. Based on a rough cylinder geometry with tilted cuticle scales, our far-field model is non-separable by nature, yet allows accurate importance sampling. Additional benefits include support for elliptical hair cross-sections and an analytical solution for the reflected lobe using the GGX distribution. We show that our model captures glint-like forward scattering features in the reflected lobe that have been observed before but not properly explained.

## 4.1 Introduction

Rendering realistic hair is important for virtual creatures and humans. It has thus received attention in computer graphics literature early on [64]. A more detailed look at the effects contributing to the distinct look of hair

established that the dielectric fiber surface reflects (R) and transmits (T) part of the light [76]. Most prominently, the scattering distribution of hair is composed of an R lobe, a TT lobe, and a TRT lobe, denoted by the type and order of interactions between the light path and the fiber surface. Hair has slightly tilted cuticle scales on the surface, which are responsible for a shift between the direct highlight (R) and the secondary highlight (TRT). Also, light passing through the pigmented fiber picks up the distinct coloration of the material and results in the lively appearance of the two above-mentioned highlights. Lobes of higher order, where the light has passed through the fiber multiple times (TRRT, ...) exist as well, but are usually weak enough to be neglected thanks to repeated absorption.

Monte Carlo path tracing of hair is hard: the size of the individual fibers is usually small (on the order of a tenth of a millimeter), so already finding an intersection of a ray with such a sub-pixel-sized object is hard. To counter this, analytic fiber scattering models pre-integrate over the cross-section of the hair: the geometric primitive to intersect is not actually a cylinder, but a ray-facing stripe, and the curvature of the cylinder is included in the equations for the lobes. This way it is certain that all offsets from the stripe center, *i.e.* normals on the cylinder, are considered appropriately.

This approach poses a set of challenging mathematical problems. To make these tractable, separating the equations into a longitudinal and azimuthal factor was proposed [76]. This mathematical simplification was so successful that it can be found in the most advanced models to date. On the flip side, this artificial factorization of the scattering lobes does not have a physical motivation. Basing advanced models on this assumption has thus become increasingly hard, resulting in complicated equations which still fail to capture even simulated reference faithfully in all cases.

In parallel to this development, microfacet-based surface reflectance models have gained popularity in computer graphics and have been studied in quite some detail. We revisit fiber scattering models with this background and devise a *bidirectional curve scattering distribution function* (BCSDF) which is rooted in microfacet theory. We still intersect ray-facing stripes, but then include a cylindrical macrosurface, tilted scales as mesosurface, as well as a microsurface with Beckmann or GGX normal distribution function in our analysis. This formulation naturally includes glinty behavior at grazing angles and a non-separable shape of the lobes in longitudinal/azimuthal space. The existence of this shape has been observed before [28, 66], but could not be reproduced with a physically based model. We show how a physically-plausible surface model simplifies working with the BCSDF: importance sampling boils down to sampling microfacets, a closed-form solution exists for the GGX R lobe, and the model naturally extends to elliptical fiber

macrogeometry.

In summary, our contributions are:

- the first fiber scattering model based on physically-plausible macro-, meso-, and microgeometry,
- accurate importance sampling despite non-separable lobes,
- an analytic form of the resulting integral for the R lobe with GGX microroughness,
- a natural extension to elliptical cross-sections.

## 4.2 Background and Related Work

**Light transport.** Physically based rendering has a long history [94]. The most successful numerical method to solve the integrals appearing in the transport equations is Monte Carlo path tracing. Materials are included in the physical model via the *bidirectional scattering distribution function* (BSDF), which relates incoming irradiance to outgoing radiance. This function is valid on locally flat surfaces and is often derived from statistical models of the microsurface by applying a far-field assumption. Analogous to that, there is the BCSDF which models the same material properties assuming a ray-facing stripe as underlying geometry, *i.e.*, it can encode the curvature of a cylinder inside it.

**Fiber scattering models.** Most if not all fiber scattering models in computer graphics today can be traced back to Marschner’s work [76]. After intersecting a ray-facing curve primitive, the BCSDF is evaluated when connecting to the light source. To make the definition of this BCSDF tractable, they separated the model into a longitudinal (depending on  $\theta$ ) and an azimuthal part (depending on  $\varphi$ ). These two are multiplied together to form the final lobe. In addition to that, the full model consists of multiple lobes, one for the directly reflected light (R), the light transmitting through the fiber (TT) and the lobe formed by light entering the fiber, and exiting it again after internal reflection (TRT). This scheme can be extended indefinitely, but the contribution of the higher-order lobes vanishes soon.

In Monte Carlo path tracing, importance sampling and energy conservation are important topics and have been looked into [26, 19]. Also, there is an excellent implementation guide [94] of Chiang et al.’s work [19]. Later, the model has been extended to structures inside the fiber and for a stochastic

near- and far-field model [138, 136]. The importance of elliptical hair fiber cross-sections has been pointed out and a specialized azimuthal scattering function has been devised to this end [66]. The model has even been extended to include certain effects of diffraction [134, 11], while still keeping the original assumption of longitudinal/azimuthal separability. We do not consider wave-optics in this work.

The notable exception to this pattern is a paper by d’Eon et al. [28], who showed that the non-separable nature of the reflectance field causes a strong, focused forward scattering effect. They conducted an offline Monte Carlo simulation of a rough dielectric cylinder, which is the underlying geometry of the Marschner model [76], and hand-tailored a non-separable model that would match their observation better. Since importance-sampling a non-separable 2D function is not trivial, they proposed an approximate way of approaching this problem.

We take their observation further and show that the underlying geometry of a rough dielectric cylinder can be traced directly using microfacet theory without the effort of separation. The resulting lobes match the Monte Carlo reference much closer than previous approaches. Since it is based on well-studied microfacet models, we can importance sample the lobes of our model exactly using standard inverse-CDF sampling.

**Microfacet theory** has a long history in literature, as it is relevant to antenna theory and heat transfer, with which physically based rendering shares a great deal of theory. The surface of a material is thought of as a set of microfacets with certain reflection properties. Often they are assumed to be perfect mirrors with material specific Fresnel behavior [21]. The geometry of the microsurface is modeled statistically, to avoid instantiating and ray tracing a multitude of geometric primitives. Certain random distributions of the height and normals of the facets can be applied, and most often they are assumed to be uncorrelated with each other, *i.e.* the surface consists of disconnected, independent facets (a Smith surface [107]). The foundation of modern microfacet models in computer graphics is Heitz’ work [48]. The generic form of a *bidirectional reflectance distribution function* (BRDF) for scattering on flat surfaces is

$$f_{\text{r}}(\omega_{\text{i}}, \omega_{\text{o}}) = \frac{F(\omega_{\text{h}}, \omega_{\text{o}})G(\omega_{\text{o}}, \omega_{\text{i}}, \omega_{\text{h}})D(\omega_{\text{h}})}{4|\omega_{\text{m}} \cdot \omega_{\text{o}}||\omega_{\text{m}} \cdot \omega_{\text{i}}|}. \quad (4.1)$$

Here,  $\omega_{\text{i}}$  and  $\omega_{\text{o}}$  are the incident and outgoing directions,  $\omega_{\text{h}}$  is the half vector (or, equivalently, the micronormal),  $\omega_{\text{m}}$  the geometric normal of the macrosurface,  $F$  is the Fresnel term, and  $G$  the combined geometric factor for

shadowing and masking within the microsurface. This model only represents single scattering in the microsurface, so it fulfills energy conservation only insofar as it does not generate energy. Since it lacks multiple scattering contributions [50, 72, 121], it will be visibly too dark for very rough surfaces.

There has been a lot of interest in surface scattering models that exhibit off-center reflectance peaks, *i.e.* the mean orientation of the microfacets is not aligned with the normal of the triangle mesh. To this end, the surface orientation can be divided up in micronormal, mesonormal, and macronormal [30]. To arrive at a consistent surface model, the mesosurface has to be closed. Schüßler et al. [104] devise such a model including multiple scattering in the mesosurface for normal maps.

The case analyzed in our work is similar: the macrosurface is a cylinder, the mesosurface consists of tilted cuticle scales, and the microsurface is a Smith surface. We apply microfacet theory to this setting and arrive at a reflectance model for hair fibers, including R, TT, and TRT lobes for circular and elliptical cross-sections.

## 4.3 Model

In this section, we describe our model and its implementation details. First, we will describe the geometry and derive the basic lobe evaluation formulas in Section 4.3.1. Extensions to scale tilt (Section 4.3.2) and elliptical cross-sections (Section 4.3.3) follow after. Section 4.3.4 then summarizes aspects related to the requirements of Monte Carlo rendering system: evaluation, importance sampling, evaluation of the *probability distribution function* (PDF).

### 4.3.1 A Microfacet BCSDF

We model the fiber as a cylinder with microfacet surface roughness, having a radius of 1 (Fig. 4.2). In accordance with former fiber- and hair-models, we associate the outgoing radiance  $L_o$  with the incoming radiance  $L_i$  via the BCSDF  $S(\omega_i, \omega_o)$

$$L_o(\omega_o) = \int L_i(\omega_i) S(\omega_i, \omega_o) \cos \theta_i d\omega_i. \quad (4.2)$$

We limit our discussion to R, TT, and TRT lobes, therefore

$$S(\omega_i, \omega_o) = S_R(\omega_i, \omega_o) + S_{TT}(\omega_i, \omega_o) + S_{TRT}(\omega_i, \omega_o). \quad (4.3)$$

The relevant vectors to appear in the following subsections are illustrated in Fig. 4.3.

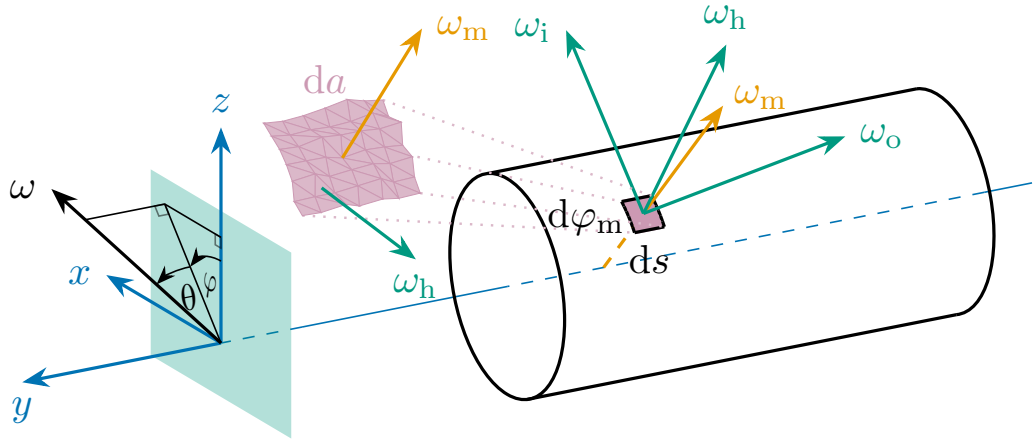


Figure 4.2: An illustration of the geometry of our hair scattering model. The longitudinal-azimuthal parameterization is shown on the left. The longitudinal angle  $\theta$  is defined as the angle between  $\omega$  and the  $x - z$  plane, and the azimuthal angle  $\varphi$  is the angle between the  $z$  axis and the projection of  $\omega$  onto the  $x - z$  plane.  $da$  is a differential surface element with macronormal  $\omega_m$ , which is composed of specular microfacets  $\omega_h$  with associated normal distribution  $D(\omega_h, \omega_m)$ .

### Reflection Lobe $S_R$

For perfectly specular microfacets, only the half-angle vector  $\omega_{h1} = \widehat{\omega_i + \omega_o}$  contributes to the reflection from  $\omega_i$  to  $\omega_o$ . Consider a differential surface area element

$$da_{m1} = d\varphi_{m1} ds \quad (4.4)$$

with the macronormal direction  $\omega_{m1}$  and the differential length  $ds$  along the fiber. Such a differential surface has an associated distribution  $D(\omega_{h1}, \omega_{m1})$  of micronormals  $\omega_{h1}$ , which satisfies

$$\int_{\mathcal{H}^2(\omega_{m1})} D(\omega_{h1}, \omega_{m1}) |\omega_{h1} \cdot \omega_{m1}| d\omega_{h1} = 1, \quad (4.5)$$

where  $|\cdot|$  denotes the absolute value of the dot product. The area of the differential surface element  $da_{h1}$  with micronormals  $\omega_{h1}$  is

$$da_{h1} = D(\omega_{h1}, \omega_{m1}) d\omega_{h1} da_{m1}. \quad (4.6)$$

The differential flux  $d\Phi_{h1}$  received by such microfacets is

$$d\Phi_{h1} = L_i(\omega_i) d\omega_i |\omega_i \cdot \omega_{h1}| da_{h1}. \quad (4.7)$$

Multiplying the Fresnel reflectance gives

$$d\Phi_o = R(\omega_{h1}, \omega_o) d\Phi_{h1}, \quad (4.8)$$

the differential outgoing flux from the surface element  $da_{m1}$ . The total outgoing flux is given by integrating the differential flux. Therefore, the average outgoing radiance from the fiber is

$$L_o(\omega_o) = \frac{\int d\Phi_o}{d\omega_o a_o^\perp}, \quad (4.9)$$

where

$$a_o^\perp = 2 \cos \theta_o ds \quad (4.10)$$

is the projected area of the full-width fiber in the outgoing direction. Making use of the half-angle mapping  $d\omega_{h1} = \frac{d\omega_o}{4|\omega_{h1} \cdot \omega_i|}$  and combining Eqs. (4.4) and (4.6) to (4.10), we obtain

$$L_o(\omega_o) = \iint \frac{L_i(\omega_i) R(\omega_{h1}, \omega_o) D(\omega_{h1}, \omega_{m1}) d\varphi_{m1} d\omega_i}{8 \cos \theta_o}. \quad (4.11)$$

Comparing Eq. (4.11) with Eq. (4.2) and adding the Smith shadowing-masking term  $G_{\omega_{m1}}(\omega_i, \omega_o)$  gives the BCSDf for the R lobe

$$S_R(\omega_i, \omega_o) = \frac{R(\omega_{h1}, \omega_o)}{8 \cos \theta_o \cos \theta_i} \int D(\omega_{h1}, \omega_{m1}) G_{\omega_{m1}}(\omega_i, \omega_o) d\varphi_{m1}. \quad (4.12)$$

Different from former fiber models [76, 26, 138, 136], we do not separate the BCSDf into longitudinal and azimuthal components; rather, we compute the half-angle vector  $\omega_{h1}$  between incoming and outgoing angles, and integrate its distribution along the azimuth. Other than this integration, Eq. (4.12) is almost identical with the Cook-Torrance BRDF in Eq. (4.1), which makes sense, since we have applied the same model on a curved surface, instead of on a flat surface.

Hair usually has low roughness values, therefore,  $G \approx 1$  holds for a large range of normal directions. Interestingly, if ignoring the shadowing-masking function, an analytical solution of Eq. (4.12) exists for GGX roughness. The result can be found in Appendix E.

### Secondary Lobes $S_{TT}$ and $S_{TRT}$

The BCSDfs for TT and TRT lobes are derived in similar ways. The differential flux transmitted through interface ① (Fig. 4.3) is

$$d\Phi_t = T_1 d\Phi_{h1}, \quad (4.13)$$

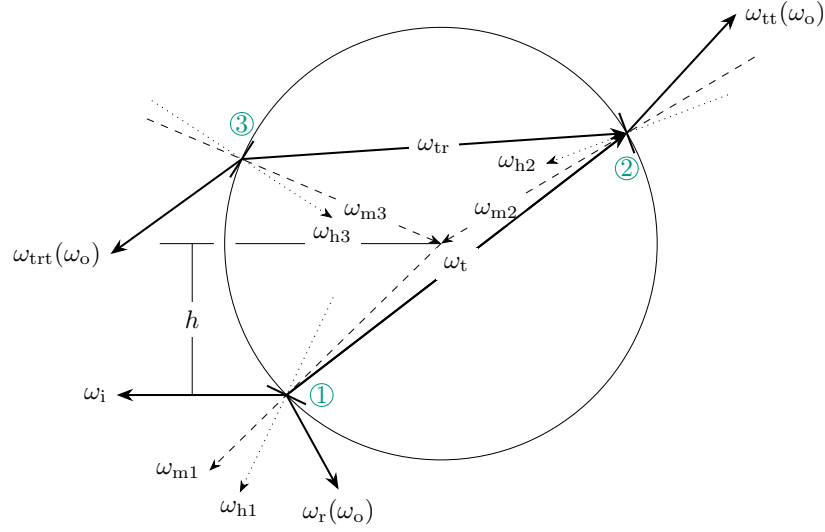


Figure 4.3: R, TT and TRT scattering from a circular cross-section. At each interface with macro/mesonormals  $\omega_{mi}$ ,  $i \in 1, 2, 3$ , the ray hits a microfacet (denoted with thick line segments) with normal  $\omega_{hi}$ , after which it undergoes specular reflection and refraction. Note the directions the vectors are pointing to.  $h \in [-1, 1]$  denotes the azimuthal offset.

where  $T_1 = 1 - R(\omega_{h1}, \omega_o)$  is the Fresnel transmittance. The corresponding radiance is

$$L_t = \frac{d\Phi_t}{d\omega_t da_t^\perp}, \quad (4.14)$$

with

$$da_t^\perp = |\omega_t \cdot \omega_{m1}| da_{m1} \quad (4.15)$$

being the projected microsurface area in the direction of  $\omega_t$ . The differential flux received by microfacets with normal direction  $\omega_{h2}$  is

$$d\Phi_{h2} = A_t L_t d\omega_t |\omega_t \cdot \omega_{h2}| da_{h2}. \quad (4.16)$$

Here we have introduced  $A_t$  as the absorption due to pigments inside the hair as the ray travels along  $\omega_t$ . Two kinds of pigments are responsible for absorption inside hair: eumelanin and pheomelanin with concentrations  $\rho_e$  and  $\rho_p$ , respectively. Let  $\sigma_a = \rho_e \sigma_{a,e} + \rho_p \sigma_{a,p}$  be the absorption per unit length [29], then

$$A_t = \exp\left(-\sigma_a \frac{2 \cos(\varphi_t - \varphi_{m1} + \pi)}{\cos \theta_t}\right). \quad (4.17)$$

Note that the path length  $2 + 2 \cos(2\gamma_t)$  in the original model [76] and its derivation [26] has left out a square root when applying law of cosines and is erroneous, it should be  $2 \cos \gamma_t$ , as the term in Pharr's work [93].

Similar to Eq. (4.6), the area of the surface element  $da_{h2}$  with micronormals  $\omega_{h2}$  is given by

$$da_{h2} = D(\omega_{h2}, \omega_{m2}) d\omega_{h2} da_{m2}, \quad (4.18)$$

with

$$da_{m2} = d\varphi_{m2} ds. \quad (4.19)$$

Thus, the outgoing flux for the TT component is

$$d\Phi_o = T_2 d\Phi_{h2}, \quad (4.20)$$

with  $T_2 = 1 - R(\omega_{h2}, \omega_t)$  being the Fresnel transmittance through interface ②. Note the change in relative refractive index when exiting the fiber. Further, the half vector and the outgoing direction is related by

$$\begin{aligned} d\omega_{h1} &= \frac{\eta^2}{\|\bar{\omega}_{h1}\|^2} |\omega_t \cdot \omega_{h1}| d\omega_t, \\ d\omega_{h2} &= \frac{1}{\eta^2 \|\bar{\omega}_{h2}\|^2} |\omega_{tt} \cdot \omega_{h2}| d\omega_o, \end{aligned} \quad (4.21)$$

with  $\bar{\omega}_{h1} = -\omega_i - \eta\omega_t$  and  $\bar{\omega}_{h2} = -\omega_t + \omega_o/\eta$  being the unnormalized normal vectors and  $\|\cdot\|$  their norms, and  $\eta$  the relative refractive index of hair with respect to air. Combining Eqs. (4.6), (4.7), (4.9), (4.10), (4.13) to (4.16) and (4.18) to (4.21), we obtain

$$\begin{aligned} L_o &= \frac{L_i}{2 \cos \theta_o} \int \frac{T_1 T_2}{\|\bar{\omega}_{h1}\|^2 \|\bar{\omega}_{h2}\|^2} |\omega_i \cdot \omega_{h1}| |\omega_t \cdot \omega_{h1}| |\omega_o \cdot \omega_{h2}| |\omega_t \cdot \omega_{h2}| \\ &\quad \iint \frac{D_1 D_2 G_1 G_2 A_t}{|\omega_t \cdot \omega_{m1}|} d\varphi_{m2} d\omega_t d\omega_i. \end{aligned} \quad (4.22)$$

Here we have simplified  $D(\omega_{hi}, \omega_{mi})$  as  $D_i$ , and the shadowing-masking term at interface ② as  $G_i$ . Making use of  $\varphi_{m1} = 2\varphi_t - \varphi_{m2}$ , the BCSDf for the TRT lobe is given as

$$\begin{aligned} S_{TT}(\omega_i, \omega_o) &= \frac{1}{2 \cos \theta_o \cos \theta_i} \\ &\quad \int \frac{T_1 T_2}{\|\bar{\omega}_{h1}\|^2 \|\bar{\omega}_{h2}\|^2} |\omega_i \cdot \omega_{h1}| |\omega_t \cdot \omega_{h1}| |\omega_o \cdot \omega_{h2}| |\omega_t \cdot \omega_{h2}| \\ &\quad \int \frac{D_1 D_2 G_1 G_2 A_t}{|\omega_t \cdot \omega_{m1}|} d\varphi_{m1} d\omega_t. \end{aligned} \quad (4.23)$$

Repeating the above process at interface ③, we obtain the BCSDf for the TRT lobe

$$\begin{aligned}
S_{\text{TRT}}(\omega_i, \omega_o) = & \frac{1}{8 \cos \theta_o \cos \theta_i} \int \frac{T_1}{\|\bar{\omega}_{h1}\|^2} |\omega_t \cdot \omega_{h1}| |\omega_i \cdot \omega_{h1}| \\
& \int \frac{R_2 T_3}{\|\bar{\omega}_{h3}\|^2} |\omega_{\text{tr}} \cdot \omega_{h3}| |\omega_o \cdot \omega_{h3}| \\
& \int \frac{D_1 D_2 D_3 G_1 G_2 G_3 A_t A_{\text{tr}}}{|\omega_t \cdot \omega_{m1}| |\omega_{\text{tr}} \cdot \omega_{m2}|} d\varphi_{m1} d\omega_{\text{tr}} d\omega_t, \quad (4.24)
\end{aligned}$$

with

$$A_{\text{tr}} = \exp \left( -2\sigma_a \frac{\cos(\varphi_{\text{tr}} - \varphi_{m2} + \pi)}{\cos \theta_{\text{tr}}} \right) \quad (4.25)$$

and making use of  $\varphi_{m3} = \varphi_{m1} - 2(\varphi_t - \varphi_{\text{tr}}) + \pi$ .

### 4.3.2 Scale Tilt

Hairs have tilted surface scales [76], resulting a shift of the macronormal from  $\omega_m = [\sin \varphi_m, 0, \cos \varphi_m]^\top$  to the mesonormal  $\omega_{m\alpha} = [\sin \varphi_m \cos \alpha, \sin \alpha, \cos \varphi_m \cos \alpha]^\top$ , with  $\alpha$  being the tilt angle. Also, additional intersection test with the cylinder body should be performed. Otherwise, the BCSDFs remains the same.

When sampling microfacets from a tilted geometric normal, the projected area as in Eq. (4.10) is also supposed to change; however, keep  $a_o^\perp$  unchanged seems to bring only very slight discrepancy at grazing angles (Fig. 4.9). Therefore, we only adjust the macronormal itself for simplicity. Since we have completely replaced the macronormal with the mesonormal wherever it appears, they share the same notation  $\omega_m$  throughout the work, except for the discussion in Section 4.4.1 where a differentiation is needed.

It has been assumed that a scale tilt of  $\alpha$  causes the outgoing longitudinal angle of the R lobe to be deflected by  $2\alpha$  [76]. However, this is only true when  $\varphi_i = \varphi_o$ . When  $|\varphi_i - \varphi_o| \rightarrow \pi$ ,  $\theta_o$  converges to  $-\theta_i$ , the same as without scales. We illustrate this phenomenon in Fig. 4.4. This also results in a distinctly non-separable contraction of the R lobe at both sides near the grazing angle (see Section 5.5). To our knowledge, d'Eon et. al [28] are the first to mention and model the dependence of  $\theta_o$  on  $|\varphi_i - \varphi_o|$  in the presence of cuticle scales. However, they mainly focus on deriving the expression for the specular cone in the presence of a scale tilt, then add a cosine-modulated longitudinal width around this specular cone. Such formulation describes this contraction in a phenomenological way, rather than being an explanation of the physical process, thus resulting in a non-separable lobe which is difficult to importance-sample.

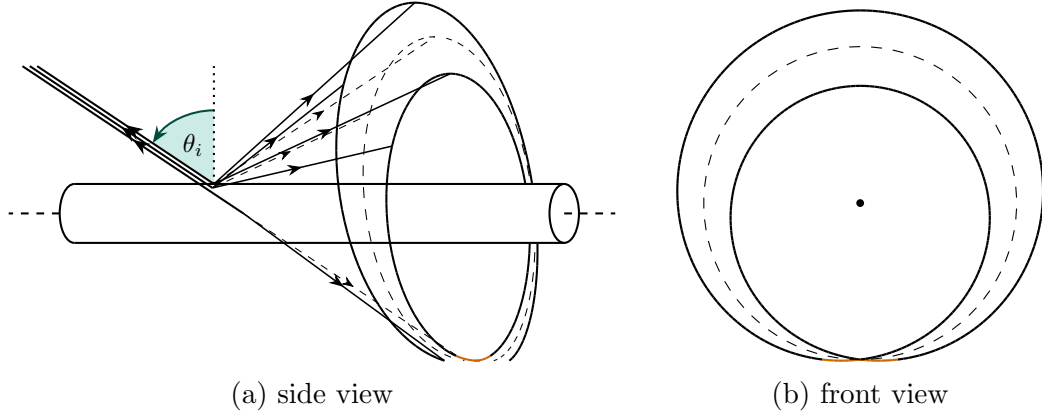


Figure 4.4: Parallel rays reflected off a smooth cylinder. Without cuticle scales, the reflected rays are restricted to a specular cone (dashed). In the presence of cuticle scales, the reflected rays form a conical surface but not a cone anymore (solid). We demonstrate the case for  $\alpha = 4^\circ$  and  $\alpha = -4^\circ$ . Regions that are unreachable because of invisibility is marked red. For the purpose of illustration, the radius of the cylinder is set to zero in the front view.

### 4.3.3 Extending the Model to Elliptical Hair Fibers

Our model does not only work for circular cross-sections; in general, the above idea can be applied to any smooth convex shape. The key changes lie in adjusting the differential surface area element  $da_m$  and the projected area in the outgoing direction  $a_o^\perp$ . We demonstrate the necessary modifications for elliptical cross-sections, as real hair fibers are often roughly elliptical [11, 66].

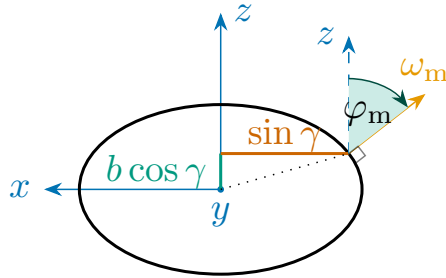


Figure 4.5: An elliptical cross-section

Assuming the ellipse is parameterized by  $x = \sin \gamma, z = b \cos \gamma, \gamma \in [-\pi, \pi]$  (Fig. 4.5). This gives eccentricity  $e = \sqrt{1 - b^2}$ . The normal vector of a point on the ellipse is  $[\sin \varphi, \cos \varphi]^\top$ , or  $[b \sin \gamma, \cos \gamma]^\top$ .  $da_m$  in Eqs. (4.4)

and (4.19) now becomes

$$da_m = \sqrt{1 - e^2 \sin^2 \gamma_m} d\gamma_m ds, \quad (4.26)$$

and  $a_o^\perp$  in Eq. (4.10) is replaced by

$$a_o^\perp = 2\sqrt{1 - e^2 \sin^2 \varphi_o} \cos \theta_o ds. \quad (4.27)$$

After replacing these terms in the above derivation, we arrive at the BCSDF for elliptical fibers

$$S_R(\omega_i, \omega_o) = \frac{R_1}{8\sqrt{1 - e^2 \sin^2 \varphi_o} \cos \theta_o \cos \theta_i} \int D_1 G_1 \sqrt{1 - e^2 \sin^2 \gamma_{m1}} d\gamma_{m1}, \quad (4.28)$$

$$S_{TT}(\omega_i, \omega_o) = \frac{1}{2\sqrt{1 - e^2 \sin^2 \varphi_o} \cos \theta_o \cos \theta_i} \int \frac{T_1 T_2}{\|\bar{\omega}_{h1}\|^2 \|\bar{\omega}_{h2}\|^2} |\omega_i \cdot \omega_{h1}| |\omega_t \cdot \omega_{h1}| |\omega_o \cdot \omega_{h2}| |\omega_t \cdot \omega_{h2}| \int \frac{D_1 D_2 G_1 G_2 A_t \sqrt{1 - e^2 \sin^2 \gamma_{m2}}}{|\omega_t \cdot \omega_{m1}|} d\gamma_{m1} d\omega_t, \quad (4.29)$$

$$S_{TRT}(\omega_i, \omega_o) = \frac{1}{8\sqrt{1 - e^2 \sin^2 \varphi_o} \cos \theta_o \cos \theta_i} \int \frac{T_1}{\|\bar{\omega}_{h1}\|^2} |\omega_t \cdot \omega_{h1}| |\omega_i \cdot \omega_{h1}| \int \frac{R_2 T_3}{\|\bar{\omega}_{h3}\|^2} |\omega_{tr} \cdot \omega_{h3}| |\omega_o \cdot \omega_{h3}| \int \frac{D_1 D_2 D_3 G_1 G_2 G_3 A_t A_{tr} \sqrt{1 - e^2 \sin^2 \gamma_{m3}}}{|\omega_t \cdot \omega_{m1}| |\omega_{tr} \cdot \omega_{m2}|} d\gamma_{m1} d\omega_{tr} d\omega_t. \quad (4.30)$$

Further, it holds that  $\gamma_{m2} = 2 \tan^{-1}(b \tan \varphi_t) - \gamma_{m1}$ , and  $\gamma_{m3} = \gamma_{m1} - 2(\tan^{-1}(b \tan \varphi_t) - \tan^{-1}(b \tan \varphi_{tr})) - \pi$ . The attenuation terms  $A_{t,tr}$  depend on the distance through the medium inside the fiber, which can be obtained by taking the difference between the intersection points divided by  $\cos \theta_{t,tr}$ .

Compared to Eqs. (4.12), (4.23) and (4.24), above BCSDFs turn out to have only two additional terms, which is a very minor change.

### 4.3.4 Implementation

In this section, we provide the implementation details of our model, including sampling, evaluating the BCSDF and the PDF. The code is provided in <https://github.com/RiverInTheSky/roughhair>.

#### Importance Sampling

Since our model is based on the microfacet theory, the sampling procedure boils down to sampling microfacets at each intersection. For simplicity, we denote the vectors with their spherical coordinates as  $\omega_x = \{\theta_x, \varphi_x\}$ . The importance sampling for circular hair fibers works as follows:

- Randomly select an azimuthal offset  $h$ , similar to d'Eon et al. [27].
- Compute the mesonormal  $\omega_{m1} = \{\alpha, -\sin^{-1} h\}$ , sample a micronormal  $\omega_{h1}$ , compute the Fresnel reflectance, that is the attenuation of the R lobe  $\mathcal{A}_R = R_1$ .
- Compute the refracted ray via

$$\omega_t = \frac{1}{\eta} \left( \left( |\omega_i \cdot \omega_{h1}| - \sqrt{\eta^2 + |\omega_i \cdot \omega_{h1}|^2 - 1} \right) \omega_{h1} - \omega_i \right),$$

compute the mesonormal  $\omega_{m2} = \{-\alpha, 2\varphi_t - \varphi_{m1}\}$  at interface ②, sample a micronormal  $\omega_{h2}$ , compute the Fresnel reflectance  $R_2$  and the absorption  $A_t$  along  $\omega_t$ . The attenuation of the TT lobe is then  $\mathcal{A}_{TT} = T_1 T_2 A_t$ , with  $T_i = 1 - R_i$ .

- Compute the reflected ray via  $\omega_{tr} = 2|\omega_t \cdot \omega_{h2}|\omega_{h2} - \omega_t$ , compute the mesonormal  $\omega_{m3} = \{-\alpha, \varphi_{m1} - 2(\varphi_t - \varphi_{tr}) + \pi\}$ , sample a micronormal  $\omega_{h3}$ , compute the Fresnel transmittance  $T_3$  and the absorption  $A_{tr}$  along  $\omega_{tr}$ . The attenuation of the TRT lobe is then  $\mathcal{A}_{TRT} = T_1 R_2 T_3 A_t A_{tr}$ .
- Select a lobe with the probability in proportion to the attenuation, compute the outgoing direction of the selected lobe, return sample weight  $\mathcal{A}_R + \mathcal{A}_{TT} + \mathcal{A}_{TRT}$ , multiplied by the visibility term  $G$  in the outgoing direction.

A total of 8 random numbers are needed in this procedure.

## BCSDF evaluation

The integration in Eq. (4.12) can be evaluated either analytically (ignoring the GGX shadowing-masking function, see Appendix E) or numerically. For the numerical method, we apply composite Simpson’s rule. More sub-intervals are needed when more of the cylinder is visible from both the incoming and the outgoing angles. We found that a step size of  $0.7\beta$  delivers satisfying results, with  $\beta$  being the GGX or Beckmann roughness. For  $\beta = 0.08$ , an average of  $\sim 28$  sub-intervals are needed to integrate the R lobe.

Evaluating Eqs. (4.23) and (4.24) is trickier, as they involve integration in 3D and 5D, respectively, which is extremely costly to evaluate with deterministic numerical integration methods due to the curse of dimensionality. We suggest precomputing them and storing the result in a 3D look-up table (4D for elliptical cross-sections), or to apply our proposed combined Monte Carlo-Simpson integration on the fly: That is, for each  $\varphi_{m1}$ , we sample an internal path, connect it with the outgoing direction, then compute the integrand along the path, divided by the probability of sampling the internal path.

For the TT lobe,  $\omega_{h1}$  is sampled,  $\omega_{h2}$  is computed via  $\omega_{h2} = -\widehat{\omega_t + \omega_o}/\eta$ . If we importance-sample visible microfacets [49], then Eq. (4.23) is evaluated as

$$S_{\text{TT}}(\omega_i, \omega_o) \approx \frac{1}{2 \cos \theta_o \cos \theta_i} \int \frac{T_1 T_2 G_1(\omega_t) D_2 G_2 A_t}{\eta^2 \|\bar{\omega}_{h2}\|^2} \frac{|\omega_i \cdot \omega_{m1}| |\omega_o \cdot \omega_{h2}| |\omega_t \cdot \omega_{h2}|}{|\omega_t \cdot \omega_{m1}|} d\varphi_{m1}, \quad (4.31)$$

with  $G_1(\omega_t)$  being the one-sided Smith’s shadowing-masking function for direction  $\omega_t$  at surface normal  $\omega_{m1}$ .

For the TRT lobe,  $\omega_{h1}$  and  $\omega_{h2}$  are sampled,  $\omega_{h3}$  is computed via  $\omega_{h3} = \widehat{\omega_{tr} + \omega_o}/\eta$ . Also sampling visible microfacets, Eq. (4.24) is evaluated as

$$S_{\text{TRT}}(\omega_i, \omega_o) \approx \frac{1}{2 \cos \theta_o \cos \theta_i} \int \frac{T_1 R_2 T_3 G_1(\omega_t) G_2(\omega_{tr}) D_3 G_3 A_t A_{tr}}{\eta^2 \|\bar{\omega}_{h3}\|^2} \frac{|\omega_{tr} \cdot \omega_{h3}| |\omega_o \cdot \omega_{h3}| |\omega_i \cdot \omega_{m1}| |\omega_t \cdot \omega_{m2}|}{|\omega_t \cdot \omega_{m1}| |\omega_{tr} \cdot \omega_{m2}|} d\varphi_{m1}, \quad (4.32)$$

with  $G_2(\omega_{tr})$  being Smith’s shadowing-masking function for direction  $\omega_{tr}$  when the surface normal is  $\omega_{m2}$ .

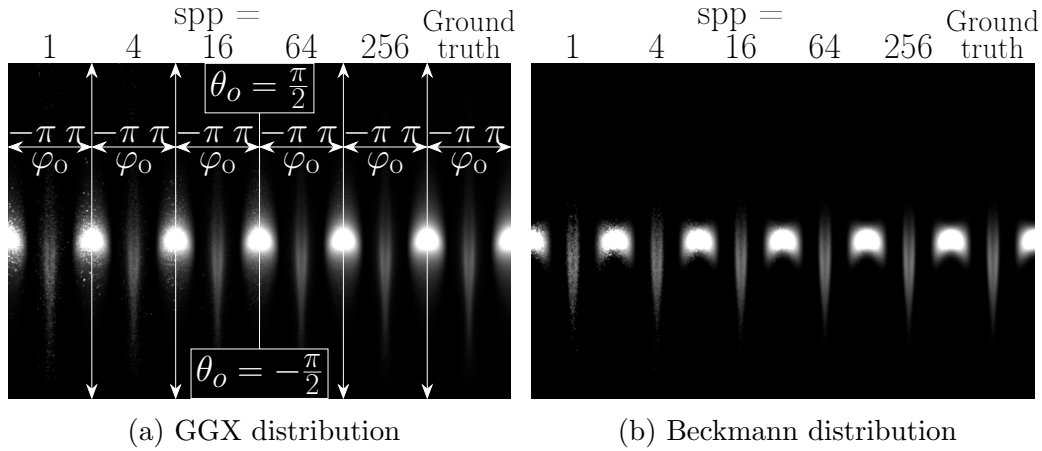


Figure 4.6: Evaluating  $S_{TT} + S_{TRT}$  as a function of  $\theta_o$  and  $\varphi_o$ , with  $\theta_i = \varphi_i = 0, \sigma_a = 0$  and  $\alpha = 4^\circ$ . We test our combined Monte Carlo-Simpson integration method with 1, 4, 16, 64, and 256 samples per pixel. The ground truth is computed with Simpson’s rule applied along  $\varphi_m$  and Lebedev quadrature [71, 16] in  $\omega_r$  and  $\omega_{tr}$ . In both subfigures  $\beta = 0.08$ . In Section 4.4.1 we will explain how such images are produced.

Now Eqs. (4.31) and (4.32) integrate in 1D, we can easily evaluate them using the same composite Simpson’s rule as before.

The above method is significantly faster than using quadrature on all dimensions, and has a reasonably low noise level even when we only sample one internal path for each  $\varphi_m$  every time the BCSDF is evaluated (Fig. 4.6). During render time, the function will be evaluated multiple times and gradually converge. In practice, we do not observe more variance in the method than that of d’Eon et al. [27].

## Probability Distribution Function

Evaluating the PDF is similar to evaluating the BCSDF, we also integrate along the azimuth. After selecting an azimuthal offset, we sample an internal path (when applicable), compute the attenuation  $\mathcal{A}$  of each lobe, and take  $\mathcal{A}/\mathcal{A}_R+\mathcal{A}_{TT}+\mathcal{A}_{TRT}$  as an estimate of the probability of sampling a specific lobe; then for each lobe, we multiply  $\mathcal{A}/\mathcal{A}_R+\mathcal{A}_{TT}+\mathcal{A}_{TRT}$  by the conditional probability of sampling the final outgoing direction, given that we have sampled the internal path (when applicable). To summarize, the probability of sampling

an outgoing direction  $\omega_o$  given incident direction  $\omega_i$  is

$$P_{\omega_i}(\omega_o) \approx \frac{1}{2} \int_{-1}^1 \frac{1}{\mathcal{A}_R + \mathcal{A}_{TT} + \mathcal{A}_{TRT}} \left( \frac{\mathcal{A}_R D_1 G_1(\omega_i)}{4|\omega_i \cdot \omega_{m1}|} \right. \quad (4.33)$$

$$+ \frac{\mathcal{A}_{TT} D_2 G_2(\omega_t) |\omega_t \cdot \omega_{h2}| |\omega_o \cdot \omega_{h2}|}{\eta^2 \|\bar{\omega}_{h2}\|^2 |\omega_t \cdot \omega_{m2}|}$$

$$\left. + \frac{\mathcal{A}_{TRT} D_3 G_3(\omega_{tr}) |\omega_{tr} \cdot \omega_{h3}| |\omega_o \cdot \omega_{h3}|}{\eta^2 \|\bar{\omega}_{h3}\|^2 |\omega_{tr} \cdot \omega_{m3}|} \right) dh,$$

assuming we sample visible normals.

## 4.4 Results and Comparison

In this section, we validate our BCSDF against the ground truth Monte Carlo simulation, and compare both to previous separable [26] and non-separable [28] models. We also show the final rendering results generated using our and the separable model.

### 4.4.1 Validation

Similar to previous non-separable model by d'Eon et al. [28], we run a series of Monte Carlo simulation and compare the results with that computed by Eqs. (4.12), (4.23) and (4.24), as well as the implementation in previous works [26, 28]. For circular cross-section, we keep the azimuthal illumination angle  $\varphi_i$  to be 0, and only vary  $\theta_i$ . In each subfigure in Figs. 4.7 and 4.9 to 4.11,  $S(\omega_i, \omega_o) \cos \theta_i$  is plotted in  $(\theta_o, \varphi_o)$  coordinates. The hair is represented by a rough cylinder made of keratin ( $\eta_{\text{keratin}}/\eta_{\text{air}} \approx 1.548$ ), with microfacet roughness and Smith shadowing. We implement a spherical camera in Mitsuba 2 [87] that looks at the hair at the sphere center from all directions. The emitter is directional with irradiance 1, the developed film has a resolution of  $400 \times 100$ . All images are rendered using the `scalar_spectral` variant on an Apple M1 8-core CPU.

**Monte Carlo simulation.** For each sample on the image pixel, we generate a uniform random offset  $h \in [-1, 1]$  on the hair, and perform path tracing towards the emitter. Scale tilt is simulated by centering the normal distribution around the tilted mesonormal, but keeping the local shading frame unchanged. 1024 *samples per pixel* (spp) are used in Fig. 4.7 for the R lobe, others with TT and TRT lobes have 65536 spp.

**Numerical integration.** For each pixel,  $S(\omega_i, \omega_o) \cos \theta_i$  is evaluated directly via composite Simpson’s rule or combined numerical method as described in Section 4.3.4.

**Analytical integration without shadowing-masking.** There exists an analytical solution for the R lobe with the GGX distribution.  $\frac{R_1}{8 \cos \theta_o} \int D \, d\varphi_{m1}$  is evaluated as described in Appendix E.

**Previous separable model.** We take the implementation of d’Eon et al. [26, 27] with corrected absorption term as stated in Section 4.3.1. Their longitudinal width  $\beta_R$  is not equivalent to our microfacet roughness  $\beta$ ; for comparison, we manually choose a longitudinal width for each microfacet roughness value so that the two deliver approximately the same reflectance of the R lobe at  $\theta_i = 0, \theta_o = 0, \varphi_o = 0, \alpha = 0$ . Such a roughness pair gives almost the same longitudinal span. This choice holds for all such comparisons between our and the separable model [26].

**Previous non-separable model.** In Fig. 4.8, we directly compare with the lat-long images by d’Eon et al. [28]. Their image intensity seems different than ours; therefore, we applied a cosine scaling on our rendered images for a fair comparison, *i.e.*  $S(\omega_i, \omega_o) \cos \theta_i \cos \theta_o$  instead of  $S(\omega_i, \omega_o) \cos \theta_i$ .

## R Lobe of a Circular Cross-Section

Since d’Eon et al.’s model [28] is designed to match Beckmann roughness, we compare the R lobe of the first four aforementioned methods in Fig. 4.7 with GGX roughness and compare with d’Eon et al.’s work [28] separately with Beckmann roughness in Fig. 4.8.

In Fig. 4.7, the numerical solution matches the ground truth Monte Carlo simulation perfectly, even at grazing  $\theta_o$  angles. The analytical solution also reproduces the ground truth accurately, despite being brighter at extreme grazing  $\theta_o$  angles, where  $G$  should have been low. By ignoring  $G$  we omit the energy loss which comes from visibility inside the microsurface.

The most noticeable difference between the three microfacet-based methods and the separable model lies in the focusing and increased brightness at grazing  $\varphi_o$  angles, as predicted in Fig. 4.4. The support of the bright lobe does not touch  $\varphi_o = \pm\pi$  except when  $\theta_i = 0$ . Therefore, we are particularly interested in the behavior as  $\varphi_o$  approaches  $\pm\pi$ .

In this case, assuming no scale tilt for the moment, When  $\varphi_o = \pm\pi$ , the

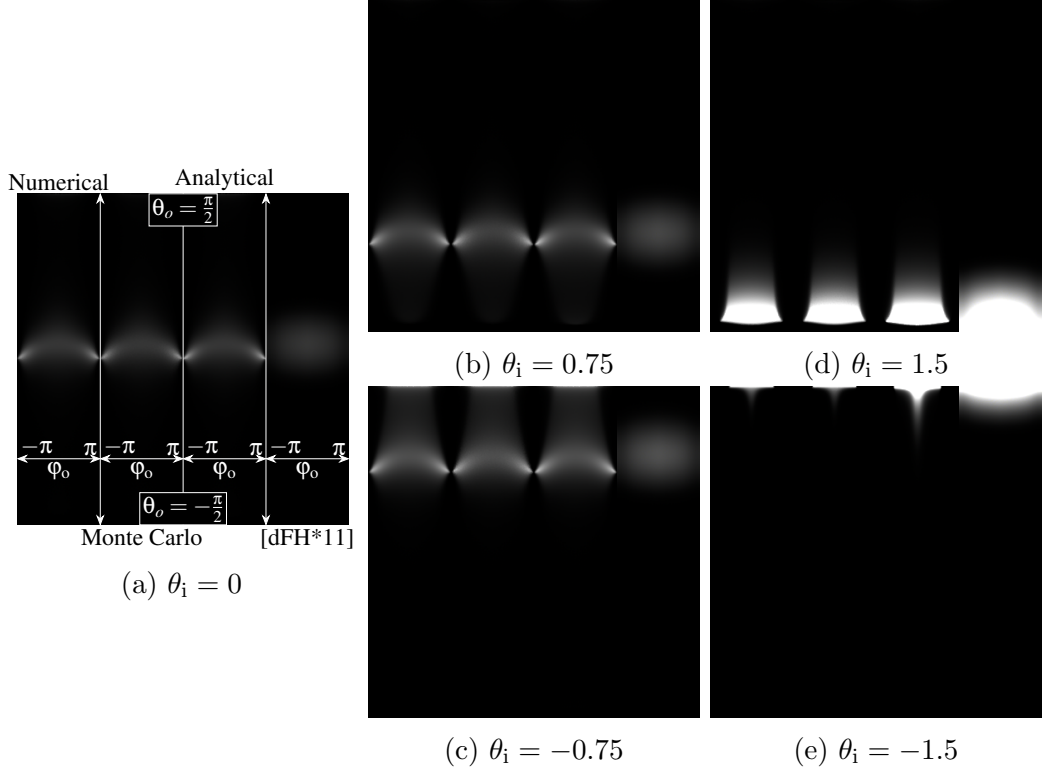


Figure 4.7: Each subfigure compares the R lobe of four different fiber BCS-DFs, under various illumination angles  $\theta_i$ .  $\alpha = 4^\circ$ , GGX  $\beta = 0.08$ ,  $\beta_R = 7.7^\circ$ . Each image is organized in four stripes: **left**: numerical integration of the proposed model, including the shadowing-masking function  $G$ ; **middle left**: ground truth Monte Carlo simulation; **middle right**: analytical integration of the proposed model, excluding  $G$ ; **right**: [26].

incoming, outgoing and micronormal angles are

$$\omega_i = \begin{bmatrix} 0 \\ \sin \theta_i \\ \cos \theta_i \end{bmatrix}, \omega_o = \begin{bmatrix} 0 \\ \sin \theta_o \\ -\cos \theta_o \end{bmatrix}, \omega_h = \begin{bmatrix} \sin \varphi_h \cos \theta_h \\ \sin \theta_h \\ \cos \varphi_h \cos \theta_h \end{bmatrix}, \quad (4.34)$$

respectively.  $\omega_i$  and  $\omega_o$  should be visible from the macronormal

$$\omega_m = [\sin \varphi_m, 0, \cos \varphi_m]^\top, \quad (4.35)$$

therefore,

$$\begin{aligned} \omega_i \cdot \omega_m \geq 0, \omega_o \cdot \omega_m \geq 0 &\Rightarrow \cos \theta_i \cos \varphi_m \geq 0, \cos \theta_o \cos \varphi_m \leq 0 \\ &\Rightarrow \cos \varphi_m = 0 \\ &\Rightarrow \omega_m = [\pm 1, 0, 0]^\top. \end{aligned} \quad (4.36)$$

It also holds that

$$\begin{aligned}\omega_o &= 2(\omega_i \cdot \omega_h)\omega_h - \omega_i \\ &= 2(\omega_i \cdot \omega_h) \begin{bmatrix} \sin \varphi_h \cos \theta_h \\ \sin \theta_h \\ \cos \varphi_h \cos \theta_h \end{bmatrix} - \begin{bmatrix} 0 \\ \sin \theta_i \\ \cos \theta_i \end{bmatrix}.\end{aligned}\quad (4.37)$$

Comparing with the expression of  $\omega_o$  in Eq. (4.34), it must be either  $\sin \varphi_h \cos \theta_h = 0$  or  $(\omega_i \cdot \omega_h) = 0$ . Assuming  $\sin \varphi_h \cos \theta_h = 0$ , then  $\omega_h = [0, \sin \theta_h, \cos \varphi_h \cos \theta_h]^\top$ . From Eq. (4.36) follows that  $\omega_m \cdot \omega_h = 0$ ; in this case, the normal distribution function  $D(\omega_h)$  is extremely low. Therefore,  $\omega_i \cdot \omega_h = 0$  is a more probable situation. From Eq. (4.37) we conclude that

$$\omega_o = -[0, \sin \theta_i, \cos \theta_i]^\top. \quad (4.38)$$

This explains why as  $\varphi_o \rightarrow \pm\pi$ , the reflection is focused on one point, the longitudinal angle of which is  $\theta_o = -\theta_i$ .

However, in the presence of tilted surface scales, the incoming and outgoing angles must also be visible from the mesonormal

$$\omega_{m\alpha} = [\sin \varphi_m \cos \alpha, \sin \alpha, \cos \varphi_m \cos \alpha]^\top, \quad (4.39)$$

therefore

$$\begin{aligned}\omega_i \cdot \omega_{m\alpha} &\geq 0, & \omega_o \cdot \omega_{m\alpha} &\geq 0, & \omega_i \cdot \omega_m &\geq 0, & \omega_o \cdot \omega_m &\geq 0 \\ \Rightarrow \cos \varphi_m &= -\tan \theta_i \tan \alpha = 0.\end{aligned}\quad (4.40)$$

When  $\alpha \neq 0$ , above equation is only satisfied at  $\theta_i = 0$ . Therefore, at oblique  $\theta_i$  angles,  $\varphi_o = \pm\pi$  is unreachable.

We believe that this focusing and increased brightness at both ends is what Khungurn and Marschner [66] described as the *E mode*. According to their measurement and description, the *E mode* “is the brightest around forward directions and is very sharp in the  $\theta_o$  direction”, and it satisfies “ $\theta_o = -\theta_i$ ”; these observations agree well with the appearance in Fig. 4.7 as  $|\varphi_o| \rightarrow \pi$ . Most importantly, this *E mode* is also present in black hairs, indicating that it is caused by reflection. Therefore, we conclude that the *E mode*, instead of being a separate mode, is a component of the R mode as a natural result of surface roughness at grazing angles.

In contrast to our method which is completely microfacet-based, previous separable model [28] applies only a cosine modulation in the longitudinal scattering direction based on the separable method [26]. This approximation matches the Monte Carlo rendering at small inclinations. However, as  $\theta_i$  gets larger, the focusing brightness in the forward scattering direction can not be described by a cosine modulation anymore, whereas our method still matches the Monte Carlo simulation faithfully (Fig. 4.8).

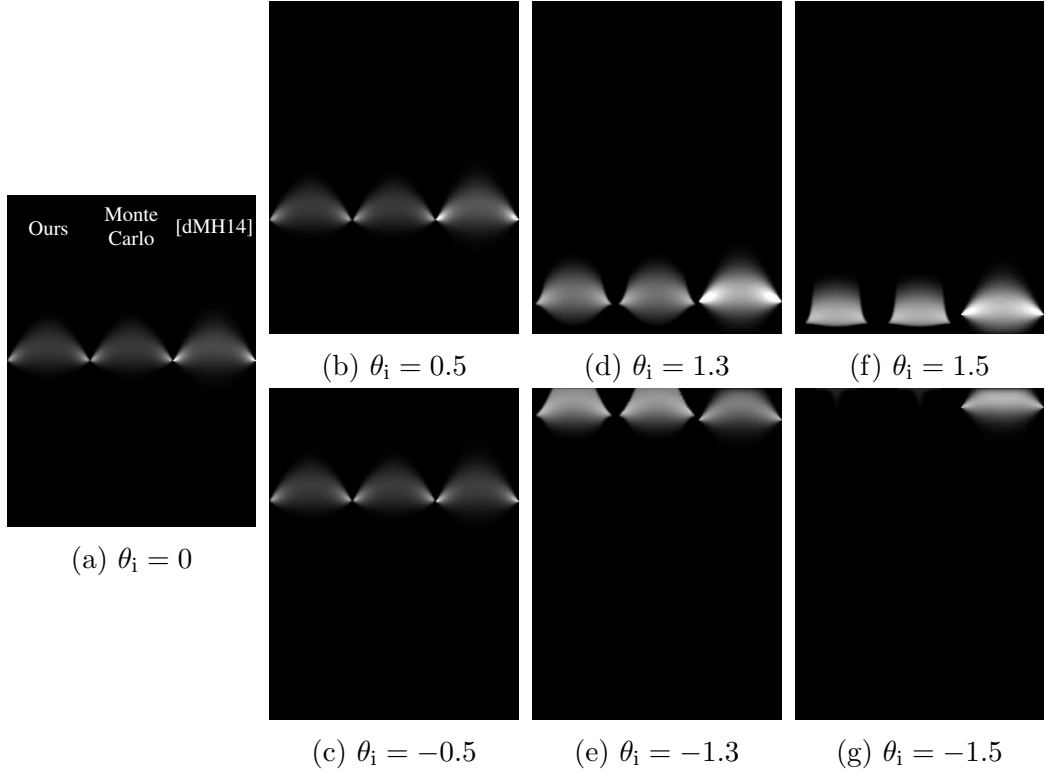


Figure 4.8: Each subfigure compares the R lobe of three different fiber BCS-DFs, under various illumination angles  $\theta_i$ .  $\alpha = 4^\circ$ , Beckmann  $\beta = 0.08$ . Each subfigure is organized in three stripes: **left**: our proposed model with numerical integration; **middle**: ground truth Monte Carlo simulation; **right**: [28].

### TT and TRT Lobes of a Circular Cross-Section

The same comparison as in the previous subsection (without analytical method and non-separable model [28]) is shown in Fig. 4.9. As before, our model matches the Monte Carlo simulation closely.

Despite the similar longitudinal span, our TRT lobe is more concentrated in the azimuth as compared to the separable model; ours is also less shiny at grazing angles. Furthermore, the two methods have similar TT lobes except at grazing angles. However, this similarity with the previous method only holds for Beckmann roughness as we have used in Fig. 4.9. GGX roughness has longer tails in the distribution (Fig. 4.6a) and is hardly comparable with the previous method.

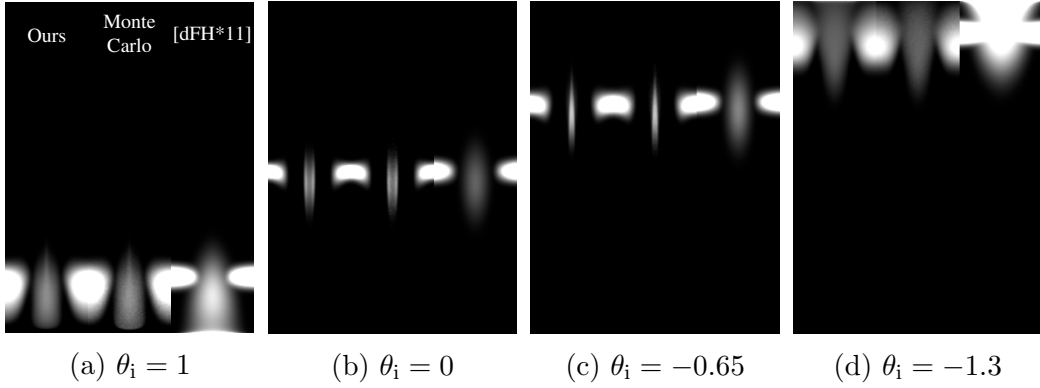


Figure 4.9: TT plus TRT lobe for various illumination angles  $\theta_i$ .  $\alpha = 2^\circ$ ,  $\sigma_a = 0$ , Beckmann  $\beta = 0.05$ ,  $\beta_R = 4.4^\circ$ . In each subfigure, **left**: Our model evaluated using combined numerical integration as described in Section 4.3.4; **middle**: ground truth Monte Carlo simulation, 65536 spp; **right**: [26].

### Scattering from Elliptical Fibers

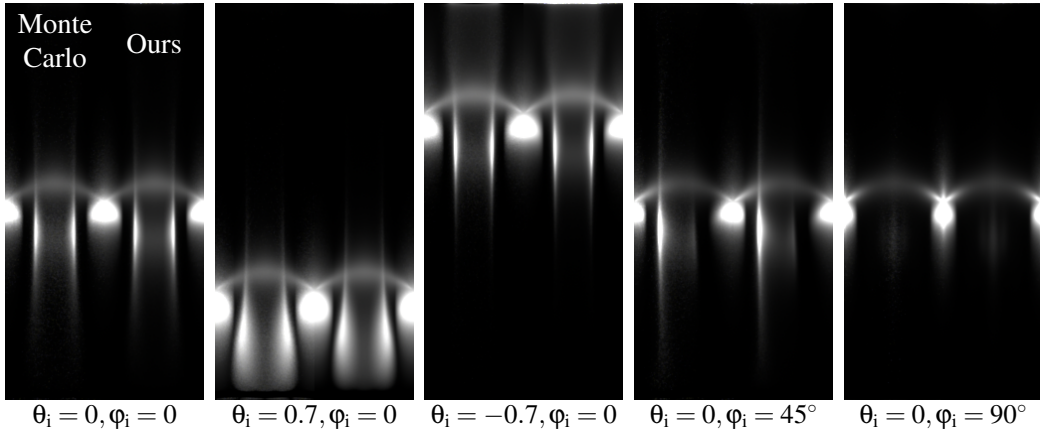


Figure 4.10: Validating our BCSDf of elliptical cross-section against Monte Carlo simulation, under various illumination angles.  $\alpha = 4^\circ$ ,  $\sigma_a = 0$ ,  $\beta = 0.05$ , ellipse eccentricity  $e = 0.8$ . For each of the five pairs: **left**: Monte Carlo simulation of scattering from an elliptic cylinder. **right**: our BCSDf for elliptical cross-section.

We verify our BCSDf against Monte Carlo simulation in Fig. 4.10, as we did for the cylindrical fibers. Here, our model also agrees well with the ground truth. The small discrepancy at grazing angles for  $\theta_i = 0.7$  might be because that the macro/mesonormal in the Monte Carlo simulation and our theoretical model don't always agree, as mentioned in Section 4.3.2.

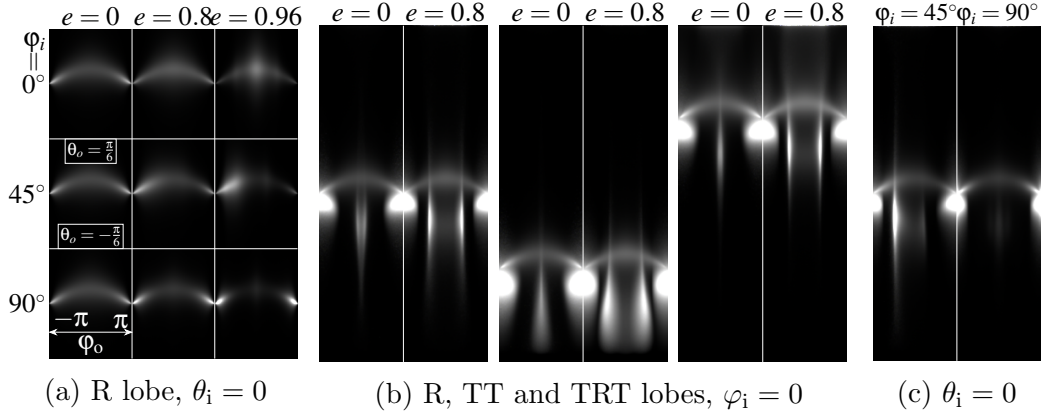


Figure 4.11: Comparing fiber scattering function of circular and elliptical cross-sections.  $\alpha = 4^\circ, \sigma_a = 0, \beta = 0.05$ . (a) R lobe of fibers with various illumination angles in  $\varphi_i$  and different eccentricity  $e$ . (b) R, TT and TRT lobes of circular and elliptical fibers with various illumination angles in  $\theta_i$ . **Left:**  $\theta_i = 0$ . **middle:**  $\theta_i = 0.7$ . **right:**  $\theta_i = -0.7$ . (c) R, TT and TRT lobes of a fiber with elliptical cross-section ( $e = 0.8$ ) under oblique illumination angles in  $\varphi_i$ .

We also show the effect of elliptical cross-sections with varying eccentricity on the cosine scaled BCSDf in Fig. 4.11.

The first column in Fig. 4.11a shows the R lobe for a circular fiber under various illumination angles in  $\varphi_i$ . As expected, the function is invariant to  $\varphi_i$  due to rotational symmetry. The last column in Fig. 4.11a shows the R lobe for an elliptical fiber with eccentricity  $e = 0.96$ . Such an elliptical fiber has a higher value of the *normal distribution function* (NDF) near the  $z$  axis than near the  $x$  axis (Fig. 4.5); thus, when the illumination is along the negative  $z$  axis ( $\varphi_i = 0^\circ$ ), the reflectance is higher at  $\varphi_o = 0$ , and lower in the forward scattering direction, compared to a circular fiber. When the illumination is along the negative  $x$  axis ( $\varphi_i = 90^\circ$ ), although the NDF is the smallest in the backward scattering direction, the diameter is also the smallest, thus, a locally maximal reflectance is visible at  $\varphi_o = 0$ . The highest value of the NDF along the  $z$  axis and the smallest projected area along the  $x$  axis lead to a global maximum in reflectance along the forward scattering function. When  $\varphi_i = 45^\circ$ , the reflectance has a highest value at around  $\varphi_o = -90^\circ$ .

An eccentricity of 0.96 is mainly for the purpose of illustrating the above properties. According to Khungurn and Marschner [66], a hair fiber has an eccentricity of up to 0.8, which is demonstrated in the middle column of Fig. 4.11a. There, the above-mentioned properties still hold, but are less significant, especially when compared to the influence of eccentricity on the

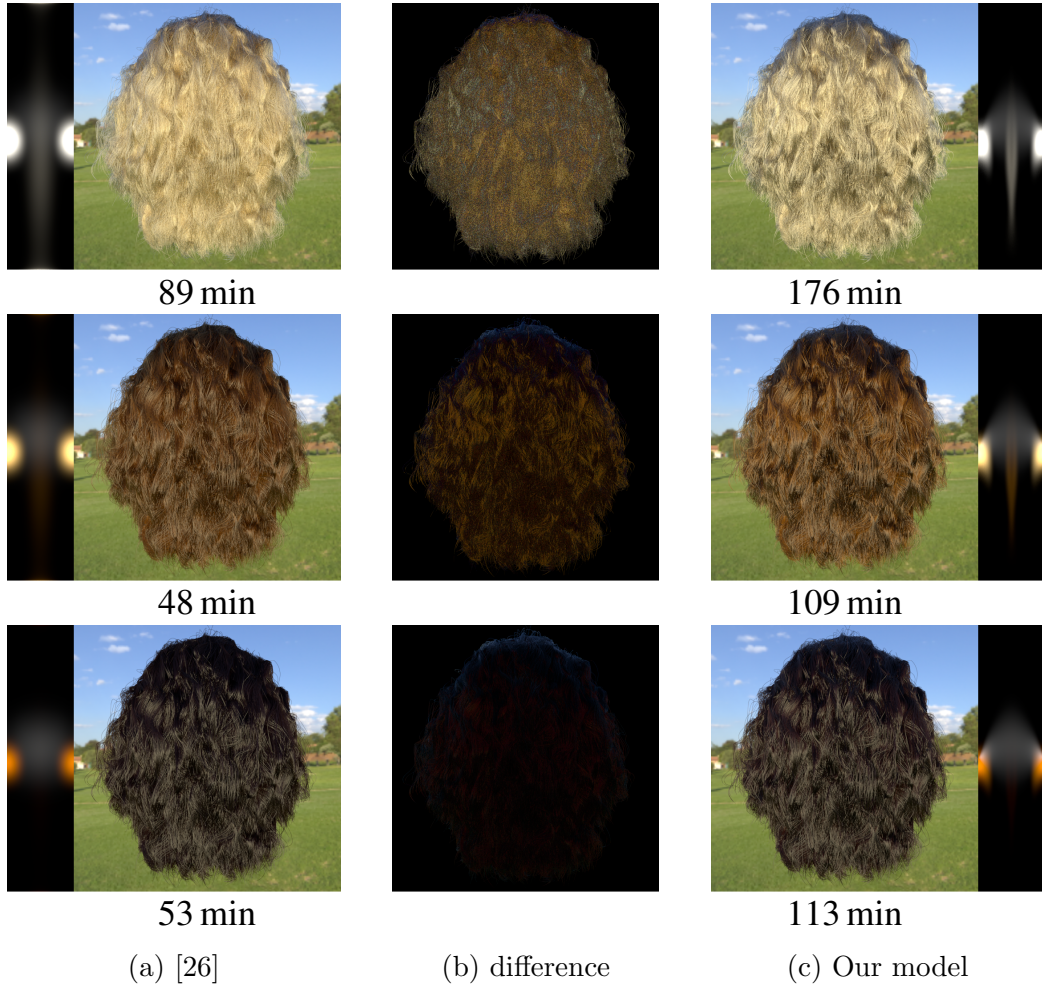


Figure 4.12: The Park Scene with increasing melanin concentration from top to bottom.  $\alpha = -4^\circ$ . (a) Marschner model with  $\beta_R = 11^\circ$ . (c) our model with Beckmann roughness  $\beta = 0.135$ . (b) the difference between the images on the left and the right side. The exposure value of the accompanying BCSDf visualization is increased by 1 to make the R lobe better visible.

TRT component in Figs. 4.11b and 4.11c. There exist two symmetric extrema for the TRT lobe [76]. However, for a fiber with an elliptical cross-section, these two extrema are further separated from each other, as is shown in Fig. 4.11b, left. At oblique  $\theta_i$  angles (Fig. 4.11b middle and right pairs), the two extrema of a circular fiber are almost indistinguishable, whereas for an elliptical fiber they are still clearly separated from each other. They also appear to be much brighter than that of a circular fiber. When  $\varphi_i = 45^\circ$  (Fig. 4.11c), the extremum on the left is much brighter than the extremum

on the right, similar to what we have discussed before for the R lobe in Fig. 4.11a. When  $\varphi_i = 90^\circ$ , the two extrema seem to be merging into one, and the intensity is also much lower, since total internal reflection is less pronounced.

## 4.4.2 Rendering Hair Scenes

In this subsection, we render a set of hair scenes to compare our method with the separable model, as well as demonstrate the influence of the absorption and the roughness parameter. The hair and the woman model is taken from Yuksel’s website [143]. For hair with elliptical cross-sections, the semi-minor axis is aligned with the curvature vector.

### Circular Cross-Sections

**Frontlit.** Fig. 4.12 shows the park scene with strong sunlight right behind the camera. The images are rendered in  $600 \times 600$  resolution with 1024 spp, accompanied by visualizations of the corresponding BCSDF with  $\theta_i = 0$ , and the difference images.

One prominent difference between our and the previous separable model lies in the specular highlight at the top of the head. Dark hairs rendered with the Marschner model are almost completely black at the top, whereas ours show more realistic specular highlight at such grazing angles. Another difference is that the Marschner model has broader TRT lobes in the azimuth, causing the same energy to spread in a larger angle; as a result, their model looks more saturated, while ours show higher contrast. Our hair has a few darker regions in the hair due to occluded highlights, while Marschner’s model spreads the reflectance more uniformly around the occluding fibers. This property is clearly visible in the blond hair. All in all, we found that hair rendered using the Marschner model appears flatter.

**Backlit.** To demonstrate the glints of the R lobe in the forward scattering direction, we render a studio scene with a small but strong area light source in front of a woman’s head (Figs. 4.1 and 4.13).

With the previous method, the forward scattering is dominated by the TT lobe. The R lobe has only very dim response, causing the hair to look brown everywhere. With our method, there is a strong highlight due to the R lobe. Such variation in intensity gives the hair more sense of depth.

**Roughness.** Rougher hairs appear softer (Fig. 4.14), and take less time to render because of our roughness-dependent integration step size. From



(a) [26], 15 min

(b) GGX, 22 min

(c) Beckmann, 28 min

Figure 4.13: Backlit on dark hair modeled by previous method and our method, with either Beckmann or GGX roughness. Our method (b,c) produces more realistic images due to the focused forward scattering of the R lobe. All images are rendered with 256 spp.  $\alpha = 4^\circ, \beta = 0.15, \beta_R = 12^\circ$ .

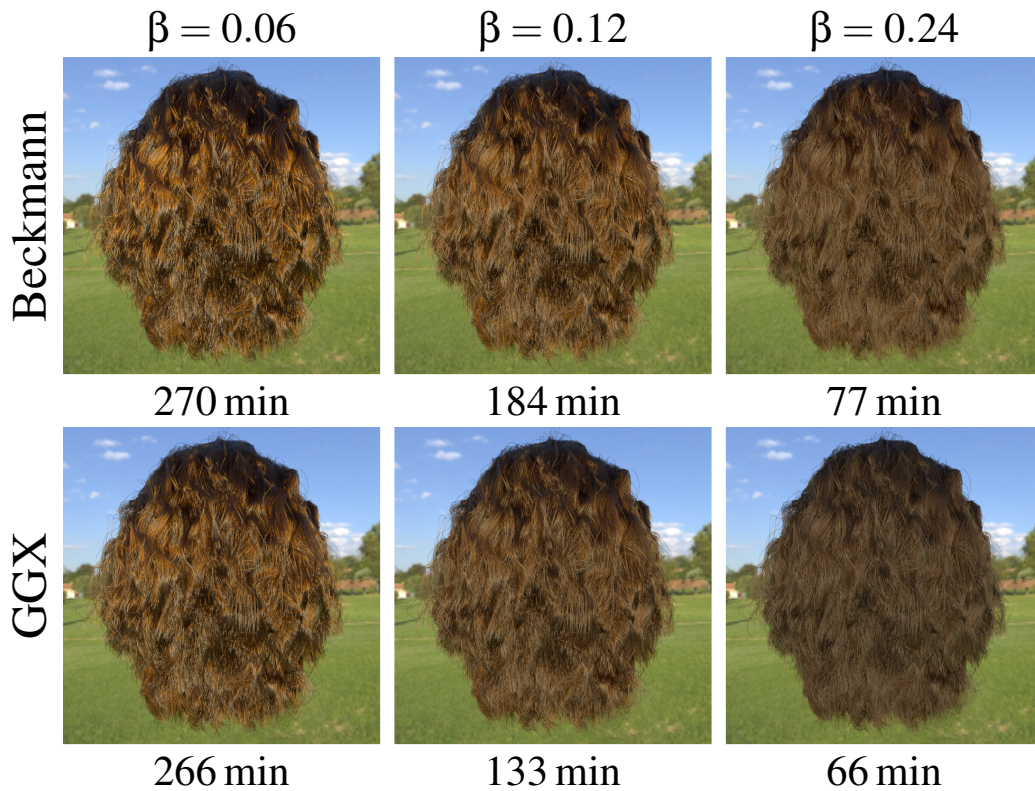


Figure 4.14: Hair with various roughness. All images are rendered in  $600 \times 600$  resolution with 1024 spp.  $\alpha = 3^\circ$ .

Fig. 4.6 we know that GGX has longer tails in the longitudinal direction; the images therefore also appear softer than those produced by the same Beckmann roughness. A Beckmann roughness of 0.06 to 0.24 is comparable with a Marschner longitudinal width of about  $5^\circ$  to  $19^\circ$ .

### Elliptical Cross-Sections

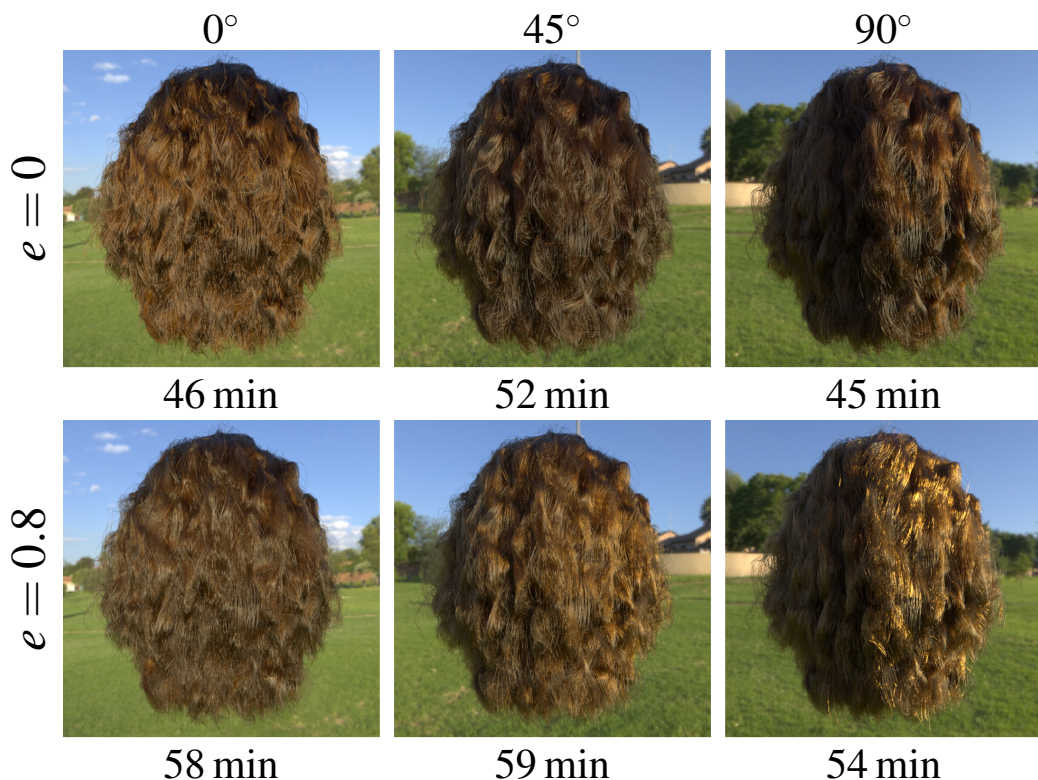


Figure 4.15: Circular and elliptical hair under various illumination angles. **Left:** illumination angle perpendicular to the camera plane; **middle:** illumination angle  $45^\circ$  to the camera plane; **right:** illumination angle parallel to the camera plane. Images rendered in  $600 \times 600$  resolution with 1024 spp.  $\alpha = 3^\circ$ , Beckmann  $\beta = 0.135$ .

All the renderings in this section are without the PDF computation.

As shown in Fig. 4.15, the highlight positions from circular and elliptical cross-sections differ significantly. When the illumination angle is perpendicular to the camera plane, the TRT component of the circular cross-section is strong, the hair therefore appears bright; for elliptical cross-sections, however, the TRT component is stronger at oblique illumination angles.

## 4.5 Discussion and Limitation

**Performance.** All the rendered images in Section 5.5 are annotated with rendering time. As both our and the previous method integrate along the azimuth, we have hoped for a similar rendering time. However, ours are about  $1.2 \sim 5\times$  slower than the previous method. We found out that 60% of the rendering time is spent on computing the PDF, since the PDF is evaluated both for emitter and BSDF sampling using the `path` integrator in Mitsuba 2. This computation time could almost completely be removed by using a cheap approximation of the PDF as a proxy for the weight computation in multiple importance sampling, as is common practice for complex material models. Indeed, as we have dropped the PDF computation completely in Fig. 4.15, our method shows comparable performance to the previous method. Rendering elliptical cross-sections takes longer than circular cross-sections because of the extra computation of arc lengths.

Sampling microfacets inside the integration is also expensive:  $1/3$  of the total rendering time is spent on sampling microfacets. The numerical evaluation of the R lobe, where no microfacet sampling is performed, takes only 8% of the BCSDf evaluation time.

Since we adjust the integration step size according to the roughness, the rendering time also depends on the roughness. As can be seen in Fig. 4.14, rough hair has comparable rendering time as previous work [27]. Production rendering systems would often use a kind of regularization for indirect lighting and use rougher variants of the materials for higher-order scattering. This approach will directly profit from those performance gains.

**Energy loss.** Our model is based on the assumption that lobes beyond TRT can be ignored due to the little energy they carry. We therefore evaluate the energy loss resulting from this simplification using Monte Carlo simulation.

In the first row of Fig. 4.16, we show the BCSDf slices of tracing only the first three lobes (R, TT, TRT), tracing lobes beyond the first three, and tracing infinite lobes with zero internal absorption, respectively; in the second row, we show only the lobes beyond the first three with increasing absorption, the same as used in the renderings in Fig. 4.12.

Fig. 4.16 shows that lobes beyond TRT are only dimly visible with low internal absorption (blond hair), especially at grazing incident angles. The TRRT lobe still has characteristic shapes, and can be added to the model similarly as described in Section 3, if necessary. Lobes beyond TRRT are very weak and have only low-frequency features; if energy conservation is desired, this contribution can be approximated using a single lobe following

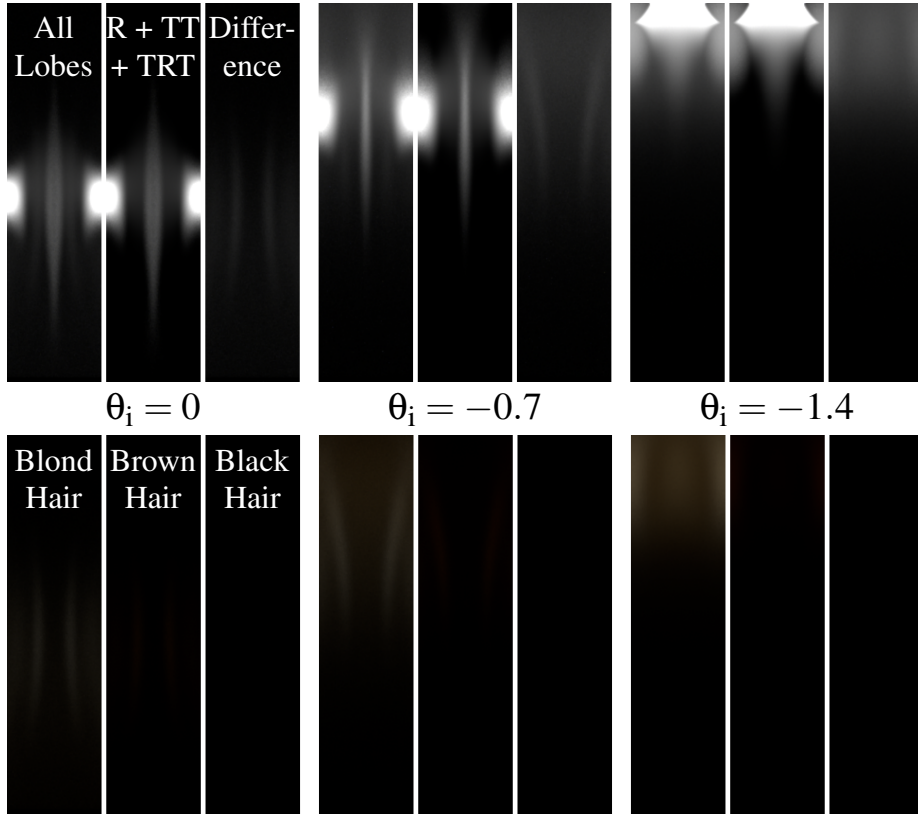


Figure 4.16: Evaluating higher-order lobes for various internal absorption under different incident angles in  $\theta_i$  using Monte Carlo simulation.  $\alpha = 2^\circ$ , Beckmann  $\beta = 0.15$ ,  $e = 0$ . **First row:**  $\sigma_\alpha = 0$ ; for blond, brown, and black hair, the eumelanin and pheomelanin concentrations  $\rho = 0.06, 0.6$ , and  $1.8$ , respectively.

Chiang et al. [19]. For brown and black hair, the contribution of higher-order lobes is negligible.

**Far-field model.** We have proposed a far-field scattering model that requires expensive integration along the azimuth; this integration can potentially be skipped to enable near-field scattering [19].

**Wave-optics effect.** Our model is a pure geometry one and ignores the wave-optics effect. However, the mean diameter of human hair is  $80 \mu\text{m}$  [24], at which scale diffraction is present. It would be interesting to trace complex rays with our method, similar to Benamira and Pattanaik's method [11].

## 4.6 Conclusion and Future Work

In this chapter, we present the first microfacet-based hair scattering model. Instead of separating the scattering function in the outgoing direction without physical justification, we model the roughness as a distribution of micronormals and derive a fiber BSDF following well-established microfacet theory. The importance sampling procedure is naturally composed of sampling microfacets. We verify that our R lobe can model the narrow and bright reflectance in the forward scattering direction as observed in previous works. Our R lobe is efficient to evaluate and can find its application in any kind of fibers, including furs with complicated internal scattering. The TT and TRT lobes are restricted to homogeneous materials and are slower to evaluate than the previous model due to the high dimensional integration; we are looking forward to a more efficient evaluation method, for example dynamically adjusted subtler for numerical integration, skipping azimuthal roughness completely so that no integration is needed, or a new microfacet distribution for which an analytical solution exists. We also demonstrate scattering from elliptical fibers and argue that the model can be extended to any smooth convex shape, which finds its application in fibers with irregular cross-sections [1].

With this work, we wish to provide a new look at the hair scattering model in a physically based way.



# 5. Rendering Iridescent Rock Dove Neck Feathers

The content of this chapter has been published as:

Weizhen Huang, Sebastian Merzbach, Clara Callenberg, Doekele Stavenga, and Matthias Hullin. Rendering iridescent rock dove neck feathers. In *ACM SIGGRAPH 2022 Conference Proceedings*, pages 1–8, 2022. DOI: 10.1145/3528233.3530749

## Summary

Abundant research has been dedicated to human hair or animal fur rendering models, while there is a lack of works focusing on feather rendering. As a result, CG artists often use hair shaders to model bird feathers. However, feathers interact with light completely differently than hairs or furs. Although they may appear similar at a macroscale, closer observation under a microscope reveals significant differences. Unlike cylindrical hair strands, bird feathers possess cascaded structures, with the hair-like structures known as barbs, which branch out on both sides and form barbules with irregular cross-sections. Currently, there is a lack of a proper shading model to describe these cascaded structures, the only exception being a recent work from Baron et al. [6]. However, they still rely on a hair scattering model, which fails to consider the irregular cross-section of barbules.

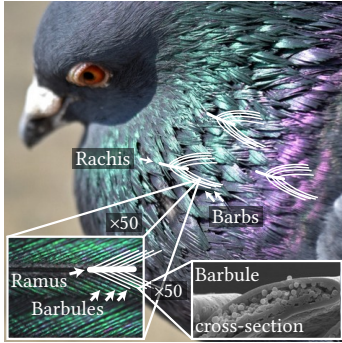
In this chapter, we propose a novel approach to render the iridescent rock dove neck feathers. Our method involves modeling the geometry of the barb and statistically describing the scattering behavior of the substructures, since structures smaller than a barb are typically not visible to the naked eye. With the help of a microscope, we observe that barbules are composed of repeating saddle-like structures, which we refer to as unit barbule cells. We model the interaction between light and a barbule unit cell using the Cook-Torrance microfacet model, with a suitable normal distribution describing the shape of the microarea, which is approximated by an elliptical arc in the

azimuthal direction and a circular arc in the longitudinal direction. Additional terms are included to account for reduced visibility due to overlapping of adjacent barbules. Furthermore, the prominent two-color iridescence of rock dove neck feather barbules is caused by the thin keratin layer on the surface, which we model as thin film reflection instead of the typical Fresnel reflection in microfacet models. The background reflection resulting from melanin granules beneath the keratin layer is modeled as a diffuse component. Additionally, the barbules exhibit a certain degree of randomness in terms of thickness, shape, orientation and distance. To address this, we incorporate the randomness into a texture that is loaded alongside the barb geometry.

To validate our model, we employ a specialized optical device developed by Stavenga et al. [110] to capture the hemispherical reflectance of barbule samples, acquired from the biology department at the University of Groningen. Our rendered results demonstrate a close match compared with the measurements: in the azimuthal direction, the barbule has a wider angular span but smaller normal distribution function (NDF) values, resulting in a longer tail with lower intensity; the widespread background component caused by melanin, the color shifting due to change in illumination or viewing direction, and the randomness in barbule orientations are also successfully reproduced by our model. In terms of performance, the render time is twice as long as that of a plain iridescent shader.

Despite being the first model aimed at feather scattering, our model only covers iridescent neck feathers of rock doves. Similar feather structures can be found in other bird species such as hummingbirds and peacocks, and our model can be extended to accommodate these species by adjusting the NDF and the model for color mechanisms. However, some bird species exhibit iridescence in ramus instead of barbules, and some bird species are less iridescent, necessitating separate models for these cases.

**Author Contribution:** I proposed the research topic and conducted a comprehensive literature review. Furthermore, I also modeled the complete feather geometry and designed the rendering model, which I implemented in Mitsuba. In addition, I designed the measurements required for the research, while Doekele Stavenga performed the actual measurements. Sebastian Merzbach contributed to the literature review section in the paper and captured photographs of bird feathers. All co-authors participated in revising the paper and offering valuable insights.



(a) Appearance and structure of rock dove feathers



(b) Full feather rendering

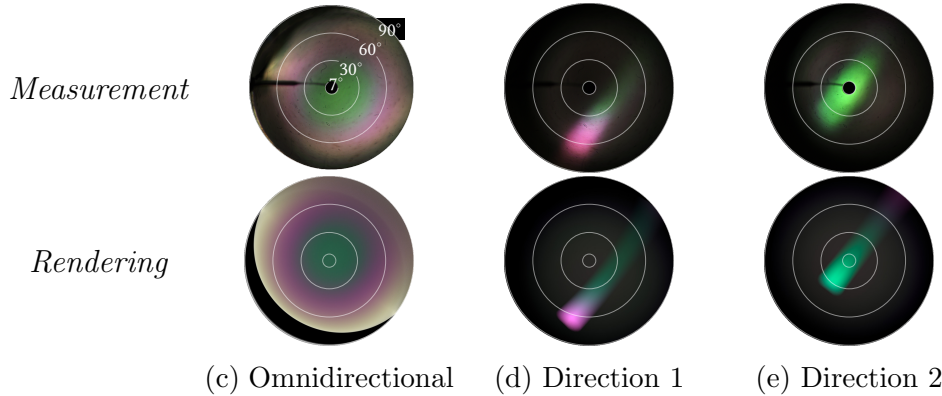


Figure 5.1: (a) The neck feather of the rock dove features geometric structures across a wide range of scales. (c–e) Barbules exhibit a characteristic scattering behavior due to their intricate surface and interior structure. (b) Our model covers details like milliscale roughness, thin films or mutual shadowing between barbules, and closely recreates the appearance of the feather.

## Abstract

Bird feathers exhibit fascinating reflectance, which is governed by fiber-like structures. Unlike hair and fur, the feather geometric structures follow intricate hierarchical patterns that span many orders of magnitude in scale. At the smallest scales, fiber elements have strongly non-cylindrical cross-sections and are often complemented by regular nanostructures, causing rich structural color. Therefore, past attempts to render feathers using fiber- or texture-based appearance models missed characteristic aspects of the visual appearance. We introduce a new feather modeling and rendering framework, which abstracts the microscopic geometry and reflectance into a microfacet-

like BSDF. The R, TRT and T lobes, also known from hair and fur, here account for specular reflection off the cortex, diffuse reflection off the medulla, and transmission due to barbule spacing, respectively. Our BSDF, which does not require precomputation or storage, can be efficiently importance-sampled and readily integrated into rendering pipelines that represent feather geometry down to the barb level. We verify our approach using a BSDF-capturing setup for small biological structures, as well as against calibrated photographs of rock dove neck feathers.

## 5.1 Introduction

The creation of realistic humans and animals has always been a central challenge in computer graphics. An important factor is the rendering of hair and fur, for which various models exist [76, 149, 136, 26, 66]. A related but much less studied problem is the rendering of bird feathers [18, 36], even though birds have played pivotal roles in famous animation works like ‘For the Birds’, ‘Piper’ (Pixar) or ‘Rio’ (Disney). Hair and fur models can only partly be transferred to feathers, due to the more complex structure of the latter.

This work explores the rendering of the iridescent neck feathers of one of the most well-known and representative urban bird species, the rock dove (Fig. 5.1a). The feathers show a prominent green-purple shading, which arises from thin-film interference in the feather substructure [142]. Supported by spectrally and angularly resolved measurements, we develop a comprehensive model for the accurate rendering of feathers that takes into account features across various scales (Table 5.1).

Our main contributions are the following:

- We propose a parameterized *bidirectional scattering distribution function* (BSDF) for feathers, which encapsulates the statistics of microscale structures (barbule). It is completely evaluated and importance-sampled at render time.
- we apply the BSDF at milliscale (barb) by changing the local shading frame, providing rich details without having to model the microstructures explicitly.

Table 5.1: The four characteristic scales of our model.

Name	Scale	Feature
Macro	>20 mm	Feather
Milli	0.3 mm	Barb
Micro	40 $\mu$ m	Barbule
Nano	550 nm	Thin film

- We incorporate iridescence in the model, alleviating the need to mix hair and iridescence shaders.
- We validate our model using one-to-one comparisons between measured and rendered BSDF as well as photographs.

## 5.2 Related Work

We briefly review existing models for feather geometry and appearance, as well as previous work on reflectance measurement.

**Geometry** Similar to hair geometry modeling, the majority of works model feathers as assemblies of parametric primitives, usually Bézier curves [18, 35, 116] or NURBS [4]. Latest works [4, 7] derive a procedural feather geometry representation of curve primitives automatically from photos.

Triangulated representations are often used for texturing: Franco and Walter [36] generate an auxiliary mesh from the Bézier representation of their earlier work [35] to transfer results from a pigmentation simulation back to the barb curves. Similarly, Seddon et al. [105] deform a Bézier patch from a scanned feather. A shader generates barb curves along the patch, which can be controlled by bio-inspired attributes painted on the patch.

Our model is based on barb curves with associated normal vector at each vertices, representing the local barbule orientation. To our knowledge, Baron et al.’s works [5, 6] are the only ones also adapting the shading frame between barb and barbule.

**Rendering** When rendering feathers in larger scales, *bidirectional texture function* (BTF) are often used without looking into its substructures [36, 18]. For more geometric detail, hair models [76, 26] are alternatively applied to barbs [44, 70], ignoring finer structures such as barbules. However, according to Harvey et al. [47], the feathers’ milliscale features also contribute to optical scattering. Recently, Baron et al. [5, 6] demonstrate a new rendering technique that take into account milliscale features by procedurally rendering the substructures while still applying hair shading models.

None of the above works deal with iridescence. Iridescence in bird feathers is well understood by the ornithology community; however, their simulation is mostly restricted to nanoscales with basic approaches such as thin-film interference simulation [89] and finite-difference time-domain modeling [130]. Only one heavy ray-tracing simulation on feather barbules [77] is performed

with a commercial tool for optical system prototyping FRED [46]. These methods are not well suited for integration in a renderer.

We instead propose a feather-specific BSDF, which models the barbule reflectance statistically.

**Measurements** There are mainly two approaches to acquire BxDFs. Some previous works [5, 67, 18] adopt an image-based acquisition approach, matching the simulation with a few photographs; other works [138, 66] use a gonioreflectometer with motorized robotic arms, alternatively. The reflectance can be sampled at high angular resolution, moving either the light source or the sensor. In particular, Harvey et al. [47] take multiple photographs of a complete feather using a spherical gantry; these photos are then fused to visualize the BRDF.

Our image-based approach uses the setup by Stavenga et al. [110]. It is closely related to the setups in some previous works in computer graphics [41, 66] regarding the application of a non-planar reflector. Our setup allows direct and efficient BSDF acquisition with a digital camera, and is especially suitable for measuring microscale features such as feather barbules and insect wing scales.

## 5.3 Background

This section provides an introduction of the feather geometry, the mechanisms behind the color production and the measurement setting for the BSDF. Table 5.2 lists an overview of the symbols.

### 5.3.1 Feather Geometry

A bird feather is a multi-scale structure (Fig. 5.1a). The hair-like structures that are normally seen with bare eyes are barbs that branch from the rachis. A barb, in turn, has numerous side branches: the barbules, which overlap and together form a rather flat surface. The barbule has a distinctly non-cylindrical cross-section and may, depending on species, comprise thin film coatings, multilayer stacks or photonic crystals (Fig. 5.2). In this chapter, we investigate rock dove neck feathers (Fig. 5.2c), which exhibit thin film structure.

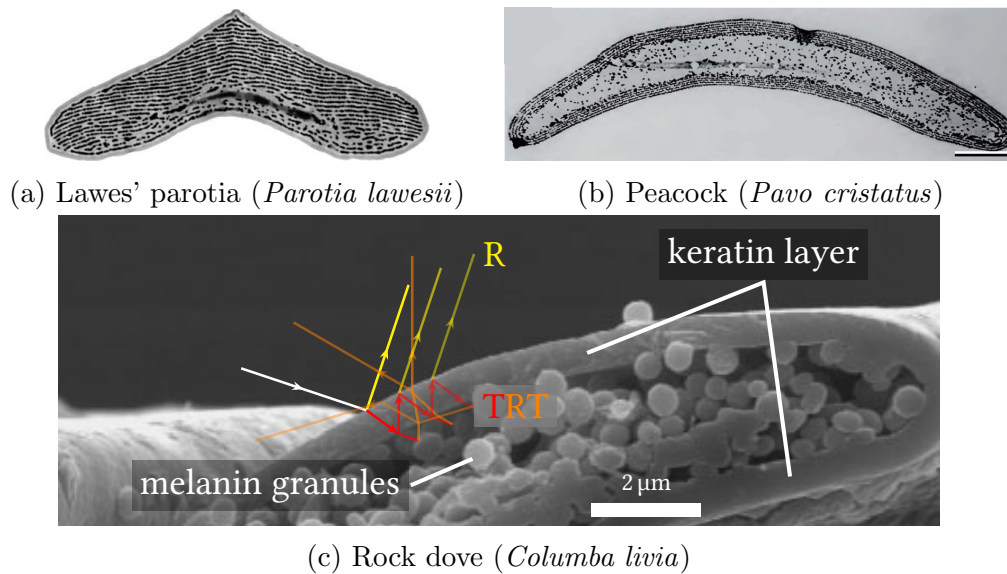


Figure 5.2: Various mechanisms of structural color in barbules. (a) *Transmission electron microscopic* (TEM) image of a male Lawes' parotia breast feather barbule, showing multilayer structure [111]. (b) TEM image of the transverse cross-section of a peacock tail feather barbule, showing 2D photonic crystal structure [37]. (c) *Scanning electron microscopic* (SEM) image of the transverse cross-section of a rock dove neck feather barbule with thin-film structure [81] (©2008 The Physical Society of Japan), overlaid with annotations demonstrating the R and TRT components (Section 5.3.3).

### 5.3.2 The Colors of Bird Feathers

Mainly two mechanisms contribute to the color of birds: pigments and structures [115]. *Pigmentary colors* originate from pigments that absorb light in selective wavelength ranges. A virtually universal pigment in bird feathers, absorbing in a very broad wavelength range, is melanin, which also exists in human hairs. *Structural colors*, on the other hand, originate from regular organized micro- and nanostructures of keratin and melanosomes, reflecting light in restricted wavelength ranges. Structural colors are generally directional and more brilliant than pigmentary colors. Many birds combine pigmentary and structural coloration.

**Rock Dove Neck Feather Barbule Colors** Rock dove neck feather barbules (Fig. 5.2c) exhibit a special two-color iridescence caused by thin-film interference from the upper keratin layer [142, 81, 89]. The feathers located on the upper part of the neck have an average keratin thickness of

595 nm [141] and look green at normal incidence. With only slight variation of the illumination or viewing angle though, the color can very suddenly change from green to purple; the purple feathers on the lower part of the neck, with a mean keratin thickness of 530 nm, turn green at an oblique angle. This angle-dependence of color is demonstrated in Fig. 5.3. Below the

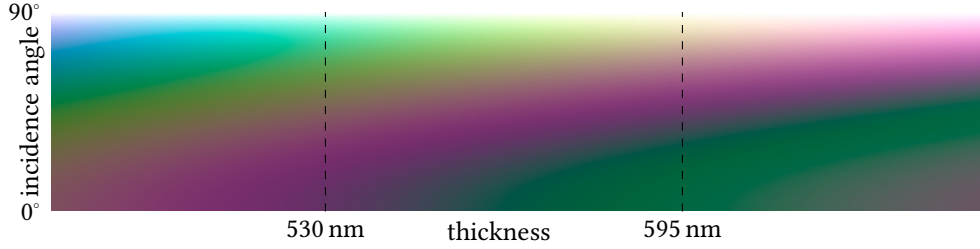


Figure 5.3: Simulated colors of a thin keratin film in air as a function of thickness and incidence angle (illuminant D65).

keratin layer, the barbules feature randomly arranged melanin granules, with minor and almost constant reflectance in the visible wavelength range. They mainly decrease the color saturation.

### 5.3.3 The Physics of Thin Films

Thin-film interference occurs when light is reflected from the upper and lower boundary of the film, causing difference in optical paths (Fig. 5.4). The path difference  $\mathcal{D}$  results in a phase shift  $\Delta\psi = \frac{2\pi\mathcal{D}}{\lambda}$  of the light, with  $\lambda$  being the wavelength. We denote  $r_{ak}$  ( $t_{ak}$ ) as the Fresnel reflection (transmission) coefficient at the air-keratin interface and  $r_{ka}$  ( $t_{ka}$ ) as that at the keratin-air interface (Fig. 5.4 left), and derive the complex thin-film reflection/transmission coefficients  $r$  and  $t$  via Airy formula [140, 10]

$$r = r_{ak} + \frac{t_{ak}r_{ka}t_{ka}e^{i\Delta\psi}}{1 - r_{ka}^2e^{i\Delta\psi}}, \quad t = \frac{t_{ak}t_{ka}}{1 - r_{ka}^2e^{i\Delta\psi}}, \quad (5.1)$$

where  $\Delta\psi = \frac{2\pi\mathcal{D}}{\lambda} = \frac{4\pi d\eta_k \cos\beta}{\lambda}$  holds for both reflection and transmission, with the *index of refraction* (IOR) of keratin  $\eta_k$  and the film thickness  $d$ . The intensity reflectance is then given by

$$I_R = |r|^2. \quad (5.2)$$

We call this reflection the *R component*.

We measure the reflectance spectra of a  $10 \times 10 \mu\text{m}^2$  spot from normal incidence with a *microspectrophotometer* (MSP) [124]. Fig. 5.5 shows the the

Table 5.2: Important notations used in this work

Symbol	Definition
$\eta$	<b>Index Of Refraction</b>
$\lambda$	Wavelength
$I_{R,TRT}$	Reflectance, similar to Fresnel term, Eqs. (5.2) and (5.3)
$L_{i,o}(\omega_{i,o}, \lambda)$	Incoming / outgoing spectral radiance
$S(\omega_i, \omega_o, \lambda)$	<b>Bidirectional Scattering Distribution Function</b>
$\omega_{i,o}$	Incoming / outgoing unit vectors
$\omega_m$	Barbule normal vector, Fig. 5.7b
$\vec{n}$	Barb plane normal vector, Fig. 5.8
$\theta/\phi$	Longitudinal/azimuthal parameterization of $\omega$ , Fig. 5.7b
$\phi_{0,1}$	Lower ( $\phi_0$ ) and upper ( $\phi_1$ ) bound of the azimuth
$b$	Ellipse semi-minor axis, Fig. 5.7b
$r_\theta$	Radius of the longitudinal circular arc, Fig. 5.7b
$\theta_d$	Circular arc opening angle, Section 5.4.1, Fig. 5.7b
$D, D_\theta, D_\phi$	<b>Normal Distribution Function</b> , Section 5.4.1
$G(\omega_i, \omega_m, \omega_o)$	Masking and shadowing term, Section 5.4.1
$H$	Barbule spacing, Fig. 5.8
$\Delta h(\phi), \Delta h'(\phi)$	Projected length of elliptical arc, Fig. 5.8
$h, l$	Azimuthal / longitudinal offset, Fig. 5.9

observed wavelength-dependent reflectance and the simulated R component. Evidently, this component alone cannot sufficiently describe the barbule reflectance behavior, as total destructive interference appears at some wavelengths. There is clearly a background component, which is resulted from the light transmitted through the keratin layer, reflected on the melanin layer, then transmitted back through the keratin layer. We call this the *TRT component*, it is illustrated in Fig. 5.4 (right), and is similarly computed as

$$I_{TRT} = \left| \frac{tr_{am}t'_{ak}t'_{ka}}{1 - (r'_{ka})^2 e^{i\Delta\psi'}} \right|^2, \quad (5.3)$$

where  $r_{am}$  is the Fresnel reflection coefficient at the air-melanin interface, and the phase shift  $\Delta\psi' = \frac{4\pi d\eta_k \cos\beta'}{\lambda}$ . The superscript  $'$  takes account of the possibility that the incoming and outgoing directions are non-symmetric. After reflecting on the randomly distributed melanin granules, we do not expect the R and the TRT components to interfere; thus, we simply add their intensities Eq. (5.2) and Eq. (5.3) together. Due to the melanin layer's low reflectance of only 5% [141], we neglect all subsequent components that

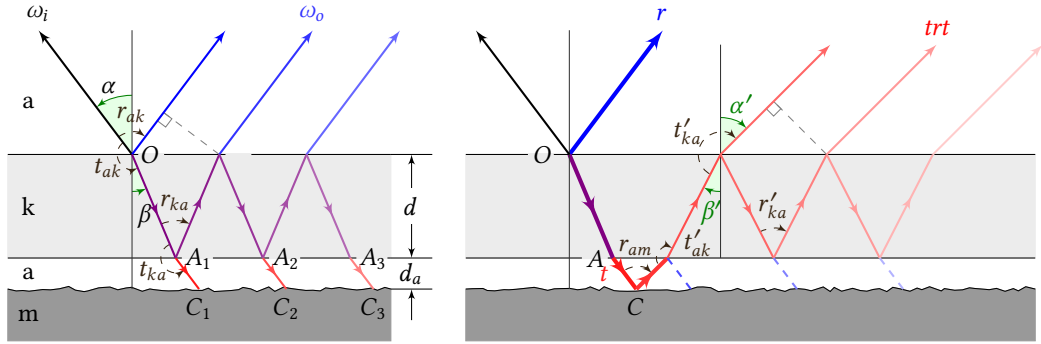


Figure 5.4: Thin-film interference. The keratin layer (k) is surrounded by two air layers (a), beneath these layers lies the randomly dispersed melanin granules (m), which we model as a diffuse surface. **Left:** thin-film reflection (blue arrows) amounts to the R component. **Right:** thin-film reflection (blue) plus TRT component (red), the thick rays on the right summarize the respective thin rays on the left. The components after the blue dashed lines are ignored due to their negligible contribution.

involve interaction with the melanin layer. This choice is validated by the similarity of the blue curve to the measurement in Fig. 5.5.

### 5.3.4 Measuring with an Imaging Scatterometer

Above analyses apply to flat thin films; however, the keratin film in a barbule is curved, as shown in Fig. 5.2c. We deploy the measurement setting designed by Stavenga et al. [110], called *imaging scatterometer* (Fig. 5.6), to measure the influence of the barbule geometry on the reflectance. The resulting far-field scattering image is called a *scatterogram*, which captures the hemispherical reflectance from the sample simultaneously via a digital camera. Examples are shown in Figs. 5.1c to 5.1e. The long, pointed, black object at 9 o'clock is the occlusion from the glass micropipette holding the sample. The white circles indicate various scattering angles of  $\vartheta$ .

We implement in Mitsuba 2 [87] a hemispherical sensor looking from all directions at the sphere origin. This delivers equivalent images as scatterograms.

## 5.4 Modeling

In accordance with the SEM image, the scatterograms in Figs. 5.1d and 5.1e show reflection into a wide solid angle. In particular, the iridescent pattern

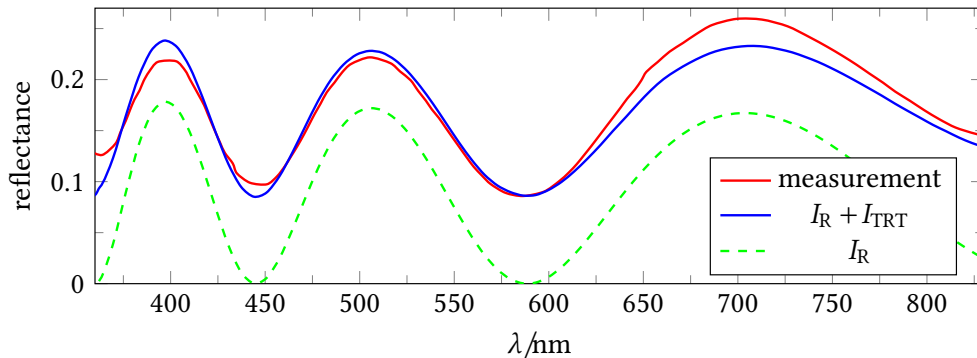


Figure 5.5: Reflectance spectra of a green barbule as measured with an MSP (red, calibrated with a spectralon), and simulated with (blue) or without (green) the background component.

stretches in one diagonal direction, which is the transversal direction of the barbule. In the longitudinal direction, *i.e.* along the barbule axis, the angular span is much smaller. Besides, the green color in Fig. 5.1d has a lower intensity than purple; this is caused by the edges of the barbules (denoted by the blue arrows in Fig. 5.7a), since a surface with a larger curvature reflects the same amount of light to a broader angle. Thus, we model the longitudinal barbule profile to be a small circular section, and the azimuthal profile to be an elliptical section with a larger angular span (Fig. 5.7).

Due to the relatively large IOR of keratin ( $\sim 1.55$  [73]), we assume that light travels a relatively small tangential length before contributing to the reflectance, so that the film can be treated as locally flat when computing interference. Thus, we only consider influence of the barbule curvature on the angular span of the reflectance. More discussions on interference from curved thin films can be found in our supplementary document.

In the following subsection, we derive a new reciprocal BSDF.

#### 5.4.1 Elliptical BSDF

The BSDF  $S(\omega_i, \omega_o, \lambda)$  describes the relationship between the incoming radiance  $L_i$  and the outgoing radiance  $L_o$

$$L_o(\omega_o, \lambda) = \int L_i(\omega_i, \lambda) S(\omega_i, \omega_o, \lambda) \langle \omega_i, \vec{n} \rangle d\omega_i, \quad (5.4)$$

where  $\vec{n}$  is the normal vector of the overlapping barbule plane (Fig. 5.8), and  $S(\omega_i, \omega_o, \lambda) = S_R + S_{\text{TRT}} + S_T$  sums up the R, TRT and T lobes. This formulation complies with the well-known rendering equation, yet differs from

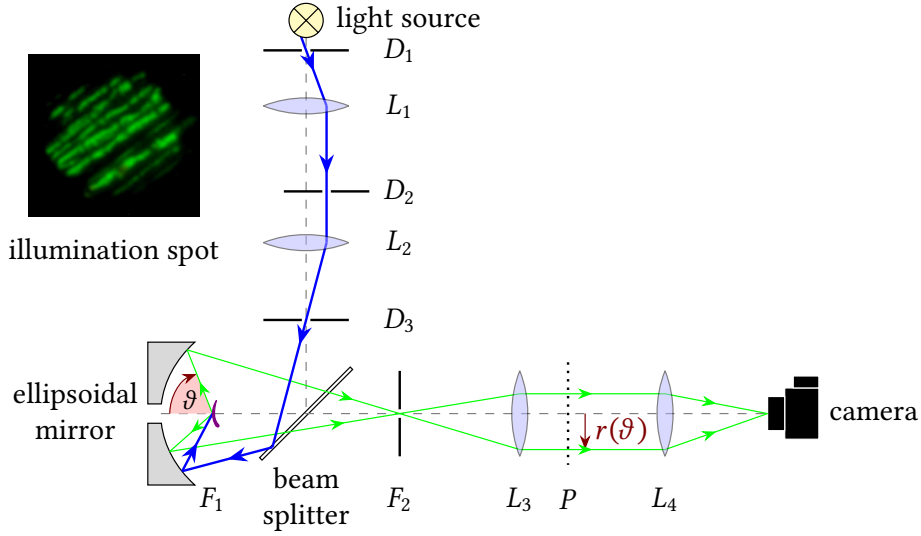


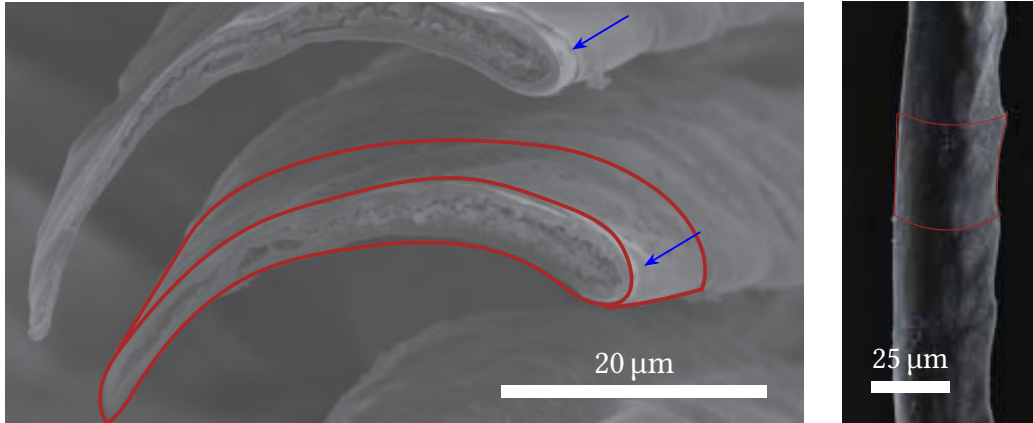
Figure 5.6: Diagram of the imaging scatterometer. A narrow beam (blue) from a xenon lamp is focused through diaphragms  $D_{1,3}$ , lenses  $L_{1,2}$ , the beam splitter together with an ellipsoidal reflector on the sample (purple). Light scattered by the sample into the hemisphere is focused at the second focal point  $F_2$  and delivered to a camera (Canon EOS 30D).  $D_2$  controls the incident angle. **Inset:** Near-field image of a green barb, showing illumination spot of our scatterograms, about  $120 \times 120 \mu\text{m}^2$ , covering  $\sim 30$  barbule cells.

the formulations of fiber scattering models [76, 136, 134], where  $\cos \theta_i$  instead of  $\langle \omega_i, \vec{n} \rangle = \cos \theta_i \cos \phi_i$  is used. This is because their radiance is defined per unit length, while ours is defined per area.

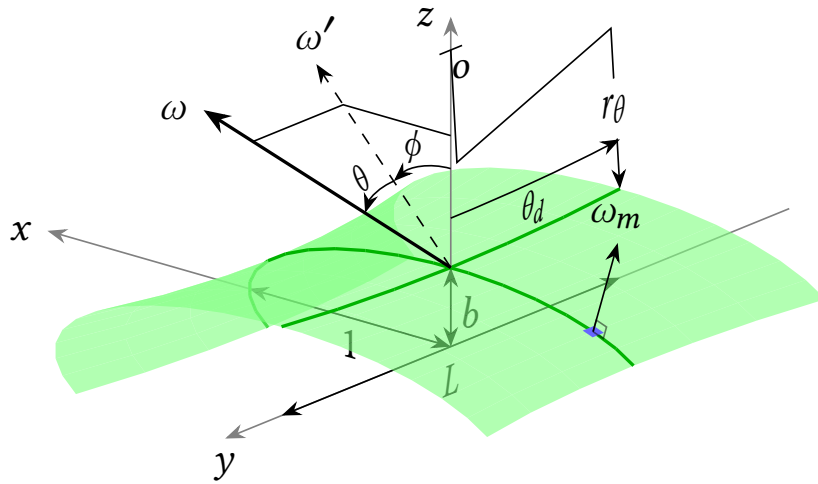
Traditionally, the scattering distribution function  $S$  is divided further into the product of the longitudinal scattering function  $M$  and the azimuthal scattering function  $N$ . However, as argued by d'Eon et al. [28], separating  $S$  causes significant artifacts at grazing angles. We propose to separate the *normal distribution function* (NDF) instead, similar to microfacet models.

**NDF** A barbule can be considered a periodic structure consisting of an array of saddle-like unit barbule cells, as indicated by the red outlines in Fig. 5.7a. We model the exposed front surface (Fig. 5.7b), where the transversal cross-section is represented by an elliptical arc with semi-major axis 1 and semi-minor axis  $b$ , and the longitudinal cross-section is represented by a circular section with a radius  $r_\theta$  and an arc length of  $2r_\theta\theta_d$ .

The overlapping barbules form a plane (“barb plane”, Fig. 5.8), which is the  $x$ - $y$  plane of the barbule coordinate system rotated by angle  $\mu$  around



(a) SEM images of iridescent dove barbules. Left: cross-section view. The blue arrows indicate the edge of the barbules with a large curvature. Right: front view. Images adapted from Nakamura et al. [81], ©2008 The Physical Society of Japan.



(b) A saddle-like unit barbule cell.  $\omega$  stands for incident, outgoing or normal direction, it is parameterized by spherical angles  $\theta$  and  $\phi$ , where  $\theta$  is the angle between  $\omega$  and the  $x-z$  plane and  $\phi$  is the angle from the  $z$  axis to the projection of  $\omega$  onto the  $x-z$  plane ( $\omega'$ ).  $\omega = [\sin \phi \cos \theta, \sin \theta, \cos \phi \cos \theta]^T$ .

Figure 5.7: SEM image and model of a unit barbule cell.

the  $y$  axis. The distance between adjacent barbules is denoted as  $H$ . The NDF in azimuthal direction is

$$D_\phi(\phi_m) = \frac{1}{H\kappa(\phi_m)} = \frac{b^2}{H} (\sin^2 \phi_m + b^2 \cos^2 \phi_m)^{-\frac{3}{2}}, \quad (5.5)$$

where  $\kappa(\phi_m)$  is the curvature at  $\phi = \phi_m$ ,  $\phi_m \in [\phi_0, \phi_1]$ . Dividing by  $H$  ensures that  $\int D_\phi(\phi_m) \cos(\phi_m + \mu) d\phi_m \leq 1$ . The NDF in longitudinal direction is

$$D_\theta(\theta_m) = \frac{1}{2 \sin \theta_d}. \quad (5.6)$$

Combining Eqs. (5.5) and (5.6), we obtain

$$\begin{aligned} D(\omega_m) &= D_\theta(\theta_m) D_\phi(\phi_m) (\cos \theta_m)^{-1} \\ &= \frac{b^2}{2H \sin \theta_d \cos \theta_m} (\sin^2 \phi_m + b^2 \cos^2 \phi_m)^{-\frac{3}{2}}. \end{aligned} \quad (5.7)$$

Eq. (5.7) satisfies  $\int D(\omega_m) \langle \omega_m, \vec{n} \rangle d\omega_m = 1$ .

**Masking and Shadowing** Diffraction often arises from regularly aligned microstructures. However, the barbule spacing is rather large and irregular, and from Figs. 5.1a and 5.5 it is obvious that the most prominent source of iridescence is the thin film. Thus, we apply geometrical optics when considering shadowing and masking.

In previous literature, the correlation between the height and slopes is usually ignored in the geometry term [107], so that each normal direction has a certain probability to be visible, independent of the incident and outgoing angles. In our case, however, the relationship between the height and slopes is known, so that each  $\omega_m$  is either always visible or always invisible, depending on  $\omega_{i,o}$ . When sampling from or evaluating the NDF, we check on-the-fly if there is an intersection of  $\omega_i$  or  $\omega_o$  with the two adjacent barbules. The visibility term  $G(\omega_i, \omega_m, \omega_o)$  is either exactly 1 when there is no intersection, or 0 if at least one intersection exists. This term is *reciprocal*. Figure 5.8 illustrates the visible sections from both  $\omega_i$  and  $\omega_o$  in purple. Multiple interreflections are ignored.

**$S_R$ : Thin-film reflection** For the R lobe,  $\omega_m$  coincides with the half-vector between  $\omega_i$  and  $\omega_o$ , acting as small mirrors. Consider the differential flux  $d\Phi_m$  incident on the differential surface oriented with normal direction  $\omega_m$ . From the definition of the radiance

$$d\Phi_m = L_i(\omega_i, \lambda) \langle \omega_i, \omega_m \rangle d\omega_i dA(\omega_m). \quad (5.8)$$

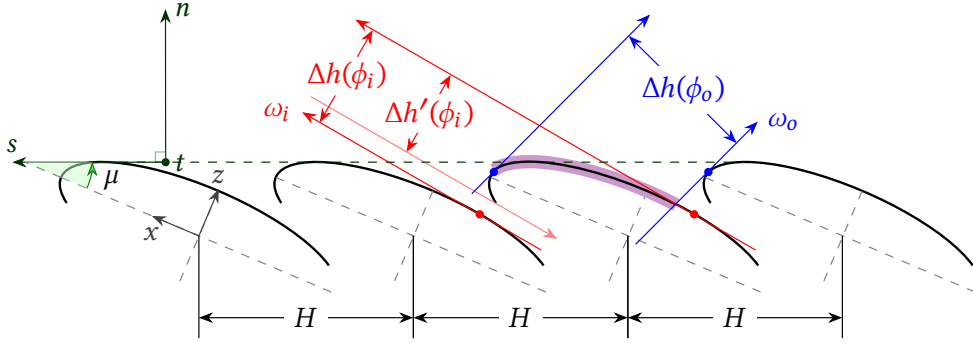


Figure 5.8: Transverse cross-section of a barb plane.

The differential area of the surface with orientation  $\omega_m$  is

$$dA(\omega_m) = D(\omega_m) d\omega_m A, \quad (5.9)$$

where  $A$  is the projected area of a unit barbule cell onto the barb plane. The outgoing flux is

$$d\Phi_o = I_R(\omega_i, \omega_o, \lambda) d\Phi_m. \quad (5.10)$$

The differential outgoing radiance over the projected area  $A_o$  is

$$dL_o(\omega_o, \lambda) = \frac{d\Phi_o}{d\omega_o A_o}. \quad (5.11)$$

Combining above equations and the half-angle mapping  $d\omega_m = \frac{d\omega_o}{4\langle\omega_m, \omega_o\rangle}$  yields

$$dL_o(\omega_o, \lambda) = \frac{I_R(\omega_i, \omega_o, \lambda) L_i(\omega_i, \lambda) D(\omega_m) A d\omega_i}{4A_o}. \quad (5.12)$$

The ratio between the projected areas in normal and outgoing directions is

$$\frac{A}{A_o} = \frac{HL}{\cos\theta_o \Delta h(\phi_o) L} = \frac{H}{\cos\theta_o H \cos(\phi_o + \mu)} = \frac{1}{\langle\omega_o, \vec{n}\rangle}, \quad (5.13)$$

where  $\Delta h(\phi)$  is the projected length in direction  $\phi$  (Fig. 5.8), and  $L$  is the length of a barbule cell along the  $z$  axis. The value of  $L$  is irrelevant as it is canceled out in the equation. Comparing with Eq. (5.4) and adding the term  $G$ , we acquire the BSDF for the R lobe

$$S_R(\omega_i, \omega_o, \lambda) = \frac{I_R(\omega_i, \omega_o, \lambda) D(\omega_m) G(\omega_i, \omega_m, \omega_o)}{4\langle\omega_i, \vec{n}\rangle \langle\omega_o, \vec{n}\rangle}, \quad (5.14)$$

which is exactly the form of a microfacet BRDF.

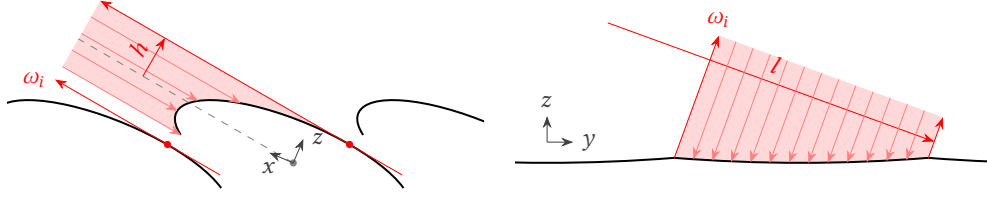


Figure 5.9: Uniform sampling of  $h$  and  $l$ .

**$S_T$ : Transmission through barbule spacing** At some angles, part of the light rays do not hit the barbule surface (Fig. 5.8), causing  $\int D_\phi(\phi_m) \cos(\phi_i - \phi_m) d\phi_m < \cos(\phi_i + \mu)$ . In practice, we always sample from the valid projected length, denoted as  $\Delta h'(\phi_i)$ . The rays that do not hit the barbule surface is propagated without changing its direction and intensity, giving the T lobe

$$S_T(\omega_i, -\omega_i, \lambda) = 1 - \frac{\Delta h'(\phi_i)}{\Delta h(\phi_i)}. \quad (5.15)$$

**$S_{TRT}$ : Background component** As seen in Fig. 5.2c, the melanin granules scatter the light into even wider angles. We model the melanin layer as a diffuse surface due to its irregular distribution.

The BSDF for the TRT component is

$$S_{TRT}(\omega_i, \omega_o, \lambda) = \frac{\rho(\omega_i, \omega_o, \lambda)}{\pi}, \quad (5.16)$$

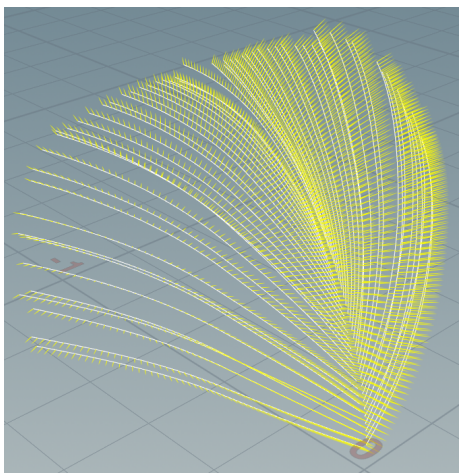
where

$$\rho(\omega_i, \omega_o, \lambda) = \frac{1}{A_i} \iint I_{TRT}(\omega_i, \omega_m, \omega_o) dh dl \quad (5.17)$$

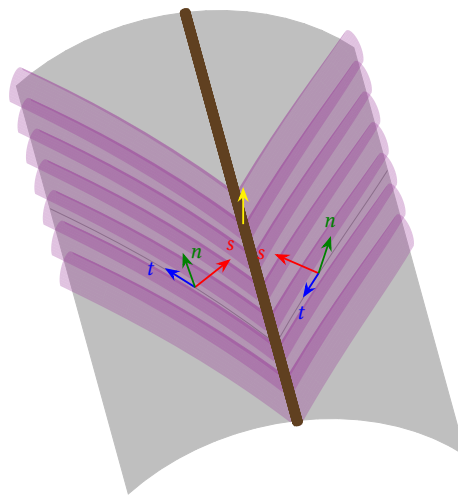
is the reflectance averaged over the illuminated projected area  $A_i$ .  $h, l$  are the azimuthal and longitudinal offsets seen from the illumination direction, respectively (Fig. 5.9). Since  $\omega_m$  is a function of  $h$  and  $l$ , the above equation is impractical to solve analytically. We compute the integral implicitly by randomly picking  $h$  and  $l$  at each evaluation.

## 5.4.2 Implementation

In this section, we provide the implementation details of our model, including geometry modeling using the software package Houdini and rendering with Mitsuba 2 using `scalar_spectral` variant.



(a) Exemplary Houdini feather



(b) A `barb` primitive

Figure 5.10: Explicit geometry in Houdini (a) and implicit geometry in Mitsuba 2 (b). The barb curves are represented by vertex chains (white in a) with assigned vertex normals in yellow. Our `barb` primitives are modeled as an extrusion of a circular arc (gray). Barbules (purple) and ramus (brown) are illustrative only, their geometry is not modeled in the primitive.  $s, t$  and  $n$  form the local shading coordinate system.

**Geometry Modeling** In Houdini, we model a feather as a collection of barb curves (Fig. 5.10a), as in usual feather grooming pipelines [44]. The vertices with their normal directions and other customizable parameters are exported as a `.ply` file. The geometry is read by a custom `feather` shape plugin in Mitsuba 2, which generates `barb` primitives (Fig. 5.10b). The BSDF described in Section 5.4.1 is applied on these barb primitives, the local shading frame coincides with the local barb plane (Figs. 5.8 and 5.10b).

**Importance Sampling** Our sampling strategy is similar to that proposed by d'Eon et al. [27]: first, the azimuthal offset  $h$  and the longitudinal offset  $l$  are uniformly sampled (Fig. 5.9), then one of the three lobes is chosen proportional to their energy. The PDF for the R lobe is computed the same as in micro-facet models, whereas that for the TRT lobe is the same as for a diffuse surface. The complete sampling procedure is stated in Algorithm 1.

---

**ALGORITHM 1:** Importance Sampling Barbule BSDF

---

```

Output: pdf,  $\omega_o$ , sample value
sample valid  $h$  and  $l$  and compute  $\omega_m(h, l)$ ;
calculate  $I_R(\omega_i, \omega_m)$  according to Eq. (5.2);
sample  $\omega_o^{\text{TRT}}$  from the cosine-weighted upper hemisphere around  $\vec{n}$ ;
 $\omega_o^{\text{TRT}} *= \text{sgn}\langle \omega_m, \omega_o^{\text{TRT}} \rangle$ ;
calculate  $I_{\text{TRT}}(\omega_i, \omega_m, \omega_o^{\text{TRT}})$  according to Eq. (5.3);
generate uniform random sample  $\xi \sim [0, I_R + I_{\text{TRT}} + \Delta h_i / \Delta h'_i - 1]$ ;
if  $\xi < I_R$  then /* choose R lobe */
|  $\omega_o = \text{reflect}(\omega_i, \omega_m)$ ; pdf =  $0.25 I_R D(\omega_m) / \langle \omega_i, \vec{n} \rangle$ ;
else if  $\xi < I_R + I_{\text{TRT}}$  then /* choose TRT lobe */
|  $\omega_o = \omega_o^{\text{TRT}}$ ; pdf =  $I_{\text{TRT}} |\omega_o \cdot z| / \pi$ ;
else /* choose T lobe. */
|  $\omega_o = -\omega_i$ ; pdf =  $\Delta h_i / \Delta h'_i - 1$ ;
end
if sample position visible from  $\omega_o$  then
| pdf /=  $I_R + I_{\text{TRT}} + \Delta h_i / \Delta h'_i - 1$ ;
| sample value =  $(I_R + I_{\text{TRT}} - 1) \Delta h'_i / \Delta h_i + 1$ ;
else
| reject sample;
end

```

---



Figure 5.11: Comparison between calibrated photographs (**top**) and renderings with comparable light and view (**bottom**). The only linear light source (illuminant E) has inclination angles range from  $0^\circ$  to  $60^\circ$  from left to right. The non-iridescent parts of the barbules (invisible on the neck since feathers are overlapping) are approximated with a thicker film.

## 5.5 Results and Comparison

In this section, we compare our rendered results with the measurements. The source code is available at [https://github.com/RiverInTheSky/dove\\_neck](https://github.com/RiverInTheSky/dove_neck).

### 5.5.1 Comparison with Scatterograms

Rock dove neck feathers were collected from a frozen dove. We removed one green barb from a neck feather and investigated the scattering with the scatterometer. The colors are not calibrated.

In Figs. 5.1c to 5.1e, the scatterograms are compared with our BSDF renderings. The parameters are manually chosen to fit the scatterograms:  $b = 0.25$ ,  $\phi_0 = -0.37$ ,  $\phi_1 = 2.64$ ,  $H = 1.25$ ,  $d = 590$  nm,  $\theta_d = 0.0785$ ,  $\mu = -0.35$ . We conduct an ablation study of the effect of each of those parameters in the supplementary document.

In Fig. 5.1c (top), the sample is illuminated omnidirectionally by removing diaphragm  $D_2$ , which we replicate in the renderer with a constant emitter. The green color in the inner ring indicates the reflectance around normal incidence, whereas oblique incidence angles (the middle ring) produce purple color. At grazing angles, the reflectance approaches 1; as a result, the barbule looks yellowish and bright. These characteristics are all predicted in Fig. 5.3 and reproduced in Fig. 5.1c (bottom). The darker region in the lower-left part of the scatterogram is also present in our rendering, which is due to the inclination of the local barb plane. We believe that the reflectance in this region does not fall off completely because of random perturbations of the

barbule orientations: they do not align perfectly to a flat surface on a larger scale. We choose not to model the randomness in the BSDF term, but rather to add a random noise in the orientation  $\mu$  of the unit barbule cells when exporting the barb curve geometry, as the influence of these perturbations is also visible on a macroscopic level (Fig. 5.11).

In Figs. 5.1d and 5.1e, the scatterograms (top row) were illuminated from an angular aperture of about  $16^\circ$ ; for the renderings (bottom row), we achieve an equivalent illumination with a disk area light. The stretching in the transversal direction, the transition between green and purple, and the lower intensity in the upper-right part are all well captured in the rendering. The large round background is the TRT component; its color is mostly brownish due to the reflectance of the melanin granules; however, there are also faint iridescent colors in the background. More precisely, the color is purple near the center and green near the periphery, exactly the reversed order as the R component. This is because when the reflected color is green, the transmitted color would be its complement, which is purple and vice versa. Our TRT lobe model follows this behavior. Also, the diffuse assumption of the melanin layer seems appropriate, as both scatterogram and rendering show similar intensity gradients that turn almost invisible toward the outer ring.

## 5.5.2 Comparison with Photographs

We further measure a rock dove neck feather in a calibrated appearance scanner TAC7 [133]. The device contains several radiometrically calibrated cameras and light sources. We use a camera observing the feather from  $45^\circ$  inclination and a series of light inclination angles. The resulting images in Fig. 5.11 are HDR-combined, calibrated and converted to linear sRGB. The renderings are obtained by modeling a similar scene in Mitsuba 2, with the feather geometry coarsely matched against the real sample. The color shifting, the glints and the irregularities are well reproduced.

## 5.5.3 Performance

Figure 5.1b shows a scene with 256 overlapping feathers (including 1032192 barb primitives), rendered with 256 samples per pixel and a resolution of  $1024 \times 768$ . The image took 8.3 min to render,  $2.1\times$  slower than rendering the identical geometry with plain thin films implemented by [10].

## 5.6 Conclusion and Future Work

In this chapter we have presented a novel framework for rendering feathers. We measure the BSDF of a feather barb from several illumination angles with a scatterometer, based upon which we design a parameterized BSDF. It is straightforward to sample and compatible with existing rendering pipelines for feathers.

Although the transversal cross-section is restricted to be elliptical in our work, the same idea could be applied to barbules of other shapes. In fact, any convex cross-section with  $C^2$  continuity has a continuous curvature and produces a continuous NDF. This amounts to changing  $D_\phi$  in Eq. (5.5). Roughness in the cortex is not a part of our model, as the barbule surface is very smooth. A modification in the NDF can be applied to achieve roughness if needed.

Our work only focuses on rendering the barbules, as their reflectance is the most prominent on rock dove feathers. For some birds, the structural colors instead originate from a sponge-like structure of the ramus [118, 92, 113] which is currently not considered by our model and could be covered in future work. Another potential extension would be the combination of iridescent and non-iridescent barbules, the latter ones being sometimes more opaque and possibly in need of further shading lobes.

As the measuring device was originally only designed for observational purposes, the colors are not properly calibrated. In the future, a full spectral calibration and an automated parameter fitting procedure could make the model more accurate and versatile.



## 6. Conclusion and Future Work

In this thesis, we explore a few aspects lacking in physically based modeling, namely the microappearance of soap bubbles, human hair, and bird feather.

In Chapter 3, we simulate chemomechanical fluid flows on soap bubbles. The fluid flow is mainly governed by the Navier-Stokes equations. The surfactant concentration at both film surfaces influences the surface tension, thus entering the stress boundary conditions. The surfactant concentration is further driven by the advection-diffusion equation. Although the fluid flow is intrinsically 3D, the scale of the film thickness in the radial direction is much smaller than the film's lateral extent; therefore, a direct simulation of the 3D equations would introduce large errors. A common approach in this case is to divide the physical quantities by their characteristic units, so that the resulting dimensionless quantities are at the same scale. After that, we asymptotically expand the variables, and only solve the leading order equations.

The above-mentioned theoretical aspects are primarily adapted from the works of Chomaz [20], Ida and Miksis [55, 56]. We are not the first in computer graphics to discover their works on soap films, but the first to reveal the expressiveness of their models by introducing numerical methods to solve the governing equations. We first introduce a great-circle advection scheme, where we construct a velocity-aligned local coordinate system instead of directly advect quantities along the global coordinate, thus preventing artifacts at the poles. We also keep a forward and a backward mapping to prevent the texture from blurring, preserving the rich details on soap bubbles. When applying body forces, we face the problem of prohibitively small step sizes, which we address by substituting the divergence term in the concentration transport equation with a rearrangement of the velocity in the momentum equation, resulting in an implicit system. Afterward, we express the linear system as a sparse matrix, and solve it with CUDA and AmgX using a preconditioned conjugate gradient method. Finally, we discuss the influence of various external forces.

Our work has greatly improved the realism of fluid simulation on soap films, and has inspired people to simulate the same phenomenon. In particular, our advection scheme is used in a work by Wang et al. [126] on soap

films and bubbles. They also considered viscosity, which we ignored. A recent work by Deng et al. [25] follows our implicit formulation of the surfactant concentration to simulate fluid flows on flat films and on soap bubble clusters. They even introduced black spots, which are absent in our model. However, the generation of black spots is seeded, instead of in a physically based way, since their framework can not handle the large force gradient at the spot boundary. The same holds for the large thickness differences at the frame boundaries for soap films. Also, the simulation is still far from real-time performance. We hope these problems can be addressed in the future.

Chapters 4 and 5 are based on the same idea: extending the microfacet model.

The microfacet model represents a flat macrosurface as a collection of small mirror-like facets, whose normal directions follow a certain distribution. The same representation must also work on a curved surface, because microfacets on a curved surface also have a certain normal distribution function. Therefore, we model human hair as a rough (elliptical) cylinder made of microfacets. By analyzing the incoming and outgoing radiance of such a shape in Sections 4.3.1 and 4.3.3, we point out that the NDF is basically an integration of the planar NDF along the azimuthal curve, which allows us to use the same formulation as the Cook-Torrance model for the reflection component. There even exists an analytical solution for the Trowbridge-Reitz (GGX) distribution on circular cross-sections. However, the situation gets more complicated for subsequent components because transmission is involved. We follow the derivation by Walter et al. [125] of refraction through rough surfaces, and formulate the TT and TRT components as integrations in 3D and 5D. In order to evaluate such multidimensional integrations efficiently, we combine the quadrature and Monte Carlo method. We verify the correctness of our formulation by comparing it with brute-force Monte-Carlo traced results. We further show that our rendered results match the strong forward scattering in a rim portrait photograph and the angle-dependent highlight of elliptical hair.

Despite close visual matches, our hair model remains primarily a theoretical model that demonstrates the potential of microfacet model on curved surfaces. For example, the common assumptions for hair scattering models are that hair has elliptical cross-sections, the inner structure is homogeneous, and the contribution of the medulla is ignored. However, in Fig. 1.3 we see that ellipses can only approximately match the hair cross-sections, there exist irregularities. Also, especially for Asian and African hair, the distribution of melanin granules is not homogeneous, and the medulla in the middle is well visible despite being small. How well our assumptions hold still needs to be verified by more thorough measurements. Moreover, the human hair

shape is far from a perfect cylinder. Nature processes and chemical treatment would damage the hair and change its appearance: the cuticle might have larger and varied tilt angles, the hair might break or have split ends, and wave optics effects might arise from the microstructures. All these effects are not covered by current hair scattering models. Besides, our formulation is limited to human head hairs. Whether other body hair, such as the beard or the shorter, thinner vellus hair which covers most parts of the human body can be described by the same model should be investigated in the future. The possible extension to animal fur would also make an interesting topic.

The connection between the feather barb and the microfacet model might not be that obvious at first glance due to the overlapping, repetitive and discontinuous structure of the former. However, our analysis in Section 5.4.1 shows that the BRDF of both has exactly the same form. We usually conceptualize microfacets as flat mirrors. However, in 1975, Trowbridge and Reitz [120] proposed an alternative representation of rough surfaces: curved microareas. The curved barbule shape can therefore also be considered a microarea, the NDF of which is derived from its curvatures. This formulation turns out to match the BRDF measurement well: the different axial and lateral extent, and the different intensities across the lateral direction are all due to the NDF of the barbule. We also consider the masking and shadowing as well as the gaps between barbules. The randomly distributed melanin granules underneath the thin keratin film are modeled as a diffuse surface. Besides, we model the angle between the barbules and the ramus by shifting the local shading frame.

Our model on rock dove neck feathers is the first one to consider the geometric structure of feathers down to the barbule cross-sections. It also represents the random orientations of the barbules as a texture on the macroscale. While it is restricted to rock dove neck feathers, the same idea should be applicable to other types of feathers, since all avian feathers have the same feather-barb-barbule structure, and almost only differ in the exact barbule cross-sections and the color mechanisms. It is therefore thinkable to use a parametric model to represent the NDFs of various barbule cross-sections. For that, one needs a well-calibrated BRDF measurement device and a rigorous measurement pipeline, those are left for future works.

Our feather scattering model was designed earlier than the hair model. Although we tried our best to match the reflectance behavior using a microfacet-like model, the transmission is modeled in a much-approximated way. At that time, a more expressive model that considers the multiple interactions inside the barbule was unthinkable and also unnecessary for rock dove neck feathers with large internal absorption. Later, we designed the hair model, and showed that subsequent interactions inside a non-cylindrical structure can

be calculated straightforwardly. This new formulation would be especially meaningful for light-colored feathers, where transmission through the feather contributes to the appearance greatly. It is therefore our hope to combine the hair model in Chapter 4 and the feather model in Chapter 5 in the future to represent even larger categories of bird feathers.

Although these details in microappearance might seem subtle, they are already identified by people before us, it was only due to the lack of proper models that people tried to fake these effects by using random noise textures, twisting roughness values for front and rear view, or mixing different shaders. Amazingly, great artists can make use of very limited tools to fake results that are quite convincing to untrained eyes. However, a physically based solution would spare such effort, the solution would also be more expressive and ensure consistency across the frames. With this dissertation, we have pushed the level of photorealism in computer graphics a step forward. At the time of writing, our research has attracted the attention of various production renderers, including the ones used by Wētā FX, Autodesk, and Blender.

Though, there remains much work to do. In addition to the various limitations we discussed about our soap bubble, hair, and feather models at the end of each chapter, a lot more topics remain to be better covered by physically based models, such as gemstones, vegetation, or any materials and natural phenomena around us that are currently over-simplified. We need to better understand the physical processes behind each phenomenon, perform extensive measurements, and design efficient algorithms to finally close the gap between simulated and physical reality.

# Bibliography

- [1] Carlos Aliaga, Carlos Castillo, Diego Gutierrez, Miguel A Otaduy, Jorge Lopez-Moreno, and Adrian Jarabo. An appearance model for textile fibers. In *Computer Graphics Forum*, volume 36, pages 35–45. Wiley Online Library, 2017.
- [2] Ryoichi Ando, Nils Thuerey, and Chris Wojtan. A stream function solver for liquid simulations. *ACM Transactions on Graphics (TOG)*, 34(4):1–9, 2015.
- [3] Omri Azencot, Orestis Vantzos, Max Wardetzky, Martin Rumpf, and Mirela Ben-Chen. Functional thin films on surfaces. In *Proceedings of the 14th ACM SIGGRAPH/Eurographics Symposium on Computer Animation*, pages 137–146, 2015.
- [4] Jessica Baron. Procedurally generating biologically driven bird and non-avian dinosaur feathers. 2018.
- [5] Jessica Baron, Daljit Singh Dhillon, and Eric Patterson. Procedural shading for rendering the appearance of feathers. In *Special Interest Group on Computer Graphics and Interactive Techniques Conference Posters*, pages 1–2, 2021.
- [6] Jessica Baron, Daljit Singh Dhillon, N Adam Smith, and Eric Patterson. Microstructure-based appearance rendering for feathers. *Computers & Graphics*, 2021.
- [7] Jessica Baron and Eric Patterson. Procedurally generating biologically driven feathers. In *Computer Graphics International Conference*, pages 342–348. Springer, 2019.
- [8] G. K. Batchelor. *An Introduction to Fluid Dynamics*. Cambridge Mathematical Library. Cambridge University Press, 1967.
- [9] Petr Beckmann. Shadowing of random rough surfaces. *IEEE transactions on antennas and propagation*, 13(3):384–388, 1965.

- [10] Laurent Belcour and Pascal Barla. A practical extension to microfacet theory for the modeling of varying iridescence. *ACM Transactions on Graphics (TOG)*, 36(4):1–14, 2017.
- [11] Alexis Benamira and Sumanta Pattanaik. A Combined Scattering and Diffraction Model for Elliptical Hair Rendering. *Computer Graphics Forum*, 2021.
- [12] Christoph G. Birngruber and Marcel A. Verhof. The color of human hair. In Victor R. Preedy, editor, *Handbook of Hair in Health and Disease*, chapter 2, pages 31–49. Wageningen Academic Publishers, Wageningen, 2012.
- [13] Benedikt Bitterli, Chris Wyman, Matt Pharr, Peter Shirley, Aaron Lefohn, and Wojciech Jarosz. Spatiotemporal reservoir resampling for real-time ray tracing with dynamic direct lighting. *ACM Transactions on Graphics (TOG)*, 39(4):148–1, 2020.
- [14] Max Born and Emil Wolf. *Principles of optics: electromagnetic theory of propagation, interference and diffraction of light*. Pergamon Press, 1970.
- [15] Robert Bridson. *Fluid simulation for computer graphics*. AK Peters/CRC Press, 2015.
- [16] John Burkardt. `sphere_lebedev_rule`, 2010.
- [17] Brian Cabral and Leith Casey Leedom. Imaging vector fields using line integral convolution. In *Proceedings of the 20th Annual Conference on Computer Graphics and Interactive Techniques, SIGGRAPH '93*, page 263–270, New York, NY, USA, 1993. Association for Computing Machinery.
- [18] Yanyun Chen, Yingqing Xu, Baining Guo, and Heung-Yeung Shum. Modeling and rendering of realistic feathers. *ACM Transactions on Graphics (TOG)*, 21(3):630–636, 2002.
- [19] Matt Jen-Yuan Chiang, Benedikt Bitterli, Chuck Tappan, and Brent Burley. A practical and controllable hair and fur model for production path tracing. In *Computer Graphics Forum*, volume 35, pages 275–283. Wiley Online Library, 2016.
- [20] Jean-Marc Chomaz. The dynamics of a viscous soap film with soluble surfactant. *Journal of Fluid Mechanics*, 442:387–409, 2001.

- [21] Robert L Cook and Kenneth E. Torrance. A reflectance model for computer graphics. *ACM Transactions on Graphics (ToG)*, 1(1):7–24, 1982.
- [22] Y Couder, JM Chomaz, and M Rabaud. On the hydrodynamics of soap films. *Physica D: Nonlinear Phenomena*, 37(1-3):384–405, 1989.
- [23] Fang Da, Christopher Batty, Chris Wojtan, and Eitan Grinspun. Double bubbles sans toil and trouble: Discrete circulation-preserving vortex sheets for soap films and foams. *ACM Trans. on Graphics (SIGGRAPH 2015)*, 2015.
- [24] Douglas W Deedrick and Sandra L Koch. Microscopy of hair part i: A practical guide and manual for human hairs. *Forensic science communications*, 6(1), 2004.
- [25] Yitong Deng, Mengdi Wang, Xiangxin Kong, Shiyong Xiong, Zangyueyang Xian, and Bo Zhu. A moving eulerian-lagrangian particle method for thin film and foam simulation. *ACM Transactions on Graphics (TOG)*, 41(4):1–17, 2022.
- [26] Eugene d’Eon, Guillaume Francois, Martin Hill, Joe Letteri, and Jean-Marie Aubry. An energy-conserving hair reflectance model. In *Computer Graphics Forum*, volume 30, pages 1181–1187. Wiley Online Library, 2011.
- [27] Eugene d’Eon, Steve Marschner, and Johannes Hanika. Importance sampling for physically-based hair fiber models. In *SIGGRAPH Asia 2013 Technical Briefs*, pages 1–4. 2013.
- [28] Eugene d’Eon, Steve Marschner, and Johannes Hanika. A fiber scattering model with non-separable lobes. In *ACM SIGGRAPH 2014 Talks*, pages 1–1. 2014.
- [29] Craig Donner and Henrik Wann Jensen. A spectral bsrdf for shading human skin. *Rendering techniques*, 2006:409–418, 2006.
- [30] Jonathan Dupuy, Eric Heitz, Jean-Claude Iehl, Pierre Poulin, Fabrice Neyret, and Victor Ostromoukhov. Linear Efficient Antialiased Displacement and Reflectance Mapping. *ACM Transactions on Graphics*, 32(6):Article No. 211, November 2013.
- [31] Ronald Fedkiw, Jos Stam, and Henrik Wann Jensen. Visual simulation of smoke. In *Proceedings of the 28th annual conference on Computer graphics and interactive techniques*, pages 15–22, 2001.

- [32] Florian Ferstl, Ryoichi Ando, Chris Wojtan, Rüdiger Westermann, and Nils Thuerey. Narrow band flip for liquid simulations. 35(2):225–232, 2016.
- [33] Nick Foster and Ronald Fedkiw. Practical animation of liquids. In *Proceedings of the 28th annual conference on Computer graphics and interactive techniques*, pages 23–30, 2001.
- [34] Nick Foster and Dimitri Metaxas. Realistic animation of liquids. *Graphical models and image processing*, 58(5):471–483, 1996.
- [35] Cristiano G Franco and Marcelo Walter. Modeling and rendering of individual feathers. In *Proceedings. XV Brazilian Symposium on Computer Graphics and Image Processing*, pages 293–299. IEEE, 2002.
- [36] Cristiano G Franco and Marcelo Walter. Direct texture synthesis of feather pigmentation patterns. In *GRAPP (GM/R)*, pages 277–283, 2007.
- [37] Pascal Freyer and Doekele G Stavenga. Biophotonics of diversely coloured peacock tail feathers. *Faraday Discussions*, 223:49–62, 2020.
- [38] Theodore F Gast, Craig Schroeder, Alexey Stomakhin, Chenfanfu Jiang, and Joseph M Teran. Optimization integrator for large time steps. *IEEE transactions on visualization and computer graphics*, 21(10):1103–1115, 2015.
- [39] C Gaulon, C Derec, T Combriat, Philippe Marmottant, and F Elias. Sound and vision: visualization of music with a soap film. *European Journal of Physics*, 38(4):045804, 2017.
- [40] Morteza Gharib and Philip Derango. A liquid film (soap film) tunnel to study two-dimensional laminar and turbulent shear flows. *Physica D: Nonlinear Phenomena*, 37(1-3):406–416, 1989.
- [41] Abhijeet Ghosh, Shruthi Achutha, Wolfgang Heidrich, and Matthew O’Toole. Brdf acquisition with basis illumination. In *2007 IEEE 11th International Conference on Computer Vision*, pages 1–8. IEEE, 2007.
- [42] Marco Giraldo, Juliana Sosa, and Doekele Stavenga. Feather iridescence of coeligena hummingbird species varies due to differently organized barbs and barbules. *Biology Letters*, 17(8):20210190, 2021.
- [43] Andrew Glassner. Soap bubbles: Part 2. *IEEE Computer Graphics and Applications*, 20(6):99–109, 2000.

- [44] Rasmus Haapaoja and Christoph Genzwürker. Mesh-driven generation and animation of groomed feathers. In *ACM SIGGRAPH 2019 Talks*, pages 1–2. 2019.
- [45] Torsten Hädrich, Miłosz Makowski, Wojtek Pałubicki, Daniel T Banuti, Sören Pirk, and Dominik L Michels. Stormscapes: Simulating cloud dynamics in the now. *ACM Transactions on Graphics (TOG)*, 39(6):1–16, 2020.
- [46] James E Harvey, Ryan G Irvin, and Richard N Pfisterer. Modeling physical optics phenomena by complex ray tracing. *Optical Engineering*, 54(3):035105, 2015.
- [47] Todd Alan Harvey, Kimberly S Bostwick, and Steve Marschner. Directional reflectance and milli-scale feather morphology of the african emerald cuckoo, *chrysococcyx cupreus*. *Journal of the Royal Society Interface*, 10(86):20130391, 2013.
- [48] Eric Heitz. Understanding the masking-shadowing function in microfacet-based brdfs. *Journal of Computer Graphics Techniques (JCGT)*, 3(2):48–107, June 2014.
- [49] Eric Heitz and Eugene d’Eon. Importance sampling microfacet-based bsdfs using the distribution of visible normals. In *Computer Graphics Forum*, volume 33, pages 103–112. Wiley Online Library, 2014.
- [50] Eric Heitz, Johannes Hanika, Eugene d’Eon, and Carsten Dachsbacher. Multiple-scattering microfacet bsdfs with the smith model. *ACM Transactions on Graphics (TOG)*, 35(4):1–14, 2016.
- [51] David J Hill and Ronald D Henderson. Efficient fluid simulation on the surface of a sphere. *ACM Transactions on Graphics (TOG)*, 35(2):1–9, 2016.
- [52] Weizhen Huang, Matthias B Hullin, and Johannes Hanika. A microfacet-based hair scattering model. In *Computer Graphics Forum*, volume 41, pages 79–91. Wiley Online Library, 2022.
- [53] Weizhen Huang, Julian Iseringhausen, Tom Kneiphof, Ziyin Qu, Chenfanfu Jiang, and Matthias B Hullin. Chemomechanical simulation of soap film flow on spherical bubbles. *ACM Transactions on Graphics (TOG)*, 39(4):41–1, 2020.

- [54] Weizhen Huang, Sebastian Merzbach, Clara Callenberg, Doekele Stavenga, and Matthias Hullin. Rendering iridescent rock dove neck feathers. In *ACM SIGGRAPH 2022 Conference Proceedings*, pages 1–8, 2022.
- [55] MP Ida and Michael J Miksis. The dynamics of thin films i: General theory. *SIAM Journal on Applied Mathematics*, 58(2):456–473, 1998.
- [56] MP Ida and Michael J Miksis. The dynamics of thin films ii: Applications. *SIAM Journal on Applied Mathematics*, 58(2):474–500, 1998.
- [57] Markus Ihmsen, Jens Orthmann, Barbara Solenthaler, Andreas Kolb, and Matthias Teschner. SPH Fluids in Computer Graphics. In Sylvain Lefebvre and Michela Spagnuolo, editors, *Eurographics 2014 - State of the Art Reports*. The Eurographics Association, 2014.
- [58] Cyril Isenberg. *The science of soap films and soap bubbles*. Tieto Cleveton, UK, 1978.
- [59] Sadashige Ishida, Peter Synak, Fumiya Narita, Toshiya Hachisuka, and Chris Wojtan. A model for soap film dynamics with evolving thickness. *ACM Trans. on Graphics*, 39(4), 2020.
- [60] Sadashige Ishida, Masafumi Yamamoto, Ryoichi Ando, and Toshiya Hachisuka. A hyperbolic geometric flow for evolving films and foams. *ACM Trans. Graph.*, 36(6):199:1–199:11, November 2017.
- [61] Kei Iwasaki, Keichi Matsuzawa, and Tomoyuki Nishita. Real-time rendering of soap bubbles taking into account light interference. In *Proceedings Computer Graphics International, 2004.*, pages 344–348. IEEE, 2004.
- [62] Wenzel Jakob. Mitsuba renderer, 2010. <http://www.mitsuba-renderer.org>.
- [63] Dariusz Jazzkowski and Janusz Rzeszut. Interference colours of soap bubbles. *The Visual Computer*, 19(4):252–270, 2003.
- [64] J. T. Kajiya and T. L. Kay. Rendering fur with three dimensional textures. *SIGGRAPH Comput. Graph.*, 23(3):271–280, July 1989.
- [65] James T Kajiya. The rendering equation. In *Proceedings of the 13th annual conference on Computer graphics and interactive techniques*, pages 143–150, 1986.

- [66] Pramook Khungurn and Steve Marschner. Azimuthal scattering from elliptical hair fibers. *ACM Transactions on Graphics (TOG)*, 36(2):1–23, 2017.
- [67] Pramook Khungurn, Daniel Schroeder, Shuang Zhao, Kavita Bala, and Steve Marschner. Matching real fabrics with micro-appearance models. *ACM Trans. Graph.*, 35(1):1–1, 2015.
- [68] Namjung Kim, SaeWoon Oh, and Kyoungju Park. Giant soap bubble creation model. *Computer Animation and Virtual Worlds*, 26(3-4):445–455, 2015.
- [69] Tom Kneiphof, Tim Golla, and Reinhard Klein. Real-time image-based lighting of microfacet brdfs with varying iridescence. In *Computer Graphics Forum*, volume 38, pages 77–85. Wiley Online Library, 2019.
- [70] James Leaning and Damien Fagnou. Feathers for mystical creatures: creating pegasus for clash of the titans. In *ACM SIGGRAPH 2010 Talks*, pages 1–1. 2010.
- [71] Vyacheslav Ivanovich Lebedev and DN Laikov. A quadrature formula for the sphere of the 131st algebraic order of accuracy. In *Doklady Mathematics*, volume 59, pages 477–481. Pleiades Publishing, Ltd., 1999.
- [72] Joo Ho Lee, Adrian Jarabo, Daniel S Jeon, Diego Gutierrez, and Min H Kim. Practical multiple scattering for rough surfaces. *ACM Transactions on Graphics (TOG)*, 37(6):1–12, 2018.
- [73] Hein L Leertouwer, Bodo D Wilts, and Doekele G Stavenga. Refractive index and dispersion of butterfly chitin and bird keratin measured by polarizing interference microscopy. *Optics Express*, 19(24):24061–24066, 2011.
- [74] Xingyue Li, Betty Sovilla, Chenfanfu Jiang, and Johan Gaume. The mechanical origin of snow avalanche dynamics and flow regime transitions. *The Cryosphere*, 14(10):3381–3398, 2020.
- [75] Miles Macklin and Matthias Müller. Position based fluids. *ACM Transactions on Graphics (TOG)*, 32(4):1–12, 2013.
- [76] Stephen R Marschner, Henrik Wann Jensen, Mike Cammarano, Steve Worley, and Pat Hanrahan. Light scattering from human hair fibers. *ACM Transactions on Graphics (TOG)*, 22(3):780–791, 2003.

- [77] Dakota E McCoy, Teresa Feo, Todd Alan Harvey, and Richard O Prum. Structural absorption by barbule microstructures of super black bird of paradise feathers. *Nature communications*, 9(1):1–8, 2018.
- [78] Tinihau Meuel, Yong Liang Xiong, Patrick Fischer, Charles-Henri Bruneau, Miloud Bessafi, and Hamid Kellay. Intensity of vortices: from soap bubbles to hurricanes. *Scientific reports*, 3:3455, 2013.
- [79] Thomas Müller, Markus Gross, and Jan Novák. Practical path guiding for efficient light-transport simulation. In *Computer Graphics Forum*, volume 36, pages 91–100. Wiley Online Library, 2017.
- [80] A Musbach, GW Meyer, F Reitich, and Sang-Hyun Oh. Full wave modelling of light propagation and reflection. In *Computer Graphics Forum*, volume 32, pages 24–37. Wiley Online Library, 2013.
- [81] Eri Nakamura, Shinya Yoshioka, and Shuichi Kinoshita. Structural color of rock dove’s neck feather. *Journal of the Physical Society of Japan*, 77(12):124801, 2008.
- [82] Rahul Narain, Jonas Zehnder, and Bernhard Thomaszewski. A second-order advection-reflection solver. *Proceedings of the ACM on Computer Graphics and Interactive Techniques*, 2(2):1–14, 2019.
- [83] Maxim Naumov, M Arsaev, Patrice Castonguay, J Cohen, Julien Demouth, Joe Eaton, S Layton, N Markovskiy, István Reguly, Nikolai Sakharnykh, et al. Amgx: A library for gpu accelerated algebraic multi-grid and preconditioned iterative methods. *SIAM Journal on Scientific Computing*, 37(5):S602–S626, 2015.
- [84] Duc Quang Nguyen, Ronald Fedkiw, and Henrik Wann Jensen. Physically based modeling and animation of fire. In *Proceedings of the 29th annual conference on Computer graphics and interactive techniques*, pages 721–728, 2002.
- [85] Michael B Nielsen, Morten Bojsen-Hansen, Konstantinos Stamatelos, and Robert Bridson. Physics-based combustion simulation. *ACM Transactions on Graphics (TOG)*, 41(5):1–21, 2022.
- [86] Vincent Adriaan Nierstrasz and Gert Frens. Marginal regeneration and the marangoni effect. *Journal of colloid and interface science*, 215(1):28–35, 1999.

- [87] Merlin Nimier-David, Delio Vicini, Tizian Zeltner, and Wenzel Jakob. Mitsuba 2: A retargetable forward and inverse renderer. *Transactions on Graphics (Proceedings of SIGGRAPH Asia)*, 38(6), December 2019.
- [88] Yoichi Ochiai, Alexis Oyama, Takayuki Hoshi, and Jun Rekimoto. Theory and application of the colloidal display: Programmable bubble screen for computer entertainment. In Dennis Reidsma, Haruhiro Katayose, and Anton Nijholt, editors, *Advances in Computer Entertainment*, pages 198–214. Springer, 2013.
- [89] Toshio Okazaki. Green and purple structural color development by thin film interference and eumelanin distribution of dove feathers. *Int J Anal Bio-Sci Vol*, 7(4), 2019.
- [90] Alexander Oron, Stephen H Davis, and S George Bankoff. Long-scale evolution of thin liquid films. *Reviews of modern physics*, 69(3):931, 1997.
- [91] Marcel Padilla, Oliver Gross, Felix Knöppel, Albert Chern, Ulrich Pinkall, and Peter Schröder. Filament based plasma. *ACM Transactions on Graphics (TOG)*, 41(4):1–14, 2022.
- [92] Andrew J Parnell, Adam L Washington, Oleksandr O Mykhaylyk, Christopher J Hill, Antonino Bianco, Stephanie L Burg, Andrew JC Dennison, Mary Snape, Ashley J Cadby, Andrew Smith, et al. Spatially modulated structural colour in bird feathers. *Scientific reports*, 5(1):1–10, 2015.
- [93] Matt Pharr. The implementation of a hair scattering model, 2016.
- [94] Matt Pharr, Wenzel Jakob, and Greg Humphreys. *Physically based rendering: From theory to implementation*. Morgan Kaufmann, 3 edition, 2018.
- [95] Olivier Pironneau, J Liou, and T Tezduyar. Characteristic-galerkin and galerkin/least-squares space-time formulations for the advection-diffusion equation with time-dependent domains. *Computer Methods in Applied Mechanics and Engineering*, 100(1):117–141, 1992.
- [96] Ziyin Qu, Xinxin Zhang, Ming Gao, Chenfanfu Jiang, and Baoquan Chen. Efficient and conservative fluids using bidirectional mapping. *ACM Transactions on Graphics (TOG)*, 38(4):128, 2019.

- [97] David A Randall, Todd D Ringler, Ross P Heikes, Phil Jones, and John Baumgardner. Climate modeling with spherical geodesic grids. *Computing in Science & Engineering*, 4(5):32–41, 2002.
- [98] Alexander Reshetov and David Luebke. Phantom ray-hair intersection. *Proceedings of the ACM on Computer Graphics and Interactive Techniques*, 1(2):1–22, 2018.
- [99] Osborne Reynolds. Iv. on the theory of lubrication and its application to mr. beauchamp tower’s experiments, including an experimental determination of the viscosity of olive oil. *Philosophical transactions of the Royal Society of London*, 177:157–234, 1886.
- [100] AW Rücker. On black soap films. *Nature*, 16:331–333, 1877.
- [101] Iman Sadeghi, Heather Pritchett, Henrik Wann Jensen, and Rasmus Tamstorf. An artist friendly hair shading system. *ACM Transactions on Graphics (TOG)*, 29(4):1–10, 2010.
- [102] Robert I. Saye and James A. Sethian. Multiscale modeling of membrane rearrangement, drainage, and rupture in evolving foams. *Science*, 340(6133):720–724, 2013.
- [103] Robert I. Saye and James A. Sethian. Multiscale modelling of evolving foams. *Journal of Computational Physics*, 315:273–301, 2016.
- [104] Vincent Schüssler, Eric Heitz, Johannes Hanika, and Carsten Dachsbacher. Microfacet-based normal mapping for robust Monte Carlo path tracing. *Transactions on Graphics (Proceedings of SIGGRAPH Asia)*, 36(6):205:1–205:12, November 2017.
- [105] Daniel Seddon, Martin Auflinger, and David Mellor. Rendertime procedural feathers through blended guide meshes. In *ACM SIGGRAPH 2008 talks*, pages 1–1. 2008.
- [106] F Seychelles, Y Amarouchene, Miloud Bessafi, and H Kellay. Thermal convection and emergence of isolated vortices in soap bubbles. *Physical review letters*, 100(14):144501, 2008.
- [107] Bruce Smith. Geometrical shadowing of a random rough surface. *IEEE transactions on antennas and propagation*, 15(5):668–671, 1967.
- [108] Brian E. Smits and Gary W. Meyer. *Newton’s Colors: Simulating Interference Phenomena in Realistic Image Synthesis*, pages 185–194. Springer Berlin Heidelberg, Berlin, Heidelberg, 1992.

- [109] Jos Stam. Stable fluids. In *Proceedings of the 26th annual conference on Computer graphics and interactive techniques*, pages 121–128, 1999.
- [110] DG Stavenga, HL Leertouwer, P Pirih, and MF Wehling. Imaging scatterometry of butterfly wing scales. *Optics Express*, 17(1):193–202, 2009.
- [111] Doekele G Stavenga, Hein L Leertouwer, N Justin Marshall, and Daniel Osorio. Dramatic colour changes in a bird of paradise caused by uniquely structured breast feather barbules. *Proceedings of the Royal Society B: Biological Sciences*, 278(1715):2098–2104, 2011.
- [112] Doekele G Stavenga, Hein L Leertouwer, Daniel C Osorio, and Bodo D Wilts. High refractive index of melanin in shiny occipital feathers of a bird of paradise. *Light: Science & Applications*, 4(1):e243–e243, 2015.
- [113] Doekele G Stavenga, Jan Tinbergen, Hein L Leertouwer, and Bodo D Wilts. Kingfisher feathers—colouration by pigments, spongy nanostructures and thin films. *Journal of Experimental Biology*, 214(23):3960–3967, 2011.
- [114] Shlomi Steinberg, Pradeep Sen, and Ling-Qi Yan. Towards practical physical-optics rendering. *ACM Transactions on Graphics*, 41(4):1–13, Jul 2022.
- [115] Mary Caswell Stoddard and Richard O Prum. How colorful are birds? evolution of the avian plumage color gamut. *Behavioral Ecology*, 22(5):1042–1052, 2011.
- [116] Lisa Streit and Wolfgang Heidrich. A biologically-parameterized feather model. In *Computer Graphics Forum*, volume 21, pages 565–573. Wiley Online Library, 2002.
- [117] Yinlong Sun. Rendering biological iridescences with rgb-based renderers. *ACM Trans. Graph.*, 25(1):100–129, January 2006.
- [118] Jan Tinbergen, Bodo D Wilts, and Doekele G Stavenga. Spectral tuning of amazon parrot feather coloration by psittacofulvin pigments and spongy structures. *Journal of Experimental Biology*, 216(23):4358–4364, 2013.
- [119] Bertil Trottet, Ron Simenhois, Gregoire Bobillier, Bastian Bergfeld, Alec van Herwijnen, Chenfanfu Jiang, and Johan Gaume. Transition from sub-rayleigh anticrack to supershear crack propagation in snow avalanches. *Nature Physics*, pages 1–5, 2022.

- [120] TS Trowbridge and Karl P Reitz. Average irregularity representation of a rough surface for ray reflection. *JOSA*, 65(5):531–536, 1975.
- [121] Emmanuel Turquin. Practical multiple scattering compensation for microfacet models. URL: [https://blog.selfshadow.com/publications/turquin/ms\\_comp\\_final.pdf](https://blog.selfshadow.com/publications/turquin/ms_comp_final.pdf), 45, 2019.
- [122] Roman Ďurikovič. Animation of soap bubble dynamics, cluster formation and collision. *Comput. Graph. Forum*, 20:C–67–C–75, 09 2001.
- [123] Eric Veach. *Robust Monte Carlo methods for light transport simulation*. Stanford University, 1998.
- [124] P Vukusic and DG Stavenga. Physical methods for investigating structural colours in biological systems. *Journal of the Royal Society Interface*, 6(suppl.2):S133–S148, 2009.
- [125] Bruce Walter, Stephen R Marschner, Hongsong Li, and Kenneth E Torrance. Microfacet models for refraction through rough surfaces. *Rendering techniques*, 2007:18th, 2007.
- [126] Mengdi Wang, Yitong Deng, Xiangxin Kong, Aditya H Prasad, Shiyong Xiong, and Bo Zhu. Thin-film smoothed particle hydrodynamics fluid. *ACM Transactions on Graphics (TOG)*, 40(4):1–16, 2021.
- [127] Andrea Weidlich. *Pseudochromatic Colourisation of Crystals in Predictive Image Synthesis*. PhD thesis, Institute of Computer Graphics and Algorithms, Vienna University of Technology, January 2009.
- [128] Sebastian Werner, Zdravko Velinov, Wenzel Jakob, and Matthias B Hullin. Scratch iridescence: Wave-optical rendering of diffractive surface structure. *ACM Transactions on Graphics (TOG)*, 36(6):1–14, 2017.
- [129] Alexander Wilkie, Sehera Nawaz, Marc Droske, Andrea Weidlich, and Johannes Hanika. Hero wavelength spectral sampling. In *Computer Graphics Forum*, volume 33, pages 123–131. Wiley Online Library, 2014.
- [130] Bodo D Wilts, Kristel Michielsen, Hans De Raedt, and Doekele G Stavenga. Sparkling feather reflections of a bird-of-paradise explained by finite-difference time-domain modeling. *Proceedings of the National Academy of Sciences*, 111(12):4363–4368, 2014.

- [131] Joshua Wolper, Ming Gao, Martin P Lüthi, Valentin Heller, Andreas Vieli, Chenfanfu Jiang, and Johan Gaume. A glacier–ocean interaction model for tsunami genesis due to iceberg calving. *Communications Earth & Environment*, 2(1):1–10, 2021.
- [132] Joel Wretborn, Sean Flynn, and Alexey Stomakhin. Guided bubbles and wet foam for realistic whitewater simulation. *ACM Transactions on Graphics (TOG)*, 41(4):1–16, 2022.
- [133] X-Rite. Tac7 scanner, 2021.
- [134] Mengqi (Mandy) Xia, Bruce Walter, Eric Michielssen, David Bindel, and Steve Marschner. A wave optics based fiber scattering model. *ACM Trans. Graph.*, 39(6), 2020.
- [135] Ling-Qi Yan, Miloš Hašan, Wenzel Jakob, Jason Lawrence, Steve Marschner, and Ravi Ramamoorthi. Rendering glints on high-resolution normal-mapped specular surfaces. *ACM Transactions on Graphics (TOG)*, 33(4):1–9, 2014.
- [136] Ling-Qi Yan, Henrik Wann Jensen, and Ravi Ramamoorthi. An efficient and practical near and far field fur reflectance model. *ACM Transactions on Graphics (TOG)*, 36(4):1–13, 2017.
- [137] Ling-Qi Yan, Weilun Sun, Henrik Wann Jensen, and Ravi Ramamoorthi. A bssrdf model for efficient rendering of fur with global illumination. *ACM Transactions on Graphics (TOG)*, 36(6):1–13, 2017.
- [138] Ling-Qi Yan, Chi-Wei Tseng, Henrik Wann Jensen, and Ravi Ramamoorthi. Physically-accurate fur reflectance: Modeling, measurement and rendering. *ACM Transactions on Graphics (TOG)*, 34(6):1–13, 2015.
- [139] Bowen Yang, William Corse, Jiecong Lu, Joshua Wolper, and Chenfanfu Jiang. Real-time fluid simulation on the surface of a sphere. *Proc. ACM Comput. Graph. Interact. Tech.*, 2(1), June 2019.
- [140] Pochi Yeh. *Optical waves in layered media*. Wiley, 2005.
- [141] Haiwei Yin, Lei Shi, Jing Sha, Yizhou Li, Youhua Qin, Biqin Dong, Serge Meyer, Xiaohan Liu, Li Zhao, and Jian Zi. Iridescence in the neck feathers of domestic pigeons. *Physical Review E - Statistical, Nonlinear, and Soft Matter Physics*, 74(5), 2006.

- [142] Shinya Yoshioka, Eri Nakamura, and Shuichi Kinoshita. Origin of two-color iridescence in rock dove’s feather. *Journal of the Physical Society of Japan*, 76(1):013801, 2007.
- [143] Cem Yuksel. HAIR model files, 2020.
- [144] Cem Yuksel. High-performance polynomial root finding for graphics. *Proceedings of the ACM on Computer Graphics and Interactive Techniques*, 5(3):1–15, 2022.
- [145] Jonas Zehnder, Rahul Narain, and Bernhard Thomaszewski. An advection-reflection solver for detail-preserving fluid simulation. *ACM Transactions on Graphics (TOG)*, 37(4):1–8, 2018.
- [146] Tizian Zeltner, Iliyan Georgiev, and Wenzel Jakob. Specular manifold sampling for rendering high-frequency caustics and glints. *ACM Transactions on Graphics (TOG)*, 39(4):149–1, 2020.
- [147] Xianyao Zhang, Melvin Ott, Marco Manzi, Markus Gross, and Marios Papas. Automatic feature selection for denoising volumetric renderings. In *Computer Graphics Forum*, volume 41, pages 63–77. Wiley Online Library, 2022.
- [148] Bo Zhu, Ed Quigley, Matthew Cong, Justin Solomon, and Ronald Fedkiw. Codimensional surface tension flow on simplicial complexes. *ACM Transactions on Graphics (TOG)*, 33(4):111, 2014.
- [149] Arno Zinke and Andreas Weber. Light scattering from filaments. *IEEE Transactions on Visualization and Computer Graphics*, 13(2):342–356, 2007.

# Appendices

# A. Material Derivative in Spherical Coordinates

The material derivative describes the rate of change of a quantity moving with a time-dependent velocity field  $\vec{u}$ . We denote a dimensionless scalar quantity in spherical coordinates as  $\Phi(\theta, \phi, t)$ . Applying the chain rule yields

$$\frac{D\Phi}{Dt} = \frac{\partial\Phi}{\partial t} + \frac{\partial\Phi}{\partial\theta} \frac{d\theta}{dt} + \frac{\partial\Phi}{\partial\phi} \frac{d\phi}{dt}. \quad (\text{A.1})$$

The dimensionless velocities in spherical coordinates are defined as

$$u_\theta = \frac{d\theta}{dt}, \quad u_\phi = \sin\theta \frac{d\phi}{dt}. \quad (\text{A.2})$$

Note that we included the sphere radius  $R$  in our non-dimensionalization of  $t$  in Section 3.3.2, thus we do not need to take account of the sphere radius when taking the derivatives. Substituting Eq. (A.2) in Eq. (A.1) gives

$$\frac{D\Phi}{Dt} = \frac{\partial\Phi}{\partial t} + u_\theta \frac{\partial\Phi}{\partial\theta} + \frac{u_\phi}{\sin\theta} \frac{\partial\Phi}{\partial\phi}. \quad (\text{A.3})$$

The material derivative of a vector quantity, for example velocity, is similarly written as

$$\frac{D\vec{u}}{Dt} = \frac{\partial\vec{u}}{\partial t} + \frac{\partial\vec{u}}{\partial\theta} \frac{d\theta}{dt} + \frac{\partial\vec{u}}{\partial\phi} \frac{d\phi}{dt}, \quad (\text{A.4})$$

where

$$\frac{\partial\vec{u}}{\partial t} = \frac{\partial u_\theta}{\partial t} \vec{e}_\theta + \frac{\partial u_\phi}{\partial t} \vec{e}_\phi + u_\theta \frac{\partial \vec{e}_\theta}{\partial t} + u_\phi \frac{\partial \vec{e}_\phi}{\partial t}. \quad (\text{A.5})$$

To evaluate the remaining two partial derivatives, we take a step back to look at the derivatives of unit vectors in sphere coordinates. Neglecting the radial ( $r$ -dependent) component, they are

$$\frac{\partial \vec{e}_\theta}{\partial \theta} = 0, \quad \frac{\partial \vec{e}_\theta}{\partial \phi} = \cos\theta \vec{e}_\phi, \quad \frac{\partial \vec{e}_\phi}{\partial \theta} = 0, \quad \frac{\partial \vec{e}_\phi}{\partial \phi} = -\cos\theta \vec{e}_\theta. \quad (\text{A.6})$$

Thus,

$$\frac{\partial \vec{u}}{\partial \theta} = \frac{\partial u_\theta}{\partial \theta} \vec{e}_\theta + \frac{\partial u_\phi}{\partial \theta} \vec{e}_\phi + u_\theta \frac{\partial \vec{e}_\theta}{\partial \theta} + u_\phi \frac{\partial \vec{e}_\phi}{\partial \theta} = \frac{\partial u_\theta}{\partial \theta} \vec{e}_\theta + \frac{\partial u_\phi}{\partial \theta} \vec{e}_\phi, \quad (\text{A.7})$$

and

$$\begin{aligned} \frac{\partial \vec{u}}{\partial \phi} &= \frac{\partial u_\theta}{\partial \phi} \vec{e}_\theta + \frac{\partial u_\phi}{\partial \phi} \vec{e}_\phi + u_\theta \frac{\partial \vec{e}_\theta}{\partial \phi} + u_\phi \frac{\partial \vec{e}_\phi}{\partial \phi} \\ &= \frac{\partial u_\theta}{\partial \phi} \vec{e}_\theta + \frac{\partial u_\phi}{\partial \phi} \vec{e}_\phi + u_\theta \cos \theta \vec{e}_\phi - u_\phi \cos \theta \vec{e}_\theta. \end{aligned} \quad (\text{A.8})$$

Combining Eqs. (A.2), (A.5), (A.7) and (A.8) we obtain

$$\begin{aligned} \frac{D\vec{u}}{Dt} &= \left( \frac{\partial u_\theta}{\partial t} + u_\theta \frac{\partial u_\theta}{\partial \theta} + \frac{u_\phi}{\sin \theta} \frac{\partial u_\theta}{\partial \phi} - \frac{u_\phi^2}{\tan \theta} \right) \vec{e}_\theta \\ &\quad + \left( \frac{\partial u_\phi}{\partial t} + u_\theta \frac{\partial u_\phi}{\partial \theta} + \frac{u_\phi}{\sin \theta} \frac{\partial u_\phi}{\partial \phi} + \frac{u_\theta u_\phi}{\tan \theta} \right) \vec{e}_\phi. \end{aligned} \quad (\text{A.9})$$

## B. 2<sup>nd</sup>-Order Half-Step Update

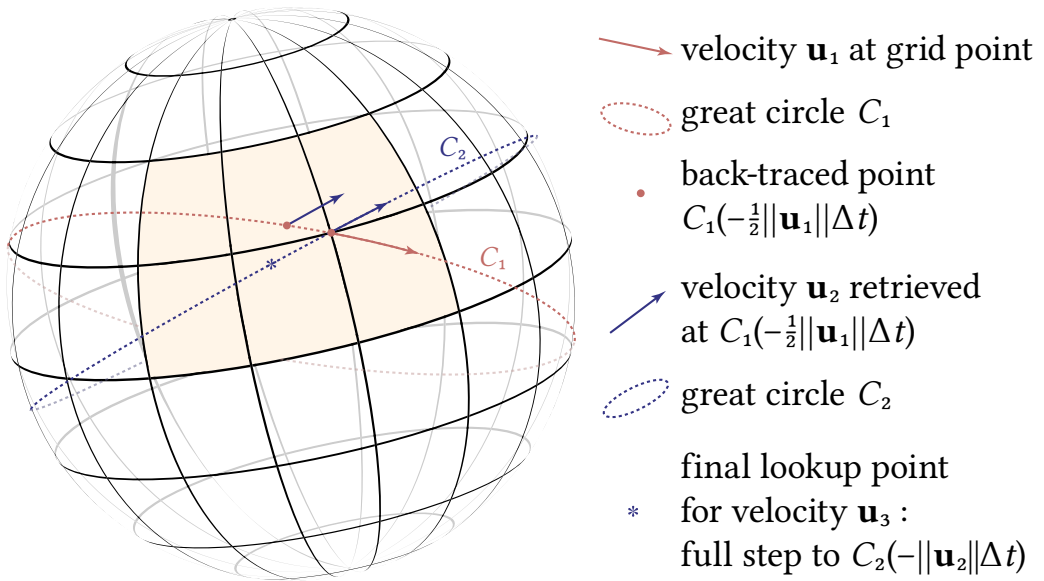


Figure B.1: Construction of a multi-step scheme similar to an order-2 Runge-Kutta update.

Based on the single-step scheme detailed in Section 3.4.2, we construct a multi-step scheme inspired by second-order Runge Kutta that can deliver higher accuracy (Fig. B.1). First, the velocity vector sampled at the grid point (red) defines a great circle (also red), which is used to construct a local coordinate frame. Following this direction backward by a *half* time step, a second velocity vector (blue) is sampled. After transforming this vector back to the original point, it generates a second great circle (also blue). A *full* backward step along this circle takes us to the look-up location (\*) for the value advected to the grid point.

## C. Linear System

We solve Eq. (3.26) on a grid of dimension  $m \times n$  and cell size  $\Delta s \times \Delta s$  in matrix form  $A\mathbf{\Gamma} = \vec{b}$ , where

$$\mathbf{\Gamma} = [\Gamma_{0,0}, \dots, \Gamma_{m-1,n-1}]^\top \in \mathbf{R}^{mn}, \quad \mathbf{b} = [b_{0,0}, \dots, b_{m-1,n-1}]^\top \in \mathbf{R}^{mn}$$

and  $A \in \mathbf{R}^{mn \times mn}$  is a sparse, block diagonal matrix with five elements in each row, corresponding to the cell itself and its four direct neighbors. In order to make  $A$  symmetric positive definite, we multiply both sides of Eq. (3.26) by  $\sin \theta$ . Then, in each row, the entries of  $A$  are given by

$$\begin{aligned} A_{i,\text{mid}} &= \sin \theta (\Delta t \Gamma_{\theta,\phi}^*)^{-1} + M \Delta t \Delta s^{-2} \\ &\quad \left[ \frac{\sin^{-1} \theta}{\eta_{\theta,\phi-\frac{\Delta s}{2}}^* + Cr \Delta t} + \frac{\sin^{-1} \theta}{\eta_{\theta,\phi+\frac{\Delta s}{2}}^* + Cr \Delta t} + \right. \\ &\quad \left. \frac{\sin(\theta + \frac{\Delta s}{2})}{\eta_{\theta+\frac{\Delta s}{2},\phi}^* + Cr \Delta t} + \frac{\sin(\theta - \frac{\Delta s}{2})}{\eta_{\theta-\frac{\Delta s}{2},\phi}^* + Cr \Delta t} \right], \\ A_{i,\text{left-right}} &= -\sin^{-1} \theta M \Delta t \Delta s^{-2} (\eta_{\theta,\phi \mp \frac{\Delta s}{2}}^* + Cr \Delta t)^{-1}, \\ A_{i,\text{up}} &= -\sin\left(\theta - \frac{\Delta s}{2}\right) M \Delta t \Delta s^{-2} (\eta_{\theta-\frac{\Delta s}{2},\phi}^* + Cr \Delta t)^{-1}, \\ A_{i,\text{down}} &= -\sin^{-1} \theta M \Delta t \Delta s^{-2} (\eta_{\theta,\phi+\frac{\Delta s}{2}}^* + Cr \Delta t)^{-1}, \end{aligned}$$

where  $\theta$  and  $\phi$  denote the cell center of the respective mid cell. The right hand side  $b$  is given by

$$b_{i,j} = \sin \theta \left( \frac{1}{\Delta t} - \nabla \cdot \frac{\eta_{i,j}^* \vec{u}_{i,j}^* + Cr \Delta t (\vec{u}_{\text{air}})_{i,j} + \Delta t \eta_{i,j}^* \vec{g}_{i,j}}{\eta_{i,j}^* + Cr \Delta t} \right).$$

# D. Derivation of the kinematic condition and the lubrication model in Eq. (3.10)

## D.1 The Kinematic Condition

In this section, we derive the kinematic condition in spherical coordinates (Eq. (3.7)). All the quantities preserve their physical dimensions.

Let  $F(\theta, \phi, r, t) = 0$  be an implicit definition of the outer bubble surface, where  $\eta$  is the half thickness of the film. Then, the height field at the outer side of the bubble can be written as  $r = R + \eta(\theta, \phi, t)$ , and the free surface is given by

$$F(\theta, \phi, r, t) = \eta(\theta, \phi, t) - r + R = 0. \quad (\text{D.1})$$

Taking the material derivative of  $F$  we have

$$\begin{aligned} 0 &= \frac{DF}{Dt} \\ &= \frac{\partial F}{\partial t} + \frac{\partial F}{\partial \theta} \frac{d\theta}{dt} + \frac{\partial F}{\partial \phi} \frac{d\phi}{dt} + \frac{\partial F}{\partial r} \frac{dr}{dt} \\ &= \frac{\partial F}{\partial t} + \frac{u_\theta}{R} \frac{\partial F}{\partial \theta} + \frac{u_\phi}{R \sin \theta} \frac{\partial F}{\partial \phi} + u_r \frac{\partial F}{\partial r} \\ &= \frac{\partial(\eta - r)}{\partial t} + \frac{u_\theta}{R} \frac{\partial(\eta - r)}{\partial \theta} + \frac{u_\phi}{R \sin \theta} \frac{\partial(\eta - r)}{\partial \phi} + u_r \frac{\partial(\eta - r)}{\partial r} \\ &= \left( \frac{\partial \eta}{\partial t} - 0 \right) + \frac{u_\theta}{R} \left( \frac{\partial \eta}{\partial \theta} - 0 \right) + \frac{u_\phi}{R \sin \theta} \left( \frac{\partial \eta}{\partial \phi} - 0 \right) + u_r (0 - 1) \\ &= \frac{\partial \eta}{\partial t} + \frac{u_\theta}{R} \frac{\partial \eta}{\partial \theta} + \frac{u_\phi}{R \sin \theta} \frac{\partial \eta}{\partial \phi} - u_r \end{aligned} \quad (\text{D.2})$$

and subsequently

$$u_r = \frac{\partial \eta}{\partial t} + \frac{u_\theta}{R} \frac{\partial \eta}{\partial \theta} + \frac{u_\phi}{R \sin \theta} \frac{\partial \eta}{\partial \phi}. \quad (\text{D.3})$$

The derivation for the inner side with  $r = R - \eta(\theta, \phi, t)$  is similar, yielding

$$-u_r = \frac{\partial \eta}{\partial t} + \frac{u_\theta}{R} \frac{\partial \eta}{\partial \theta} + \frac{u_\phi}{R \sin \theta} \frac{\partial \eta}{\partial \phi}. \quad (\text{D.4})$$

## D.2 Asymptotic Expansion

In this section, we derive Equation (10), with neglect of the force term  $\vec{f}$ . The Cauchy stress tensor  $\sigma$  in Equation (1) is defined in terms of local fluid pressure and viscosity as  $\sigma = -p\mathbf{I} + \mu[\nabla\vec{u} + (\nabla\vec{u})^\top]$ ; in spherical coordinates it has components

$$\sigma_{\theta\theta} = -p + \frac{2\mu}{r} \left( \frac{\partial u_\theta}{\partial \theta} + u_r \right), \quad (\text{D.5a})$$

$$\sigma_{\phi\phi} = -p + \frac{2\mu}{r \sin \theta} \left( \frac{\partial u_\phi}{\partial \phi} + u_\theta \cos \theta + u_r \sin \theta \right), \quad (\text{D.5b})$$

$$\sigma_{rr} = -p + 2\mu \frac{\partial u_r}{\partial r}, \quad (\text{D.5c})$$

$$\sigma_{\theta\phi} = \frac{\mu}{r \sin \theta} \left( \frac{\partial u_\theta}{\partial \phi} + \frac{\partial u_\phi}{\partial \theta} \sin \theta - u_\phi \cos \theta \right), \quad (\text{D.5d})$$

$$\sigma_{\theta r} = \frac{\mu}{r} \left[ r \frac{\partial u_\theta}{\partial r} - u_\theta + \frac{\partial u_r}{\partial \theta} \right], \quad (\text{D.5e})$$

$$\sigma_{\phi r} = \frac{\mu}{r \sin \theta} \left[ r \frac{\partial u_\phi}{\partial r} \sin \theta - u_\phi \sin \theta + \frac{\partial u_r}{\partial \phi} \right]. \quad (\text{D.5f})$$

The stress boundary conditions at both surfaces are

$$\sigma \cdot \vec{n}_{i,o} = (2\mathcal{C}_{i,o}\gamma - p_{i,o})\vec{n}_{i,o} + \nabla_s \gamma, \quad (\text{D.6})$$

where  $p_{i,o}$  represent air pressure at the inner and the outer surface, and  $2\mathcal{C}_{i,o} = -\nabla \cdot \vec{n}_{i,o}$  is twice the mean surface curvature, and the outward unit normal vectors to both film surfaces are

$$\vec{n}_o = \frac{-\frac{1}{r} \frac{\partial \eta}{\partial \theta} \vec{e}_\theta - \frac{1}{r \sin \theta} \frac{\partial \eta}{\partial \phi} \vec{e}_\phi + \vec{e}_r}{\sqrt{1 + \frac{1}{r^2} \left( \frac{\partial \eta}{\partial \theta} \right)^2 + \frac{1}{r^2 \sin^2 \theta} \left( \frac{\partial \eta}{\partial \phi} \right)^2}}, \quad (\text{D.7})$$

$$\vec{n}_i = \frac{-\frac{1}{r} \frac{\partial \eta}{\partial \theta} \vec{e}_\theta - \frac{1}{r \sin \theta} \frac{\partial \eta}{\partial \phi} \vec{e}_\phi - \vec{e}_r}{\sqrt{1 + \frac{1}{r^2} \left( \frac{\partial \eta}{\partial \theta} \right)^2 + \frac{1}{r^2 \sin^2 \theta} \left( \frac{\partial \eta}{\partial \phi} \right)^2}}, \quad (\text{D.8})$$

where as the (not normalized) tangent vectors are

$$\vec{t}_{o1} = \vec{e}_\theta + \frac{1}{r} \frac{\partial \eta}{\partial \theta} \vec{e}_r, \quad \vec{t}_{o2} = \vec{e}_\phi + \frac{1}{r \sin \theta} \frac{\partial \eta}{\partial \phi} \vec{e}_r, \quad (\text{D.9})$$

$$\vec{t}_{i1} = \vec{e}_\theta - \frac{1}{r} \frac{\partial \eta}{\partial \theta} \vec{e}_r, \quad \vec{t}_{i2} = \vec{e}_\phi - \frac{1}{r \sin \theta} \frac{\partial \eta}{\partial \phi} \vec{e}_r. \quad (\text{D.10})$$

With the variables in Equations (1), (5) and (52) non-dimensionalized by

$$\begin{aligned} \epsilon &= \frac{\eta_0}{R}, \quad \eta = \eta_0 \eta', \quad u_\theta = U u'_\theta, \quad u_\phi = U u'_\phi, \\ \sigma &= \frac{\mu U}{R} \sigma', \quad u_r = \epsilon U u'_r, \quad r = R + \epsilon R r', \\ t &= \frac{R}{U} t', \quad \Gamma = \Gamma_0 \Gamma', \quad p = \frac{\mu U}{R \epsilon} p', \quad D_s = U R D'_s, \end{aligned} \quad (\text{D.11})$$

and dropping the primes of the non-dimensionalized quantities for readability, we arrive at

$$\begin{aligned} \frac{\partial u_\theta}{\partial t} + u_\theta \frac{\partial u_\theta}{\partial \theta} + \frac{u_\phi}{\sin \theta} \frac{\partial u_\theta}{\partial \phi} + u_r \frac{\partial u_\theta}{\partial r} + \epsilon u_\theta u_r - \frac{u_\phi^2}{\tan \theta} \\ = R e^{-1} \left( \epsilon^{-1} \frac{\partial \sigma_{\theta r}}{\partial r} + \frac{\partial \sigma_{\theta \theta} \sin \theta}{\partial \theta} + \frac{1}{\sin \theta} \frac{\partial \sigma_{\theta \phi}}{\partial \phi} \right. \\ \left. + 3 \sigma_{\theta r} - \frac{\sigma_{\phi \phi}}{\tan \theta} \right), \end{aligned} \quad (\text{D.12a})$$

$$\begin{aligned} \frac{\partial u_\phi}{\partial t} + u_\theta \frac{\partial u_\phi}{\partial \theta} + \frac{u_\phi}{\sin \theta} \frac{\partial u_\phi}{\partial \phi} + u_r \frac{\partial u_\phi}{\partial r} + \epsilon u_\phi u_r + \frac{u_\theta u_\phi}{\tan \theta} \\ = R e^{-1} \left( \epsilon^{-1} \frac{\partial \sigma_{\phi r}}{\partial r} + \frac{\partial \sigma_{\theta \phi} \sin \theta}{\partial \theta} + \frac{1}{\sin \theta} \frac{\partial \sigma_{\phi \phi}}{\partial \phi} \right. \\ \left. + 3 \sigma_{\phi r} + \frac{\sigma_{\theta \phi}}{\tan \theta} \right), \end{aligned} \quad (\text{D.12b})$$

$$\begin{aligned} \epsilon \left( \frac{\partial u_r}{\partial t} + u_\theta \frac{\partial u_r}{\partial \theta} + \frac{u_\phi}{\sin \theta} \frac{\partial u_r}{\partial \phi} + u_r \frac{\partial u_r}{\partial r} \right) + u_\theta^2 + u_\phi^2 \\ = R e^{-1} \left( \epsilon^{-1} \frac{\partial \sigma_{r r}}{\partial r} + \frac{\partial \sigma_{\theta r} \sin \theta}{\partial \theta} + \frac{1}{\sin \theta} \frac{\partial \sigma_{\phi r}}{\partial \phi} \right. \\ \left. + 2 \sigma_{r r} - \sigma_{\theta \theta} - \sigma_{\phi \phi} \right), \end{aligned} \quad (\text{D.12c})$$

$$\frac{\partial u_\theta \sin \theta}{\partial \theta} + \frac{\partial u_\phi}{\partial \phi} + \sin \theta \frac{\partial u_r}{\partial r} = 0, \quad (\text{D.12d})$$

$$\begin{aligned} \frac{\partial \Gamma}{\partial t} + \frac{1}{\sin \theta} \left[ \frac{\partial}{\partial \theta} (\Gamma u_\theta \sin \theta) + \frac{\partial}{\partial \phi} (\Gamma u_\phi) \right] \\ = \frac{D_s}{\sin \theta} \left[ \frac{\partial}{\partial \theta} \left( \sin \theta \frac{\partial \Gamma}{\partial \theta} \right) + \frac{\partial}{\partial \phi} \left( \frac{1}{\sin \theta} \frac{\partial \Gamma}{\partial \phi} \right) \right]. \end{aligned} \quad (\text{D.12e})$$

Additionally, we introduce the following dimensionless numbers

$$S = \frac{\gamma_a \epsilon}{\mu U}, \quad Re = \frac{UR\rho}{\mu}, \quad M = \frac{\Gamma_0 \gamma_r}{\rho \eta_0 U^2}, \quad (\text{D.13})$$

where  $S$  is a measure of the equilibrium surface tension,  $Re$  is the Reynolds number and  $M$  is the Marangoni number. The surface tension is now given by

$$\gamma = \mu U (\epsilon^{-1} S - M Re \Gamma), \quad (\text{D.14})$$

and the expression for  $2\mathcal{C}_o$  is

$$2\mathcal{C}_o = \frac{\epsilon}{R} \left( \frac{\partial^2}{\partial \theta^2} + \frac{1}{\tan \theta} \frac{\partial}{\partial \theta} + \frac{1}{\sin^2 \theta} \frac{\partial^2}{\partial \phi^2} \right) \eta - \frac{2}{R} + \frac{2\epsilon \eta}{R} + O(\epsilon^2), \quad (\text{D.15})$$

whereas that for  $2\mathcal{C}_i$  is similar and not to be explicitly listed.

We perform an asymptotic analysis by expanding the variables in  $\epsilon$  series; that is, we expand  $\sigma_{\theta r}, \sigma_{\phi r}, \sigma_{rr}$  as

$$f = \epsilon^{-1} f^{(-1)} + f^{(0)} + \epsilon f^{(1)} + O(\epsilon^2), \quad (\text{D.16})$$

and  $\vec{u}, \Gamma, p, \eta$  as well as the other components of the stress tensor as

$$g = g^{(0)} + \epsilon g^{(1)} + O(\epsilon^2), \quad (\text{D.17})$$

Substituting the above expansions into Eq. (D.12), grouping terms with equal powers of  $\epsilon$  and setting the coefficients to zero, we obtain a series of solvable linear equations.

## D.2.1 Leading-order Equations

The leading-order problem consists of the continuity equation

$$\frac{\partial u_\theta^{(0)} \sin \theta}{\partial \theta} + \frac{\partial u_\phi^{(0)}}{\partial \phi} + \sin \theta \frac{\partial u_r^{(0)}}{\partial r} = 0, \quad (\text{D.18})$$

and the momentum equations

$$Re^{-1} \frac{\partial \sigma_{\theta r}^{(-1)}}{\partial r} = 0, \quad Re^{-1} \frac{\partial \sigma_{\phi r}^{(-1)}}{\partial r} = 0, \quad Re^{-1} \frac{\partial \sigma_{rr}^{(-1)}}{\partial r} = 0. \quad (\text{D.19})$$

For the boundary conditions, we have the kinematic condition (see Section D.1) at the outer boundary

$$u_r^{(0)} = \frac{\partial \eta^{(0)}}{\partial t} + u_\theta^{(0)} \frac{\partial \eta^{(0)}}{\partial \theta} + \frac{u_\phi^{(0)}}{\sin \theta} \frac{\partial \eta^{(0)}}{\partial \phi} \quad (\text{D.20})$$

and at the inner boundary

$$-u_r^{(0)} = \frac{\partial \eta^{(0)}}{\partial t} + u_\theta^{(0)} \frac{\partial \eta^{(0)}}{\partial \theta} + \frac{u_\phi^{(0)}}{\sin \theta} \frac{\partial \eta^{(0)}}{\partial \phi}, \quad (\text{D.21})$$

as well as the stress condition at the outer boundary

$$\sigma_{\theta r}^{(-1)} = 0, \quad \sigma_{\phi r}^{(-1)} = 0, \quad \sigma_{rr}^{(-1)} = -p_o - 2S, \quad (\text{D.22})$$

and at the inner boundary

$$\sigma_{\theta r}^{(-1)} = 0, \quad \sigma_{\phi r}^{(-1)} = 0, \quad \sigma_{rr}^{(-1)} = -p_i + 2S. \quad (\text{D.23})$$

Combining Eqs. (D.5), (D.19), (D.22) and (D.23), we discover that

$$\sigma_{\theta r}^{(-1)} = \frac{\partial u_\theta^{(0)}}{\partial r} = 0, \quad (\text{D.24})$$

$$\sigma_{\phi r}^{(-1)} = \frac{\partial u_\phi^{(0)}}{\partial r} = 0, \quad (\text{D.25})$$

$$\sigma_{rr}^{(-1)} = -p^{(0)} = -\frac{p_i + p_o}{2}. \quad (\text{D.26})$$

Thus,  $u_\theta^{(0)}$  and  $u_\phi^{(0)}$  are independent of  $r$  and are only functions of  $\theta, \phi$  and  $t$ . As a result, we may integrate the continuity equation (D.18) in  $r$  and obtain

$$u_r^{(0)} = -\frac{r}{\sin \theta} \left( \frac{\partial u_\theta^{(0)}}{\partial \theta} \sin \theta + \frac{\partial u_\phi^{(0)}}{\partial \phi} \right) + C(\theta, \phi, t), \quad (\text{D.27})$$

combining with the kinematic conditions (D.20) and (D.21) yields

$$\frac{\partial \eta^{(0)}}{\partial t} + u_\theta^{(0)} \frac{\partial \eta^{(0)}}{\partial \theta} + \frac{u_\phi^{(0)}}{\sin \theta} \frac{\partial \eta^{(0)}}{\partial \phi} + \frac{\eta^{(0)}}{\sin \theta} \left( \frac{\partial u_\theta^{(0)}}{\partial \theta} \sin \theta + \frac{\partial u_\phi^{(0)}}{\partial \phi} \right) = 0. \quad (\text{D.28})$$

The leading-order equation for the surfactant concentration is

$$\begin{aligned} \frac{\partial \Gamma^{(0)}}{\partial t} + \frac{1}{\sin \theta} \left[ \frac{\partial}{\partial \theta} (\Gamma^{(0)} u_\theta^{(0)} \sin \theta) + \frac{\partial}{\partial \phi} (\Gamma^{(0)} u_\phi^{(0)}) \right] \\ = \frac{D_s}{\sin \theta} \left[ \frac{\partial}{\partial \theta} \left( \sin \theta \frac{\partial \Gamma^{(0)}}{\partial \theta} \right) + \frac{\partial}{\partial \phi} \left( \frac{1}{\sin \theta} \frac{\partial \Gamma^{(0)}}{\partial \phi} \right) \right]. \end{aligned} \quad (\text{D.29})$$

From the leading-order problem, we obtain two evolution equations (D.28) and (D.29) for the film thickness  $\eta^{(0)}$  and the surfactant concentration  $\Gamma^{(0)}$ .

## D.2.2 Remaining Orders

From the momentum equations and the stress boundary conditions we similarly obtain

$$\sigma_{\theta r}^{(0)} = \sigma_{\phi r}^{(0)} = 0, \quad (\text{D.30})$$

$$\begin{aligned} \sigma_{rr}^{(0)} &= S \left( \frac{\partial^2}{\partial \theta^2} + \frac{1}{\tan \theta} \frac{\partial}{\partial \theta} + \frac{1}{\sin^2 \theta} \frac{\partial^2}{\partial \phi^2} + 2 \right) \eta^{(0)} \\ &= -p^{(1)} + 2 \frac{\partial u_r^{(0)}}{\partial r}. \end{aligned} \quad (\text{D.31})$$

Making use of Eqs. (D.5) and (D.31), we further obtain

$$\begin{aligned} \sigma_{\theta\theta}^{(0)} &= -p^{(1)} + 2 \frac{\partial u_\theta^{(0)}}{\partial \theta} \\ &= S \left( \frac{\partial^2}{\partial \theta^2} + \frac{1}{\tan \theta} \frac{\partial}{\partial \theta} + \frac{1}{\sin^2 \theta} \frac{\partial^2}{\partial \phi^2} + 2 \right) \eta^{(0)} \\ &\quad + \frac{2}{\sin \theta} \left( \frac{\partial u_\theta^{(0)} \sin \theta}{\partial \theta} + \frac{\partial u_\phi^{(0)}}{\partial \phi} \right) + 2 \frac{\partial u_\theta^{(0)}}{\partial \theta}, \end{aligned} \quad (\text{D.32})$$

$$\begin{aligned} \sigma_{\phi\phi}^{(0)} &= -p^{(1)} + 2 \left( \frac{1}{\sin \theta} \frac{\partial u_\phi^{(0)}}{\partial \phi} + \frac{u_\theta^{(0)}}{\tan \theta} \right) \\ &= S \left( \frac{\partial^2}{\partial \theta^2} + \frac{1}{\tan \theta} \frac{\partial}{\partial \theta} + \frac{1}{\sin^2 \theta} \frac{\partial^2}{\partial \phi^2} + 2 \right) \eta^{(0)} \\ &\quad + \frac{2}{\sin \theta} \left( \frac{\partial u_\theta^{(0)} \sin \theta}{\partial \theta} + 2 \frac{\partial u_\phi^{(0)}}{\partial \phi} + u_\theta^{(0)} \cos \theta \right). \end{aligned} \quad (\text{D.33})$$

Now the leading-order momentum equations in Eq. (D.12) can be rewritten as

$$\begin{aligned} &\frac{\partial u_\theta^{(0)}}{\partial t} + u_\theta^{(0)} \frac{\partial u_\theta^{(0)}}{\partial \theta} + \frac{u_\phi^{(0)}}{\sin \theta} \frac{\partial u_\theta^{(0)}}{\partial \phi} - \frac{(u_\phi^{(0)})^2}{\tan \theta} \\ &= Re^{-1} \left( \frac{\partial \sigma_{\theta r}^{(1)}}{\partial r} + \frac{\partial \sigma_{\theta\theta}^{(0)} \sin \theta}{\partial \theta} + \frac{1}{\sin \theta} \frac{\partial \sigma_{\theta\phi}^{(0)}}{\partial \phi} - \frac{\sigma_{\phi\phi}^{(0)}}{\tan \theta} \right), \end{aligned} \quad (\text{D.34a})$$

$$\begin{aligned} &\frac{\partial u_\phi^{(0)}}{\partial t} + u_\theta^{(0)} \frac{\partial u_\phi^{(0)}}{\partial \theta} + \frac{u_\phi^{(0)}}{\sin \theta} \frac{\partial u_\phi^{(0)}}{\partial \phi} + \frac{u_\theta^{(0)} u_\phi^{(0)}}{\tan \theta} \\ &= Re^{-1} \left( \frac{\partial \sigma_{\phi r}^{(1)}}{\partial r} + \frac{\partial \sigma_{\theta\phi}^{(0)} \sin \theta}{\partial \theta} + \frac{1}{\sin \theta} \frac{\partial \sigma_{\phi\phi}^{(0)}}{\partial \phi} + \frac{\sigma_{\theta\phi}^{(0)}}{\tan \theta} \right). \end{aligned} \quad (\text{D.34b})$$

The only unknowns remaining are  $\sigma_{\theta r}^{(1)}$  and  $\sigma_{\phi r}^{(1)}$ . To obtain them, we write the two tangential stress conditions in  $O(\epsilon)$  at the outer boundary as

$$\frac{\partial \eta}{\partial \theta} \left( \sigma_{rr}^{(0)} - \sigma_{\theta\theta}^{(0)} \right) - \frac{1}{\sin \theta} \frac{\partial \eta}{\partial \phi} \sigma_{\theta\phi}^{(0)} + \sigma_{\theta r}^{(1)} = -MRe \frac{\partial \Gamma^{(0)}}{\partial \theta}, \quad (\text{D.35})$$

$$\frac{1}{\sin \theta} \frac{\partial \eta}{\partial \phi} \left( \sigma_{rr}^{(0)} - \sigma_{\phi\phi}^{(0)} \right) - \frac{\partial \eta}{\partial \theta} \sigma_{\theta\phi}^{(0)} + \sigma_{\phi r}^{(1)} = -\frac{MRe}{\sin \theta} \frac{\partial \Gamma^{(0)}}{\partial \phi}. \quad (\text{D.36})$$

All the zero-order terms in Eq. (D.34) do not vary with  $r$ . Integrating Eq. (D.34) in  $r$  and applying Eqs. (D.35) and (D.36), then combining with Eqs. (D.5) and (D.18), we obtain the evolution equations for  $u_\theta^{(0)}$  and  $u_\phi^{(0)}$  to close our system

$$\begin{aligned} & \frac{\partial u_\theta^{(0)}}{\partial t} + u_\theta^{(0)} \frac{\partial u_\theta^{(0)}}{\partial \theta} + \frac{u_\phi^{(0)}}{\sin \theta} \frac{\partial u_\theta^{(0)}}{\partial \phi} - \frac{(u_\phi^{(0)})^2}{\tan \theta} \\ &= -\frac{M}{\eta^{(0)}} \frac{\partial \Gamma^{(0)}}{\partial \theta} \\ &+ Re^{-1} \left\{ \frac{1}{\eta^{(0)} \sin \theta} \frac{\partial \eta^{(0)}}{\partial \phi} \sigma_{\theta\phi}^{(0)} \right. \\ &\quad \left. + \frac{2}{\eta^{(0)}} \frac{\partial \eta^{(0)}}{\partial \theta} \left[ \frac{\partial u_\theta^{(0)}}{\partial \theta} + \frac{1}{\sin \theta} \left( \frac{\partial u_\theta^{(0)} \sin \theta}{\partial \theta} + \frac{\partial u_\phi^{(0)}}{\partial \phi} \right) \right] \right. \\ &\quad \left. + \frac{\partial \sigma_{\theta\theta}^{(0)} \sin \theta}{\partial \theta} + \frac{1}{\sin \theta} \frac{\partial \sigma_{\theta\phi}^{(0)}}{\partial \phi} - \frac{\sigma_{\phi\phi}^{(0)}}{\tan \theta} \right\}, \end{aligned} \quad (\text{D.37a})$$

$$\begin{aligned} & \frac{\partial u_\phi^{(0)}}{\partial t} + u_\theta^{(0)} \frac{\partial u_\phi^{(0)}}{\partial \theta} + \frac{u_\phi^{(0)}}{\sin \theta} \frac{\partial u_\phi^{(0)}}{\partial \phi} + \frac{u_\theta^{(0)} u_\phi^{(0)}}{\tan \theta} \\ &= -\frac{M}{\eta^{(0)} \sin \theta} \frac{\partial \Gamma^{(0)}}{\partial \phi} \\ &+ Re^{-1} \left\{ \frac{1}{\eta^{(0)}} \frac{\partial \eta^{(0)}}{\partial \theta} \sigma_{\theta\phi}^{(0)} \right. \\ &\quad \left. + \frac{2}{\eta^{(0)} \sin^2 \theta} \frac{\partial \eta^{(0)}}{\partial \phi} \left[ \frac{\partial u_\phi^{(0)}}{\partial \phi} + u_\theta^{(0)} \cos \theta + \frac{\partial u_\theta^{(0)} \sin \theta}{\partial \theta} + \frac{\partial u_\phi^{(0)}}{\partial \phi} \right] \right. \\ &\quad \left. + \frac{\partial \sigma_{\theta\phi}^{(0)} \sin \theta}{\partial \theta} + \frac{1}{\sin \theta} \frac{\partial \sigma_{\phi\phi}^{(0)}}{\partial \phi} + \frac{\sigma_{\theta\phi}^{(0)}}{\tan \theta} \right\}, \end{aligned} \quad (\text{D.37b})$$

where  $\sigma_{\theta\theta}^{(0)}$  and  $\sigma_{\phi\phi}^{(0)}$  are given by Eq. (D.32), and

$$\sigma_{\theta\phi}^{(0)} = \frac{1}{\sin\theta} \left( \frac{\partial u_\theta^{(0)}}{\partial\phi} + \frac{\partial u_\phi^{(0)}}{\partial\theta} \sin\theta - u_\phi^{(0)} \cos\theta \right). \quad (\text{D.38})$$

The full evolution equations are thus Eqs. (D.28), (D.29) and (D.37). If we denote terms in Eq. (D.37) associated with  $Re^{-1}$  as  $\vec{V}$ , and drop the superscript  $^{(0)}$ , the governing equations can be simplified to

$$\left[ \begin{array}{l} \frac{D\vec{u}}{Dt} = -\frac{M}{\eta} \nabla\Gamma + Re^{-1}\vec{V}, \end{array} \right. \quad (\text{D.39a})$$

$$\left[ \begin{array}{l} \frac{D\Gamma}{Dt} = -\Gamma\nabla \cdot \vec{u} + D_s \nabla^2\Gamma, \end{array} \right. \quad (\text{D.39b})$$

$$\left[ \begin{array}{l} \frac{D\eta}{Dt} = -\eta\nabla \cdot \vec{u}, \end{array} \right. \quad (\text{D.39c})$$

with  $\vec{u} = (u_\theta, u_\phi)^\top$ . This corresponds to Eq. (3.10).

## E. Analytical Integration of the lobe for GGX

The GGX distribution with roughness parameter  $\beta$  is

$$D(\omega_h, \omega_{m\alpha}) = \frac{\beta^2}{\pi(1 + (\beta^2 - 1)(\omega_h \cdot \omega_{m\alpha})^2)^2}, \quad (\text{E.1})$$

where

$$\begin{aligned} \omega_h \cdot \omega_{m\alpha} &= \sin \varphi_h \cos \theta_h \sin \varphi_m \cos \alpha + \sin \theta_h \sin \alpha + \cos \varphi_h \cos \theta_h \cos \varphi_m \cos \alpha \\ &= \cos \theta_h \cos \alpha \cos(\varphi_h - \varphi_m) + \sin \theta_h \sin \alpha. \end{aligned} \quad (\text{E.2})$$

Substituting  $\cos \theta_h \cos \alpha \sqrt{1 - \beta^2}$  with  $A$ ,  $\sin \theta_h \sin \alpha \sqrt{1 - \beta^2}$  with  $B$ , the indefinite integral of Eq. (E.1) in  $\varphi_m$  is then

$$\begin{aligned} & \int D(\omega_h, \omega_{m\alpha}) d\varphi_m \\ &= \frac{\beta^2}{\pi} \int \frac{1}{(1 - (A \cos(\varphi_h - \varphi_m) + B)^2)^2} d\varphi_m \\ &= \frac{\beta^2}{4\pi} \left( \frac{2(A^2 - B^2 + 3B - 2)}{((B - 1)^2 - A^2)^{3/2}} \tan^{-1} \left( \frac{(A - B + 1) \tan \frac{\varphi_h - \varphi_m}{2}}{\sqrt{(B - 1)^2 - A^2}} \right) + \right. \\ & \quad \frac{2(A^2 - B^2 - 3B - 2)}{((B + 1)^2 - A^2)^{3/2}} \tan^{-1} \left( \frac{(B - A + 1) \tan \frac{\varphi_h - \varphi_m}{2}}{\sqrt{(B + 1)^2 - A^2}} \right) + \\ & \quad \left. \frac{A \sin(\varphi_h - \varphi_m)}{((B - 1)^2 - A^2) (A \cos(\varphi_h - \varphi_m) + B - 1)} + \right. \\ & \quad \left. \frac{A \sin(\varphi_h - \varphi_m)}{((B + 1)^2 - A^2) (A \cos(\varphi_h - \varphi_m) + B + 1)} \right) + C, \end{aligned} \quad (\text{E.3})$$

with  $C$  being some constant. If the scale tilt  $\alpha = 0$ , the above equation can be simplified as

$$\begin{aligned}
\int D(\omega_h, \omega_m) d\varphi_m &= \frac{\beta^2}{\pi} \int \frac{1}{(1 - A^2 \cos^2(\varphi_h - \varphi_m))^2} d\varphi_m \\
&= \frac{\beta^2}{2\pi} \left( \frac{(A^2 - 2)}{(1 - A^2)^{3/2}} \tan^{-1} \left( \frac{\tan(\varphi_h - \varphi_m)}{\sqrt{1 - A^2}} \right) + \right. \\
&\quad \left. \frac{A^2 \sin(2(\varphi_h - \varphi_m))}{(1 - A^2)(A^2 \cos(2(\varphi_h - \varphi_m)) + A^2 - 2)} \right) + C.
\end{aligned} \tag{E.4}$$

The lower bound of the integral is the minimal possible  $\varphi_m$  that satisfies  $\omega_m \cdot \omega_i > 0$  and  $\omega_m \cdot \omega_o > 0$ , the upper bound of the integral is likewise the maximal possible  $\varphi_m$  that satisfies the same inequations.

## F. Interference on Flat and Curved Thin Films

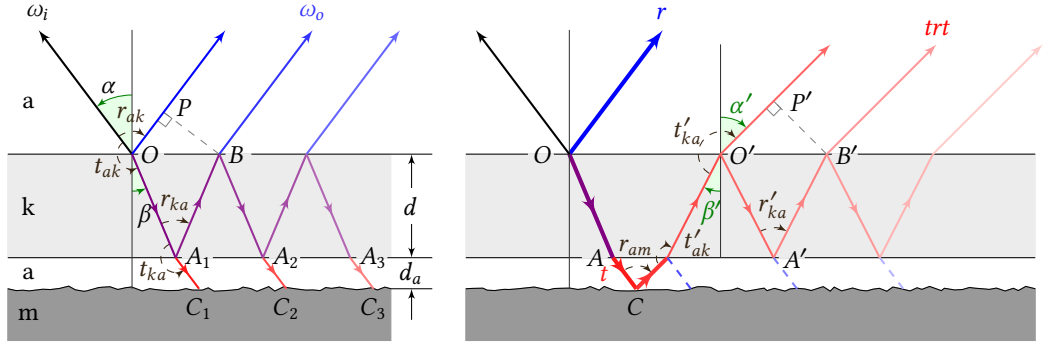


Figure F.1: Thin-film interference. **Left:** thin-film reflection (blue arrows). **Right:** thin-film reflection (blue) and the background component (red), which is transmitted through the keratin layer, reflected on the melanin layer, then transmitted back through the keratin layer.

**Airy Formula** [140] The optical path difference (OPD) for thin-film reflection and transmission is  $\mathcal{D} = \eta_k(\overline{OA_1} + \overline{A_1B}) - \eta_a\overline{OP} = 2d\eta_k \cos \beta$  (Fig. F.1). Thus, the complex thin-film reflection coefficient  $r$  is computed as

$$\begin{aligned}
 r &= r_{ak} + t_{ak}r_{ka}t_{ka}e^{i\Delta\psi_r} + t_{ak}r_{ka}r_{ka}^2t_{ka}e^{2i\Delta\psi_r} + \dots \\
 &= r_{ak} + \sum_{n=0}^{+\infty} t_{ak}r_{ka}t_{ka}e^{i\Delta\psi_r} [r_{ka}^2e^{i\Delta\psi_r}]^n \\
 &= r_{ak} + \frac{t_{ak}r_{ka}t_{ka}e^{i\Delta\psi}}{1 - r_{ka}^2e^{i\Delta\psi}}, \tag{F.1}
 \end{aligned}$$

and the complex thin-film transmission coefficient

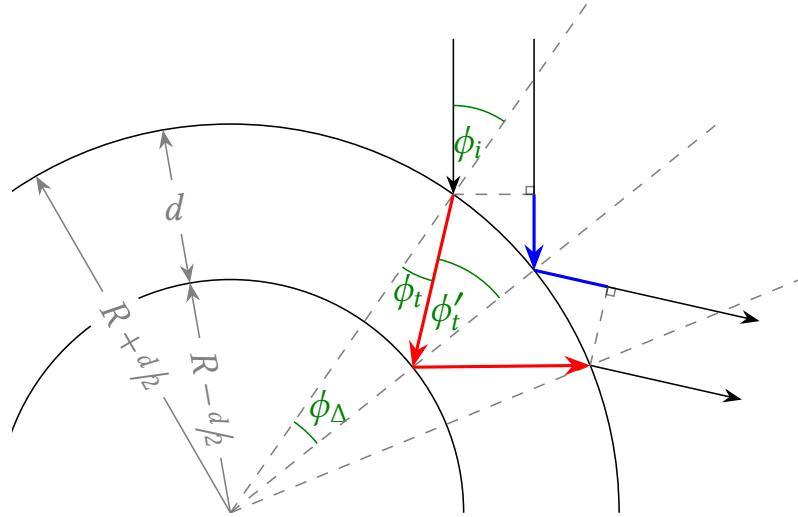
$$\begin{aligned}
t &= t_{ak}t_{ka} + t_{ak}r_{ka}^2t_{ka}e^{i\Delta\psi} + t_{ak}r_{ka}^4t_{ka}e^{2i\Delta\psi} + \dots \\
&= \sum_{n=0}^{+\infty} t_{ak}t_{ka} [r_{ka}^2e^{i\Delta\psi}]^n \\
&= \frac{t_{ak}t_{ka}}{1 - r_{ka}^2e^{i\Delta\psi}}.
\end{aligned} \tag{F.2}$$

The OPD for the TRT component is similarly computed as  $\mathcal{D}' = \eta_k(\overline{OA'} + \overline{A'B}) - \eta_a\overline{O'P'} = 2d\eta_k \cos \beta'$ . Thus,

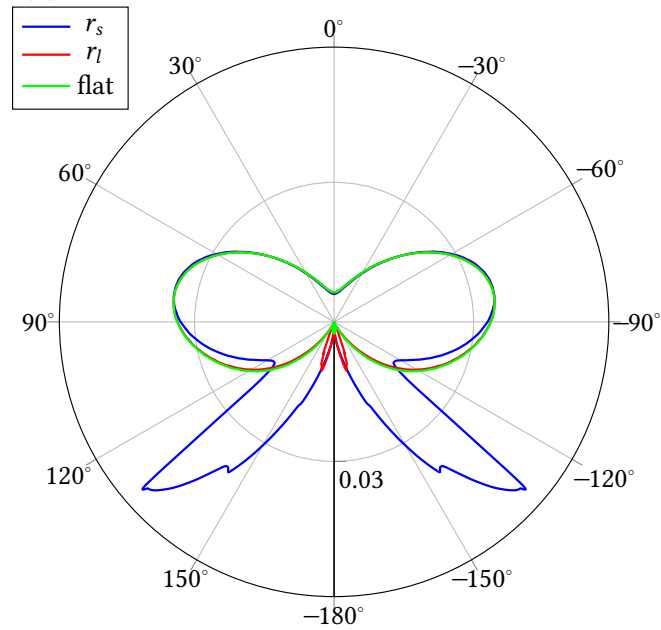
$$\begin{aligned}
I_{\text{TRT}} &= \left| tr_{am}t'_{ak}t'_{ka} + tr_{am}t'_{ak}(r'_{ka})^2t'_{ka}e^{i\Delta\psi'} + \dots \right|^2 \\
&= \left| \frac{tr_{am}t'_{ak}t'_{ka}}{1 - (r'_{ka})^2e^{i\Delta\psi'}} \right|^2.
\end{aligned} \tag{F.3}$$

**Thin-film interference with curvature** We perform a 2D analysis of curved thin film interference. Fig. F.2a shows parallel light hitting a hollow cylindrical tube. The two indicated incident rays with the same axis of symmetry interfere, as their outgoing directions are also parallel. The optical path difference is the difference between the optical path length of the blue and red paths. Further orders of interference are computed analogously.

We compare the reflectance off such a cylindrical tube as a function of the difference between the incoming and outgoing directions, with  $\lambda = 520$  nm,  $d = 650$  nm. We choose a large curvature radius  $r_l = 40$   $\mu\text{m}$  and a small curvature radius  $r_s = 4$   $\mu\text{m}$ , and compare the reflectance with a flat thin film. As shown in Fig. F.2b, there is almost no difference between the reflectance off a flat and a curved keratin thin film, except at near-grazing angles, where total internal reflection happens, as on a convex curved thin film  $\phi'_t > \phi_t$ . These angles can generally not be observed due to the overlapping geometry of the barbules, and the curvature radius is only small at the edge of the barbule. Thus, we assume the barbule to be piecewise flat for simplicity.



(a) Parallel rays hitting a cylindrical keratin tube



(b) Reflectance with piecewise flat assumption (green) plotted against analytically computed reflectance with curvature (blue and red). The red plot has a curvature radius of  $40\ \mu\text{m}$ , which is almost indistinguishable from the green plot. This is also the average curvature radius of a rock dove neck feather barbule. The blue plot has a curvature radius of  $4\ \mu\text{m}$ , showing a large difference at near-grazing angles. Such a small radius only occurs at the edge of the barbule.

Figure F.2: Illustration and reflectance plot of interference on a curved thin film.

## G. Melanin transmittance

In our model we consider thin-film interference of the keratin layer (R component), and the transmission through the keratin layer times the reflection off the melanin layer times the transmission through the keratin layer back into the eyes (TRT component), plus the transmission through the barbule gaps (T component). As we have seen, the intensity of the TRT component is already very low, and all subsequent components are ignored because of melanin's large absorptance. The refractive index of melanin is  $1.648 + 0.0632i$  at 589 nm [112], which means an absorption coefficient of  $\alpha = \frac{0.0632 \times 4\pi}{589 \text{ nm}} = 0.0013 \text{ nm}^{-1}$ . After traveling  $2 \mu\text{m}$  of melanin granules, the light intensity would be attenuated by  $\exp(-\alpha \times 2 \mu\text{m}) = 6.7\%$ , which is fairly low. Melanin-rich dark human hairs also have very low transmittance [93]. Unlike on human hairs, bird feathers overlap substantially so that backlit doesn't occur, thus, to be able to reach the eyes, further components must be reflected again on another feather underneath it, and possibly transmitted again through the feather, causing even more light to be absorbed. Such a contribution is very low.

## H. Ablation Study of Feather Rendering Model Parameters

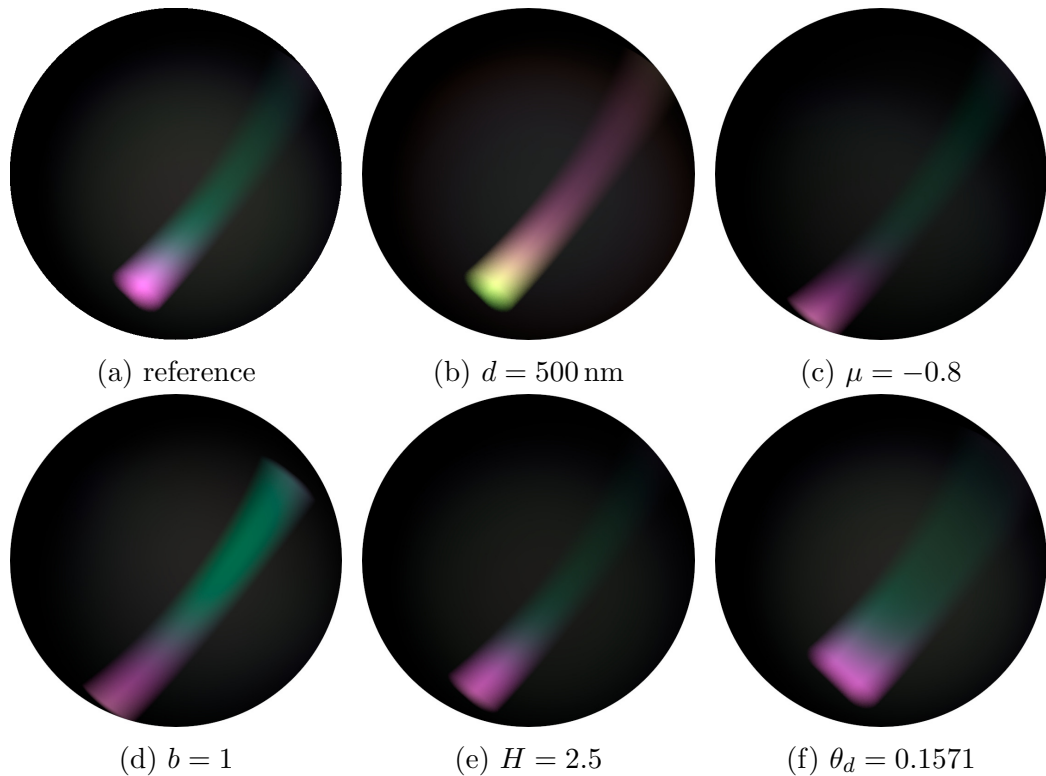


Figure H.1: Ablation study with parameters that differ from Chapter 5 (shown in (a)). One parameter is varied in each rendering: (b) keratin layer thickness changed from 590 nm to 500 nm, (c) barbule orientation changed from -0.35 to -0.8, (d) semi-minor axis changed from 0.25 to 1, (e) barbule spacing changed from 1.25 to 2.5, (f) circular arc opening angle changed from 0.0785 to 0.1571.

Models for rendering hair or fur usually assume a circular cross-section of the fibers. The first column of Fig. H.1 shows a comparison of our model

(Fig. H.1a), which assumes an elliptical cross-section of the barbules, to the BSDF produced by a circular cross-section (Fig. H.1d). Compared to the scatterogram in Fig. 5.1d (top), our elliptical model is clearly much closer to the measurement than a circular model.

We also provide such an ablation study in Fig. H.1 for other parameters. As expected from Fig. 5.3, changing the thickness  $d$  of the keratin layer produces different scattered colors (Fig. H.1b). Changing the spacing  $H$  and orientation  $\mu$  of the barbules affects the visible normal distribution and the gap between the barbules, thus changing the intensity of the scattered light (Figs. H.1c and H.1e). With an increased spacing between the barbules and a larger inclination angle, the amount of transmitted light increases, so the intensity of the reflection is lowered. Increasing the opening angle  $\theta_d$  of the barbule's circular arc in the longitudinal direction increases the scattering angle in the corresponding direction (Fig. H.1f).